Calibration of a SuperDARN Radar Antenna by means of a Satellite Beacon

Prepared by:

Doreen Agaba

AGBDOR001

Supervised by:

Prof. M. Inggs

Department of Electrical Engineering, University of Cape Town

Dr. P. J. Cilliers

South African National Space Agency, Hermanus

June 2012

A dissertation submitted to the Department of Electrical Engineering,

University of Cape Town,

in partial fulfilment of the requirements

for the degree of

Master of Philosophy

Declaration

1. Each contribution to, and quotation in this project report from the work(s) of other people, has been acknowledged, cited and referenced.

2. This project is my own work and no other person's work was plagiarised.

3. No one may use this work or part thereof without due acknowledgement.

Signature of Author . . . .

Cape Town
June 2012

Abstract

This dissertation reports on the investigation to determine which orbits, ionospheric conditions and seasons of the year that will facilitate the reception of the high frequency (HF) beacon signal from the 1 U CubeSat ZACUBE 1 by the SuperDARN HF radar in Antarctica, and by the HF direction-finding (DF) systems in both Pretoria and Hermanus. The primary objective of the HF beacon on ZACUBE 1 is to provide a continuous radio signal to calibrate and verify the elevation-resolving algorithm of the SuperDARN HF Radar antenna at SANAE IV in Antarctica. The signal will also be used to characterise the beam pattern of this and other HF radar antennas in the SuperDARN network, and to characterise the ionosphere over the Earth's polar region. A secondary objective of the HF beacon on the satellite is to measure the ionospheric total electron content (TEC) by using either measurements of the carrier phase delays or of the Faraday rotation of the signal.

An orbit analysis was done for the CubeSat using parameters for an orbit at an altitude of 600 km and inclination angles of $97.8°$ and $65°$. To account for the propagation effects of the radio wave at 14.099 MHz, the IRI-2007 model and the Chapman layer model were used to define the ionosphere. A ray tracing algorithm written in MATLAB was used to simulate the ray paths. To evaluate the results, a documented ray tracing algorithm known as Haselgrove ray tracing was used. The results obtained show that for an orbit at an inclination above $70°$ and altitude of 600 km, a number of rays actually traverse the ionosphere and reach the receivers during most of the year for a sufficient period of time during every pass. The least refraction is experienced during winter, therefore it is the best time for the calibration of the radar antenna. The results indicate that the objectives of the CubeSat mission should be achieved.

This research is dedicated to my beloved husband **Philip Atuhaire** and to our baby who is yet to be born.

Acknowledgements

First of all, I would like to thank God for His grace, strength and love in my life. Then I would like to appreciate the endless help from my supervisors, Prof M. Inggs and Dr P. J. Cilliers. They gave me constant advice and encouragement during the course of this study.

I am grateful to the National Astrophysics and Space Science Programme (NASSP) for funding my study. Prof Peter Dunsby, the NASSP director and Mrs Nicky Walker, the administrator made it possible for me to live and study in this beautiful country and I am very grateful. I also appreciate the coorperation and support of the NASSP space science students, Mr T.J Phiri, Mr O. Samuel and Mr A. Michael, with whom I shared this journey of learning and growth.

To Dr Lee-Anne McKinnell and the rest of the administration and staff of the South African National Space Agency (SANSA), thank you for your support during my stay in Hermanus. In particular I wish to acknowledge Mrs Anita Engelbrecht, Dr B. Opperman, Dr Z. Katamzi, Dr S. Lotz, Dr J. B. Habarulema, Mrs J. Cilliers, Mrs E. Siziba, Mrs K. Matamba. You sacrificed your time and energy amidst the busy schedules to make my stay in Hermanus memorable.

Last, but not least, I would like to thank my family and relatives, particularly my dear husband, for the continued support, emotional and financial, and for giving me the permission to be away from home so that I could study. And to my mother Ms J. Kamusiime, father Mr A. Mpora, brother Mr D. Ahumuza and sister Miss H. Akisiimire, may the almighty God bless you in ways greater than your imagination.

Doreen Agaba

Cape Town, South Africa

June 2012

Contents

List of Tables

List of Figures

Nomenclature

Azimuth—Angle in a horizontal plane, relative to a fixed reference, usually north or the longitudinal reference axis of the aircraft or satellite.

Beacon—A fixed-frequency unmodulated carrier transmitted by the satellite for reception on the ground.

CubeSat—A type of miniaturised satellite for space research. The 1 U CubeSat of $10 \times 10 \times 10$ cm, maximum weight of 1.33 kg, provides total power of about 3 W and typically uses commercial off-the-shelf electronic components.

Doppler effect—A shift in the radio frequency of the return signal from a target or other object as a result of the object's radial motion relative to the radar.

Elevation angle—The angle between the horizontal plane and the line of sight along the ray path, measured in the vertical plane and it is positive above the horizon (0 elevation angle), but negative below the horizon.

Range—The radial distance from a radar to a target.

Ray tracing—A method of determining the path of waves through a system with regions of varying propagation properties.

SuperDARN—An international network of radars which are being used for monitoring the plasma convection in the Antarctic and Arctic regions.

Zenith angle—The angle relative to the vertical line or zenith at the receiver.

Chapter 1

Introduction

1.1 Problem description

In 1997 the 4th South African National Antarctic Expedition (SANAE IV) completed the
construction of one of the first Super Dual Auroral Network (SuperDARN) radars to be
deployed in Antarctica (Chisham *et al.*, 2007). This research addresses the calibration of
the elevation algorithm and beam pattern of the SANAE IV HF radar antenna using data
from an HF satellite beacon. Previous attempts to calibrate the antenna in 2007 by means
of an HF transmitter on a helicopter failed due to logistical problems, which prohibited the
continuous transmission of the HF signal (Cilliers, 2007). A similar attempt to characterise
the SuperDARN radar at Saskatoon in Canada (52.16°N, 106.53°W) using a transmitter on
board an airplane was not successful (Sterne, 2010).

The SuperDARN array at SANAE IV comprises two antenna arrays referred to as the main
array and the interferometer array, separated by 100 m. Both the arrays are made up of
sets of twin terminated folded dipoles. The purpose of the interferometer array is to detect
the elevation angle of HF radar reflections from the ionosphere by using the phase difference
between the signals received on the main and interferometer arrays. Although most of the
HF radars in the network have interferometer arrays, the elevation information on the radar
returns have not been successfully extracted from the available data due to problems with
the elevation-resolving algorithm for such radars. The elevation-resolving capability of the
radar has not been fully utilised because the antenna characteristics and the ground plane are
difficult to calibrate. Furthermore, the radiation pattern of the HF radar which is another
key element in the interpretation of the data obtained by means of the radar, has not been
fully defined. The beam pattern provides the direction of maximum power transmission,
which in turn is used for inferring the predominant altitude of the radar return signals.

Therefore, an elevation algorithm needs to be compiled from the combination of the main

1

array and the interferometer data once the beam pattern is clearly understood and the effects of the ground plane have been taken into account. The proposed method to characterise these antennas is by means of a beacon transmitter on a satellite, which is in an orbit that allows the signal transmitted to be received by the radar receiver on the ground. Although there have been satellites in the past which had HF beacons on board such as Sputnik, there are currently no operational satellites with suitable HF beacons for the calibration of the SuperDARN HF radar antennas.

In an effort to obtain such data, the South African National Space Agency (SANSA) proposed an HF beacon as the primary scientific payload for the 1 U CubeSat, ZACUBE 1. The CubeSat was developed by the Cape Peninsula University of Technology (CPUT) in collaboration with the French South African Institute of Technology (F'SATI). The HF beacon transmitter will transmit a 14.099 MHz signal expected to be received by the HF radar on the ground. During propagation through the ionosphere, the wave undergoes changes in phase and amplitude. These effects are associated with refraction and absorption of the waves which depend on the frequency of transmission, ionospheric conditions and the elevation angle. In order to determine if and when the signal will actually reach the receiver, the actual orbits and ionospheric conditions are simulated and the ray paths are determined by means of ray tracing.

1.2 ZACUBE 1 CubeSat specifications

ZACUBE 1v is a 1 U CubeSat with dimensions $10 \times 10 \times 10$ cm. It was developed as a forerunner of ZACUBE 2, a 3 U prototype with dimensions $30 \times 30 \times 30$ cm for the next mission. The 1 U CubeSat is expected to be used for short term research while the 3 U prototype is intended for longer term research. Both satellites are designed with a de-orbiting mechanism to predetermine their lifespan. The satellite constitutes a number of subsystems:

1. an on-board computer which executes the flight software that schedules tasks and carries out telemetry and telecommand,

2. a power system which consists of solar panels,

3. a battery and a power controller to provide electrical energy to all the subsystems,

4. a very high frequency (VHF) or ultra high frequency (UHF) radio receiver,

5. and an Attitude Determination Control System (ADCS) which orients the satellite to point its communication antennas towards Earth.

The satellite will transmit HF radio signals at 200 mW in an orbit and at an altitude in the range of 450 to 850 km with orbital inclination between 65° to 98°. Details can be found in the mission technical report by Visser (2009).

Table 1.1: Proposed ZACUBE 1 orbital parameters and satellite characteristics taken from Visser (2009).

Semi-major axis	7038.134 km
Eccentricity	0.008524983
Perigee altitude	600 km
Apogee altitude	720 km
Inclination	97.8°
Orbital period	98 minutes
Number of orbits per day	14
Satellite mass	1.15 kg
Satellite dimensions	10×10×10 cm
Mean cross-sectional surface area	0.016 m^2

The main payload of ZACUBE 1 is designed to emit an HF beacon signal that can be received and decoded by receivers on the ground. The beacon transmitter is a relatively simple payload that will provide potentially large returns for space science. In the satellite's payload module is the beacon transmitter, an HF antenna deployment mechanism and a simple experimental camera module for monitoring the deployment of the HF antenna, and possibly to take pictures of the Earth.

The HF satellite beacon transmitter or receiver can be used to measure propagation effects on radio signals traversing the ionosphere (Appleyard *et al.*, 1988). The beacon transmitter has been proposed because of its simplicity and a large number of applications. However, the signal will only be received on the ground if the signal to noise ratio (S/N) at the receiver is greater than approximately 10 dB (Visser, 2009). It is necessary to know the link budget of the HF beacon and ground receiver so as to determine whether the signal strength will be sufficient for it to be received on the ground.

A link budget is the accounting of all the gains and losses from the transmitter, through the medium to the receiver. The signal gains, such as antenna gain, and losses depend on its power at the point of transmission, the band width and distance to the receiver. Some of these losses include: pointing loss, propagation loss, loss in the cables, polarisation loss, feedline, absorption losses and other miscellaneous losses (Michael, 2002). Antenna diversity and frequency hopping are methods that can be used to mitigate these losses. Therefore, by neglecting the absorption of the signal in the ionospheric D-layer and assuming a fixed signal strength over all signal paths from the satellite, the link budget can be calculated by

using simplified equations. Details of the link budget equation can be found in Das (2010). The link budget equation is given by

$$P_r = P_t + G_r + G_t - P_{\text{loss}}, \tag{1.1}$$

where P_r is the received power in dBm (dB relative to 1 mW), P_t is the transmitter power in dBm , G_r is the receiver gain in dB given by Equation 1.2, G_t is the transmitter gain in dB given by Equation 1.3, and P_{loss} is the total power loss as a result of transmitter loss, receiver loss, free space loss and miscellaneous losses (fading margin and polarisation mismatch).

$$G_r = e_r D \tag{1.2}$$

$$G_t = e_t D, \tag{1.3}$$

where e_r is the receiver antenna efficiency, e_t is the transmitter antenna efficiency and D the antenna directivity in dB. The Friis' transmission equation (Equation 1.4) is used to calculate received signal power based on the frequency, range, antenna gains, transmitter power and additional losses (Michael, 2002).

$$\frac{P_r}{P_t} = G_r G_t (\frac{\lambda}{4\pi d})^2 \tag{1.4}$$

where λ is the is the wavelength, and d is the distance between the antennas. To summarise the link budget calculations, in terms of power gains and losses, the factors that determine whether or not a signal transmitted from a satellite will be received by a ground receiver depend on: transmitter power, transmitter gain and the distance between the transmitter and receiver (path loss). Path loss depends on orbital altitude, elevation, frequency of transmission, noise (galactic noise, atmospheric noise and edging of transmitter), receiver power and the strength of the received signal. Atmospheric noise and galactic noise are usually referred to as sky noise and sky noise temperature varies with frequency as shown in Figure 1.1.

As the satellite passes over a ground receiver, the changing distance between the satellite and the receiver may lead to increased absorption when the ray travels through a longer section of the ionosphere. Therefore, the link budget is used to determine whether, after adding all the gains and subtracting the losses, the satellite signal still has sufficient strength to be received.
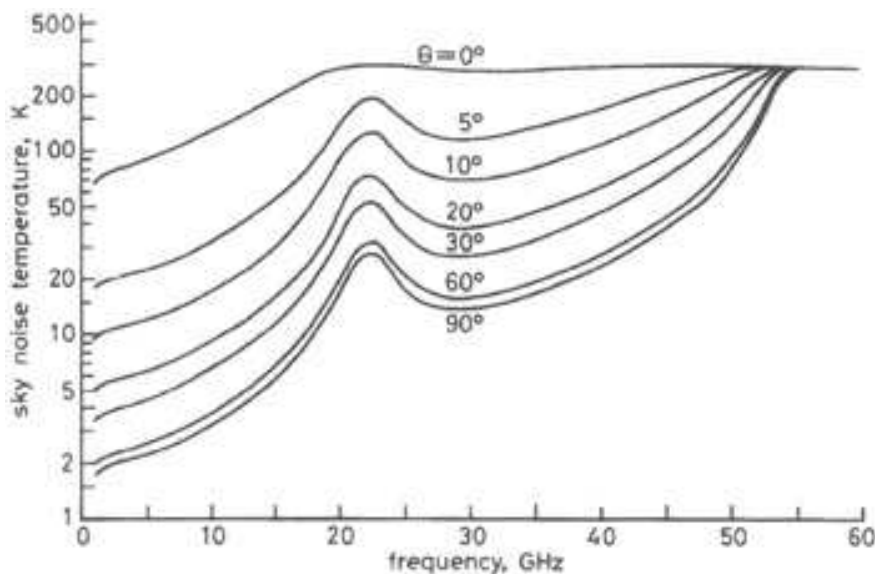
Figure 1.1: Figure illustrating the variation of sky noise with temperature at various elevation angles (Evans, 2008)

1.3 Proposed instruments for tracking and receiving the ZACUBE 1 signal

1.3.1 The SuperDARN radar at SANAE IV in Antarctica

The SuperDARN is an international network of radars which is being used for monitoring the plasma convection in Antarctica and the Arctic regions. Presently, there are 14 Super-DARN radars in the northern hemisphere and 8 in the southern hemisphere with operating frequencies in the range of 8 MHz to 20 MHz. Each radar has a total of 16 beams, typical azimuthal field of view of 54° and a scan period of 1 minute. These radars are almost identical in design and each of them transmits a short sequence of pulses in the HF band.

The SuperDARN radars are capable of measuring the velocity of charged particles in the Earth's ionosphere. For over ten years now, data from the SuperDARN radars has proven to be extremely useful in addressing a wide range of scientific questions concerning processes in the magnetosphere, ionosphere, thermosphere, mesosphere and general plasma physics (Chisham *et al.*, 2007). Along with the main array of 16 antennas, several SuperDARN radars, such as the one at SANAE IV, are equipped for elevation interferometry by means of another array of 4 antennas placed 100 meters from the main array. The purpose of this array is to detect the elevation angle of HF radar reflections from the ionosphere by using the phase difference between the signals received by the two arrays. The beam pattern, one of the array parameters to be verified, requires an external signal source, at least a few kilometers away, due to the long wavelength at which the array operates. A signal source on
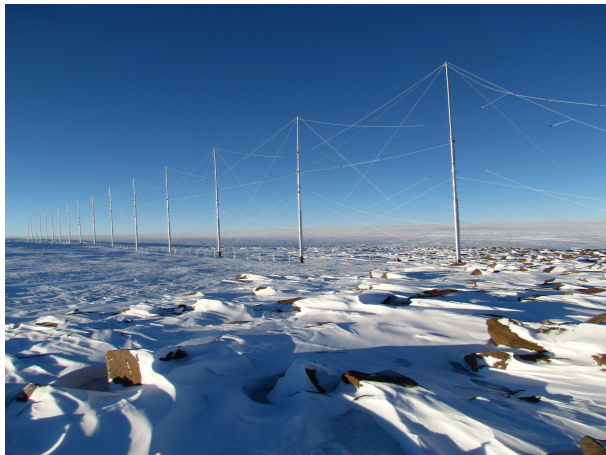
Figure 1.2: The main SuperDARN antenna log periodic array at SANAE IV and 4-element interferometer array 100 m north of the main array (SANAP and SANAE, 2012)

a satellite is a potential solution since the exact position of the satellite can be determined from its orbital parameters and the ray path from the satellite to the receiver inferred from ionospheric ray tracing.

Two things are needed to characterise the beam pattern: the angle of arrival in both azimuth and elevation and the relative power at each angle of arrival. Currently the HF radar has a built-in algorithm for steering the beam in azimuth and thus selecting the angle of arrival in azimuth. The elevation angle of the incoming signal can theoretically be determined from the phase difference between the signals received by the main array and the interferometer array, located 100 m north of the main array. Due to some unknowns in the signal path through the HF radar receiver, and the ambiguity in relating the phase difference to the elevation angle, there is currently no proven technique to extract the elevation angle from the signals available on the output of the SuperDARN radar.

Therefore, the proposed means to calibrate the elevation algorithm and characterise the beam pattern is an HF beacon on a low-Earth orbit (LEO) satellite which can potentially be used for determining both the algorithm for inferring phase angle from the outputs of the SuperDARN radar and the beam pattern of the antenna. Beam pattern measurements can be done either by near-field measurements and doing a Fourier transform to convert the near-field to a far-field pattern, or by means of far-field measurements as proposed in this research.

However, the signal will experience refraction as it propagates through the ionosphere. Hence, the location of the satellite relative to the receiver is not sufficient for finding the elevation angle. The actual angle of incidence after refraction by the ionosphere can be determined by ray tracing. Ray tracing only requires information about electron density and

height of layers in the ionosphere along the ray path, which can be obtained from a model as described in Chapter 4. It is important to note that there are some uncertainties to this approach due to the simplifying assumptions made in the software for ray tracing. Table 1.2 gives a summary of the parameters of the HF radar ground station at SANAE IV.

Table 1.2: Parameters of the HF radar ground station at SANAE IV taken from Visser (2009).

Modulation type	BPSK
Spectral Efficiency [bits/s/Hz]	0.7
Transmission rate [kbit/s]	5
Receiver IF bandwidth [kHz]	0.7
Boltzmann constant [J/K]	1.4E-023
Receiver antenna noise temperature [K]	1.5E+05
Receiver noise figure [dB]	5
Receiver noise temperature [K]	627
Receiver system noise temperature [K]	1.5E+5
Receiver system noise temperature [dB]	51
Receiver IF bandwidth [dB]	28.54
Receiver noise floor [dBm]	-118
GS RX antenna gain [dBi]	0

1.3.2   Direction-finding systems in Hermanus and Pretoria

An HF DF receiver to be built at SANSA Space Science in Hermanus, South Africa, will be used to decode the signals from ZACUBE 1 and to verify the refraction and polarisation change of the signals through the ionosphere. Proposed location of the DF equipment at SANSA is 34°25′29.60″S 19°13′25.03″E.

The data obtained at SANSA will be used for ionospheric characterisation which is key to the interpretation of the data from the SuperDARN radars. This will be done by ray tracing through the ionosphere to characterise the exact locations from where the reflections detected by the radars occur. Such ray tracing requires an accurate description of the refractive index along the ray path, which in turn depends on the electron density distribution in the ionosphere.

A DF receiver is to be built at SANSA, because the instruments for characterising the electron density in the Antarctic ionosphere are few and far between. A small number of ionosondes are in operation, but none near SANAE IV or other SuperDARN radar locations. Dual frequency global positioning system (GPS) receivers which could also be used for ionospheric characterisation are only available at a few locations in Antarctica and even fewer

in the Arctic region, where there are no suitable locations for the installation of permanent terrestrial instruments. However, SANSA is a suitable location to build the DF receiver as it will be close to an ionosonde, which gives the ionospheric characteristics in real time.

The DF instrument available at Grintek Ewation in Pretoria is located at 25°44′41.72″S 28°16′15.46″E. All the receiver stations are shown in Figure 1.3.
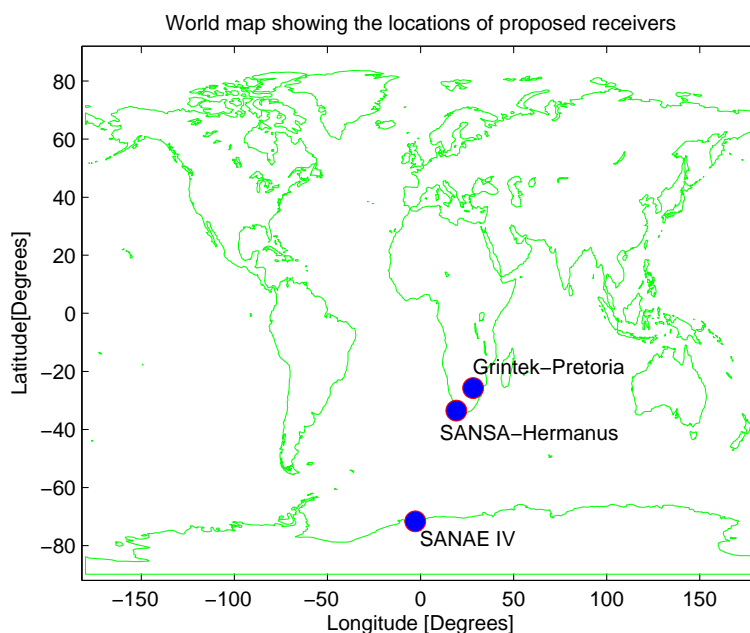
Figure 1.3: Geographic locations of the receivers at SANAE IV, SANSA and Grintek

1.4 Previous attempts to calibrate the HF radar at SANAE IV

In order to characterise the elevation angles of the HF radar return signals and the beam pattern of the antenna arrays of the SuperDARN radar at SANAE IV, one needs to understand fully the known characteristics of the transmitter on the CubeSat, the radar receiver, the ground plane properties and the calibration method being proposed.

In 2007, the elevation detection algorithm of the radar at SANAE IV was calibrated by means of an HF transmission at 13.125 MHz from a helicopter at an altitude of 1 km and 3 km using selected elevation angles (Cilliers, 2007). The objective of the experiment was to determine the calibration curve of the phase shift between the signals received by the main array and the interferometer array against elevation angle. Figure 1.4 describes the geometry of the elevation angle calibration.
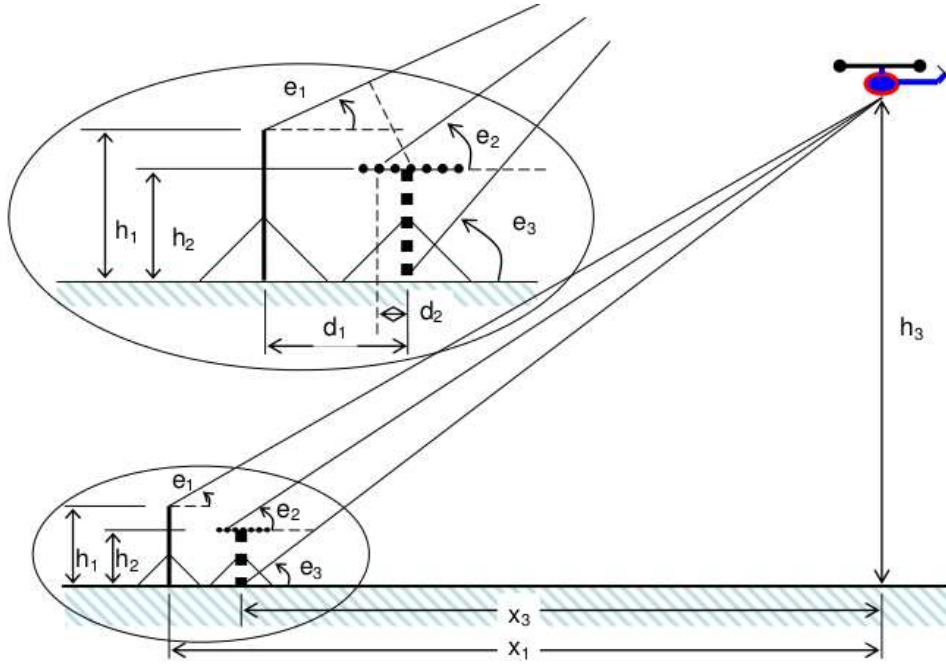
Figure 1.4: HF radar calibration geometry (Cilliers, 2007)

The assumptions made were:

1. the elevation angles are equal, that is $e_1 = e_2 = e_3 = \tan^{-1}(h_3/x_3)$

2. and the centres of the two arrays are at the same height ($h_1 = h_2$)

For a first approximation, a theoretical approach was taken, whereby the phase delay associated with the propagation path difference between the main array and the dipole interferometer array phase centres is approximated by Equation 1.5. This was called Model 1.

$$P = \frac{d_1 \cos e_1}{\lambda} 360^\circ, \tag{1.5}$$

where λ is the wavelength at the transmission frequency and d_1 is the perpendicular distance between the two arrays equal to 100 m.

For the second approximation (Model 2), which was expected to have a greater accuracy, the propagation distance from the helicopter to the centre of each of the antennas and the propagation time to the centre of the dipole array were calculated. The phase delay was then derived from the difference between the propagation times as a fraction of the period of the carrier wave as shown in Equation 1.6.

$$P = \frac{t_1 - t_2}{T} \times 360^\circ, \tag{1.6}$$

where t_1 is the propagation time to the centre of the dipole array, t_2 is the propagation time

to the centre of the main array and T is the period of the carrier wave.

None of the measured phase shifts matched the theoretical results and also the measured results did not seem to follow a consistent pattern as illustrated in Figure 1.5. In this figure, theoretical and measured phase-shift values were plotted against elevation angles, giving rise to the curve with markers at sampled elevations, with an optimum value for the hardware phase shift of -87°. The optimum phase shift was determined by means of a least-squares fit to the data after adding multiples of 2π through trial and error to each of the measured phase points. The continuous curve shows results from Model 1, while green markers were used for Model 2 and red markers for δt. Details of this experiment can be found in Cilliers (2007).
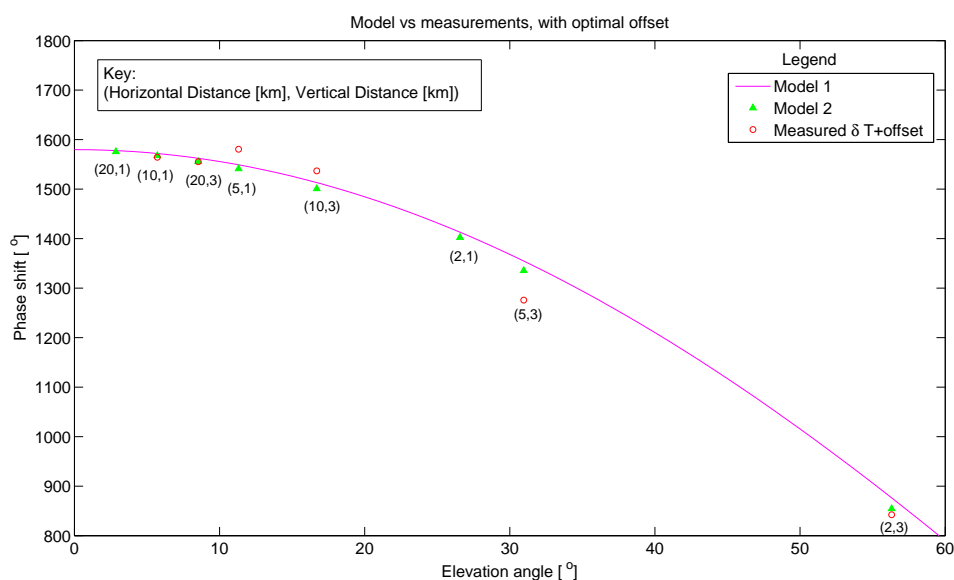
Figure 1.5: Theoretical and measured phase-shift values against elevation curve with markers at sampled elevations (Cilliers, 2007).

This attempt to characterise the elevation algorithm and the beam pattern of the SANAE IV HF radar antenna by means of an HF transmitter on a helicopter failed due to logistical problems which prohibited the continuous transmission of the HF signal (Cilliers, 2007).

A similar attempt to characterise the SuperDARN radar at Saskatoon in Canada (52.16°N, 106.53°W) using a transmitter on board an airplane, experienced major logistical complications which prohibited the successful execution of the mission. Details are given in Sterne (2010). Although there have been satellites in the past which had HF beacons on board such as Sputnik, there are currently no operational satellites with suitable HF beacons for the calibration of the SuperDARN HF radar antennas.

1.5   Structure of the dissertation

Chapter 2 contains a review of the literature that supports the theory behind HF ray tracing through the ionosphere. The chapter starts off with a brief description of ray tracing and mentions some of the areas to which it has been applied. Since the rays propagate through the ionosphere, a general overview of the major processes in the ionosphere is given. It is then elaborated that the F-region of the ionosphere contains most electrons, thus there are greater propagation effects in terms of refraction in that region.

The effects of refraction, reflection, polarisation, attenuation and multipath of the waves are described with reference to the layer of the ionosphere where the specific effect dominates. Refraction, reflection and polarisation, being the most common phenomena to affect radio propagation, are described in detail using Snell's law and the Appleton-Lassen equation. Figure 1.6 illustrates the effects of angular deviation, polarisation and multipath of radio waves.
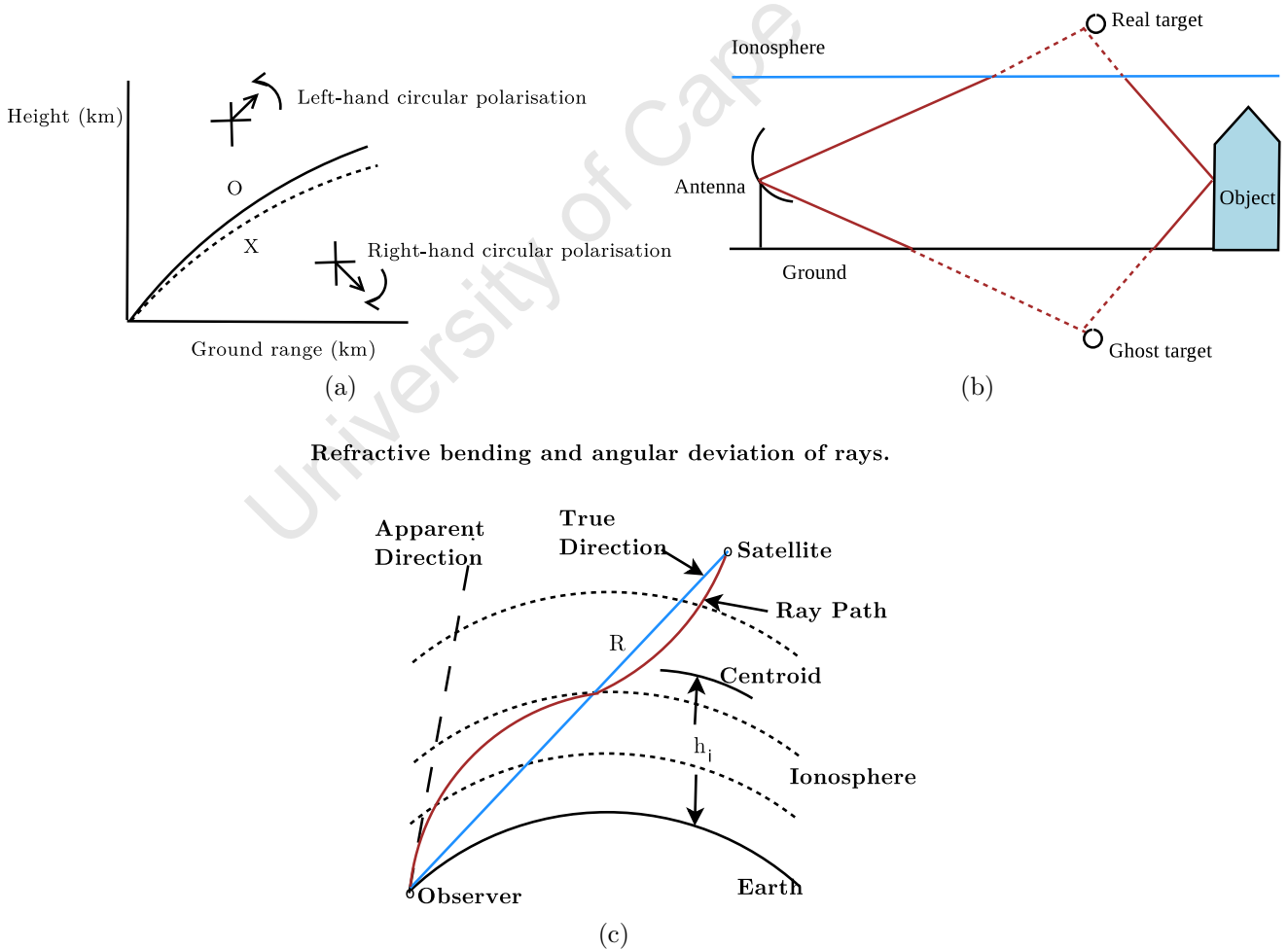
Figure 1.6: Figure illustrating polarisation (a), multipath (b) and angular deviation (c) of radio waves.

Since the ionosphere is constantly varying, the best and most common way of understanding it is by means of ionospheric models. The types of commonly used models are described briefly. The two models used in this work are the IRI-2007 model and Chapman layer model. It is known that the ionosphere has diurnal, seasonal, geomagnetic and geographical variations. A trend similar to that of the ionospheric effects is observed in the ray tracing results, especially seasonal variation as discussed in Chapter 4.

The results of the orbit analysis are given in Chapter 3. The chapter begins with a brief overview of commonly used orbit analysis algorithms. The theory behind the orbit analysis MATLAB programme and the parameters used are described. Here the inputs to the orbit analysis algorithm and their importance towards defining an orbit are discussed. These inputs include: inclination, perigee, apogee, Earth's rotation speed, semi-major axis, orbital period and eccentricity.

The satellite orbit was propagated for 14 orbits which constitute about one day. The projection of the orbits onto the Earth's hemisphere is plotted for the inclination angles of 97.8° and 65° over SANAE IV, Hermanus and Pretoria, as shown in Figures 3.1, 3.6 and 3.10 respectively. The ground trace was plotted in the azimuth-elevation plane with the radar beam for the main SuperDARN interferometer array at SANAE IV superimposed to show how much of the radar beam is traversed by the orbit (Figure 3.2).

The satellite passes that intersect the radar field of view of SANAE IV and over Hermanus and Pretoria are considered significant passes. For each of these significant passes, the amount of refraction expected in the best (midwinter) and worst (midsummer) propagation conditions was calculated and plotted in Figures 3.5, 3.8 and 3.12 for SANAE IV, Hermanus and Grintek respectively. Figures 3.5, 3.8 and 3.12 show the variation of the satellite's elevation and azimuth with time over SANAE IV, Hermanus and Pretoria respectively. Figure 1.7 shows the orthogonal projection of the orbits over SANAE IV and the azimuth-elevation plot of the visible satellite passes of these 14 orbits at an inclination of 97.8°.

In Chapter 4, the theory behind the ray tracing algorithms is described in detail. The equations and assumptions used in the MATLAB programme for ray tracing are given. Using Snell's law to account for refraction of the ray path from the relationship between refractive index and electron density, apparent elevation angles are calculated from true elevation angles. The algorithm considers a single-layer, uniform electron density model (Model 1) and multilayer model (Model 2) for both flat Earth and spherical Earth approximations. Here the ray tracing was done from the receiver on the ground to satellite beacon. In the 'top-down' method (Model 3), the ray tracing is similar to that in Model 2, except now

(a)   (b)
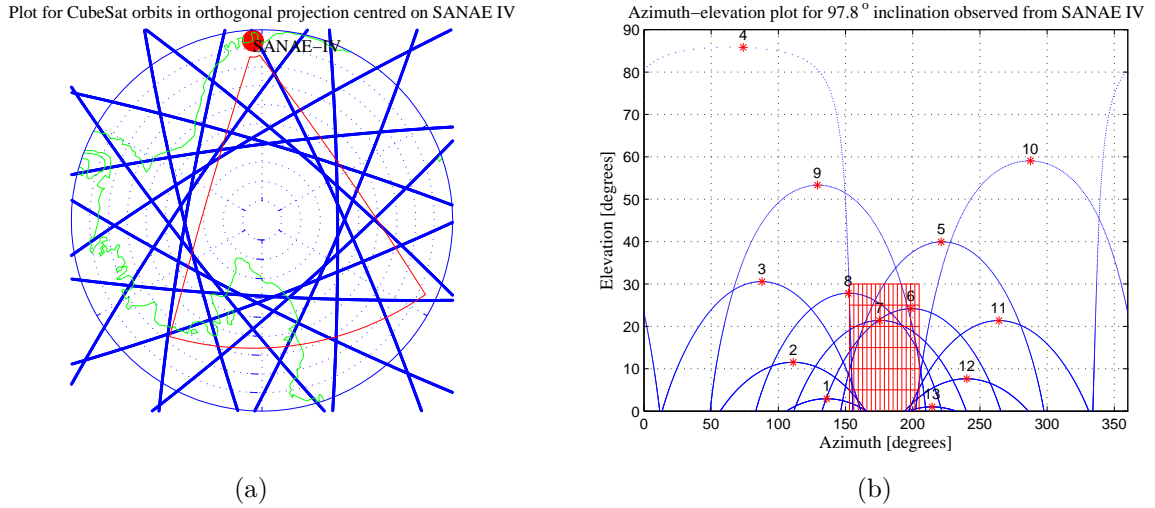
Figure 1.7: Projection of 14 orbits at inclination of 97.8° onto the Earth's hemisphere (a) and in the azimuth-elevation plane (b) over SANAE IV. The area shaded red is the azimuth-elevation coverage of the radar.

(a)   (b)
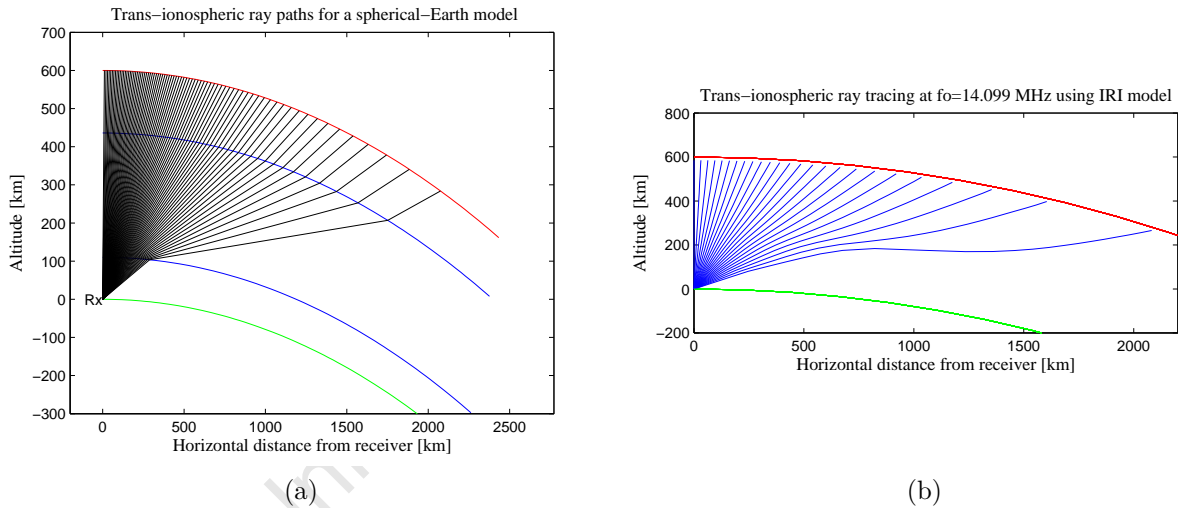
Figure 1.8: Trans-ionospheric ray paths at 14.099 MHz for the spherical Earth, single-layer (a) and multilayer (b) models for midsummer on 1 January 2011 at 12:00 UT.

the rays are traced from the satellite beacon to the receiver on the ground. In all cases, the ionosphere is defined using the IRI-2007 model and the worst (midsummer) and best (midwinter) propagation conditions are considered. For all the models, the flat Earth (a) and spherical Earth (b) approximations are used. Figure 1.8 shows ray paths as obtained by Model 1b and 2b during midsummer.

The results obtained from Model 1 and Model 2 are comparable and there are no significant changes in the true and apparent elevation angles of the signal. However, there is a significant difference in the angle of arrival and number of rays that traverse through the

13

ionosphere for the worst and best propagation conditions.

The Haselgrove ray tracing technique as a means of evaluating the accuracy of the results obtained by the simpler models 1, 2 and 3 is then described. The Haselgrove algorithm also shows the separate ray paths for ordinary (O) and extraordinary (X) modes of the wave due to polarisation as a result of the presence of a magnetic field. In the results, most of the rays from the two modes of propagation pass through the ionosphere to reach the satellite altitude and in summer some appear to bounce off the ionosphere due to reflection. At the end of the chapter, the true and apparent elevation angles derived from ray tracing Model 2b and the Haselgrove algorithm were plotted for comparison in Figure 4.24. Figure 1.9 shows ray paths derived from the Haselgrove ray tracing algorithm, using the IRI model for summer (a) and winter (b) respectively.
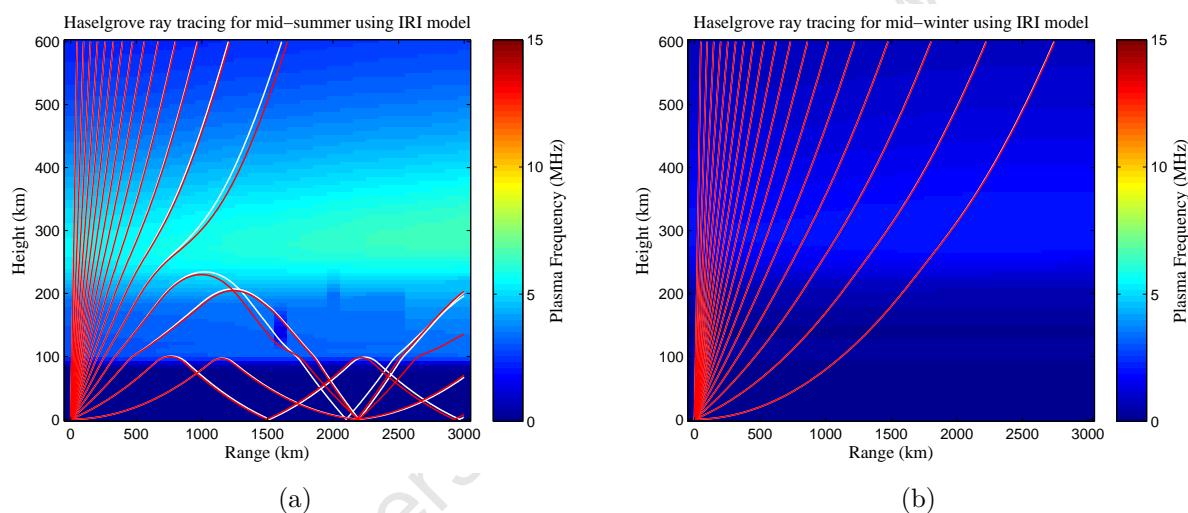
Figure 1.9: Trans-ionospheric ray paths derived from Haselgrove ray tracing algorithm at 14.099 MHz using the IRI model for midsummer on 1 January 2011 at 12:00 UT in (a), and midwinter on 1 June 2011 at 23:00 UT in (b) respectively.

In Chapter 5, the results of the orbit analysis are discussed with reference to the ground stations at SANAE IV in Antarctica, Grintek in Pretoria and the proposed HF DF equipment to be built at SANSA in Hermanus. Here the ray tracing results of the best model (Model 2) and the Haselgrove algorithm show a good correlation for the true and apparent elevation angles. The proposed orbit is a LEO at an inclination of 97.8°, the proposed ionospheric model is the spherical Earth top-to-bottom multilayer model and the time of the year to characterise the radar and perform ionospheric characterisation is midnight in winter and midday in summer, respectively. In conclusion, suggestions for future research are made.

Chapter 2

HF propagation through the ionosphere

Signal propagation is the behaviour of the signal in the form of a wave from the transmitter to the receiver through the ionosphere. It is always affected by the refraction of the electromagnetic wave carrying the signal. Propagation of HF waves through the ionosphere enables HF communication, which has been in use by the navy, military and researchers since the 17th century (Kimura, 1966). HF propagation can be ground to ground or satellite to ground or ground to satellite propagation. The HF signal will be propagated from a beacon transmitter on the CubeSat to the SuperDARN radar or to the HF DF receivers in Hermanus and Pretoria. The beacon will transmit at a frequency of 14.099 MHz.

Due to the properties of the ionosphere, which are discussed in detail in the next sub-section, radio waves propagating through the ionosphere are refracted and so they can travel over great distances around the globe. In order to simulate the propagation of radio waves, extensive knowledge about the ionosphere as the medium of propagation is required. In this study, the assumption is made that below about 60 km in the lower atmosphere, electromagnetic waves traverse in a straight line trajectory, because the refractive index remains at a constant value close to unity at high frequencies.

2.1   General overview of the ionosphere

The ionosphere is the region of the Earth's atmosphere extending from a height of about 60 km to about 1000 km. This region of the atmosphere is characterised by an abundance of charged particles (Kohl *et al.*, 1996). Electrons in the ionosphere are a result of a process of photo-ionisation of the neutral atoms by solar extreme ultraviolet (EUV) radiation and X-rays. Since the process of photo-ionisation is largely dependent on the sun, variations in the solar zenith angle to the Earth affect the rate of ionisation. Therefore, when the rate of

ionisation reduces at night, a reverse process known as recombination takes over, reducing the electron density in the ionosphere as explained by Kohl *et al.* (1996).

The process of recombination occurs in two forms: radiative and dissociative recombination. In radiative recombination, the electrons combine directly with positively charged ions, converting them into neutral atoms and leading to lack of mobility. Dissociative recombination occurs in two stages and is the more efficient process. In the first phase of dissociative recombination, positive ions from photo-ionisation interact with the numerous neutral molecules, replacing one of the atoms in the molecule. In the second phase, electrons combine with positively charged molecules, giving two neutral atoms.

These competing processes of photo-ionisation, recombination and other effects due to cosmic radiation, magnetospheric electric fields and particle precipitation determine the structure of the ionosphere (Ratcliffe, 1997). The resulting difference in electron density, chemical composition, level of ionisation and variability at different heights divides the ionosphere into different regions or layers. Changes in ionospheric ionisation are caused by diurnal and seasonal variation, solar activity, as well as geomagnetic activity. The different layers of the ionosphere are described in the next sub-section.

2.1.1   Layers of the ionosphere and their effect on radio waves

D-Layer: The D-layer is the lowest region of the ionosphere, between approximately 60 km to 90 km above the Earth's surface. The level of ionisation is relatively low because the intensity of solar radiation reaching these altitudes is very small and as a result, the electron density is low (Giraud and Petit, 1978). Ionisation almost entirely depends on Lyman alpha and hard X-rays. At night, there is almost no ionisation in this layer so the electron density layer reduces significantly after sunset, but does not disappear due to the ionisation effect of galactic cosmic rays.

When a radio wave travels downwards from the upper ionosphere to the Earth's surface, the D-region is the last region of the ionosphere that it traverses. During the day, the D-layer is responsible for attenuation of radio waves due to collisions of free electrons with molecules, leading to energy loss which manifests as an overall reduction in signal strength. Attenuation of radio signals also results from its spherical spreading during propagation since the power density of an electromagnetic wave is inversely proportional to the square of the distance between the transmitter and the receiver (Budden, 1985). The amount of attenuation is dependent upon a number of factors, some of which include:

1. The number of gas molecules: the greater the number of gas molecules, the higher the

number of collisions, the larger the attenuation rate.

2. The level of ionisation: the higher the level of ionisation, the greater the number of electrons that vibrate and collide with molecules.

3. The frequency of the signal: as the frequency increases, the wavelength shortens, and the number of collisions between the free electrons and gas molecules increases. As a result, signals at higher frequencies are attenuated more than those at lower frequencies as shown in Equation 2.1.

$$\text{Attenuation} = \alpha L f \tag{2.1}$$

where α is the attenuation constant in dB/MHz/cm, L is the length of the medium in cm and f is the frequency of the transmitted signal in MHz.

E-Layer: The E-layer is the region directly above the D-region and extends between altitudes of about 90 km to 120 km. The ionisation in this region is stronger than in the D-region. The E-region is characterized by a peak electron density near $105 - 110$ km and ionisation is by soft X-rays and some EUV radiation (Bilitza, 1998). At night the E-layer almost disappears because the primary source of ionization, which is the sun, is absent.

As the signal passes through the E-region, fewer collisions occur since the air density is low at these altitudes. This means that when the free electrons are excited by radio signals and vibrate, fewer collisions occur. However, some of the electrons are set in motion by the radio signal, but they tend to re-radiate the kinetic energy. A signal propagating in an area with increasing electron density is refracted away from the normal as it enters an area of higher electron density.

F-Layer: The F-region is immediately above the E-region, and extends to well above 300 km. This layer contains the greatest density of free electrons, making it the most important for long distance signal propagation. Ionisation here is mainly due to photo-ionisation of atomic oxygen by EUV solar radiation. During daylight hours the F-region is divided into two sub-layers, the F1 and F2 layers, but at night it is mainly one layer. The F2-layer is at a higher altitude and the electron density is greater than that in the F1-layer and any other region of the atmosphere (Giraud and Petit, 1978).

Due to the high electron density in this region, HF waves propagating through the F-region causes the most refraction of all the regions of the ionosphere. HF signals traveling from a satellite to ground in the F-region can be bend them back into space by the refraction. In effect, it appears that the region has 'reflected' the signal and this effect is significant,

because the F-region is present throughout the day and night. As the frequency of the propagating signal increases, the amount of refraction decreases until a frequency is reached where the signal passes through the F-region to the E-region. More details on the F-region dynamics can be found in Ratcliffe (1997).

2.2   Radio propagation effects

The effects experienced by radio waves during propagation through the ionosphere allow them to reach areas which would not be possible if the radio signals traveled in a direct line. However, this can be a problem if the waves do not propagate to the intended receiver position (Budden, 1985). In the following sub-sections, the major effects on radio wave propagation are discussed in detail.

2.2.1   Refraction

Refraction is the most important effect on radio wave propagation and it is caused by a wave traversing through regions with varying refractive indices. Fermat's principle of refraction describes the path taken by an electromagnetic wave, such as a radio wave, as the path that can be traversed in the shortest time. By minimising the time of propagation, Snell's law of refraction is derived from Fermat's principle (Stroyan, 1999), as illustrated in Figure 2.1. The total time of propagation through the two media t is given by;
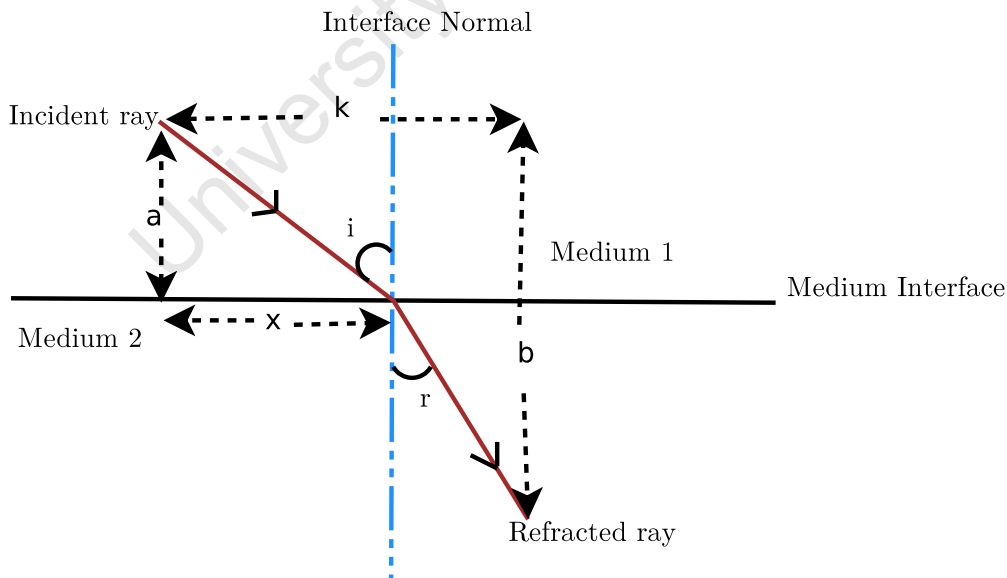
Figure 2.1: Diagram illustrating refraction of a radio wave

$$t = t_1 + t_2, \tag{2.2}$$

where t_1 is the time of propagation through medium 1 and t_2 is the time of propagation through medium 2.

$$t = \frac{\sqrt{a^2 + x^2}}{v_1} + \frac{b^2 + (k - x)^2}{v_2}, \tag{2.3}$$

$$\frac{dt}{dx} = \frac{x}{v_1\sqrt{a^2 + x^2}} - \frac{k - x}{v_2\sqrt{b^2 + (k - x)^2}}, \tag{2.4}$$

$$\frac{dt}{dx} = \frac{\sin i}{v_1} - \frac{\sin r}{v_2}. \tag{2.5}$$

By minimising time (let $\frac{dt}{dx} = 0$) and substituting $n = c/v$, Snell's law, which is given by Equation 2.6, is obtained.

$$\frac{\sin i}{\sin r} = \frac{v_1}{v_2} = \frac{n_1}{n_2} \tag{2.6}$$

The symbol i represents the angle of incidence measured from the normal, n is the refractive index of the respective medium, v is the phase velocity of the wave, that is the rate at which the phase of the wave propagates in the respective medium. In the ionosphere, the refractive index is directly proportional to electron density, as shown in Equation 2.7.

$$n = \sqrt{1 - \frac{(f_p)^2}{(f_0)^2}} \tag{2.7}$$

where f_p is the plasma frequency $\approx 8.980\sqrt{N_e}$ in MHz for electron density (N_e) in electrons/m^3 and f_0 is the frequency of the incident ray (14.099 MHz). After a radio signal has been refracted through several layers of the ionosphere, the elevation angle measured at the receiver is nolonger the true elevation angle, but apparent elevation angle. Elevation angle is defined as the angle between the horizontal plane and the line of sight along the ray path, measured in the vertical plane. And it is positive above the horizon (0° elevation angle), but negative below the horizon.

Two of the errors associated with refraction are range error and angular error. Figure 2.2 shows the effect of refraction on a ray propagating from a satellite to the ground and the errors that arise due to this effect (Davies, 1990). Range error due to the ionosphere ρ in radians is given by:

$$\rho = c\delta T \tag{2.8}$$

where, c is the speed of light in a vacuum in ms^{-1} and δT is the excess time delay in seconds of the signal over and above that of free space, given by;

$$\delta T = \frac{40.3 N_T}{f^2} \tag{2.9}$$

Refractive bending and angular deviation of rays.
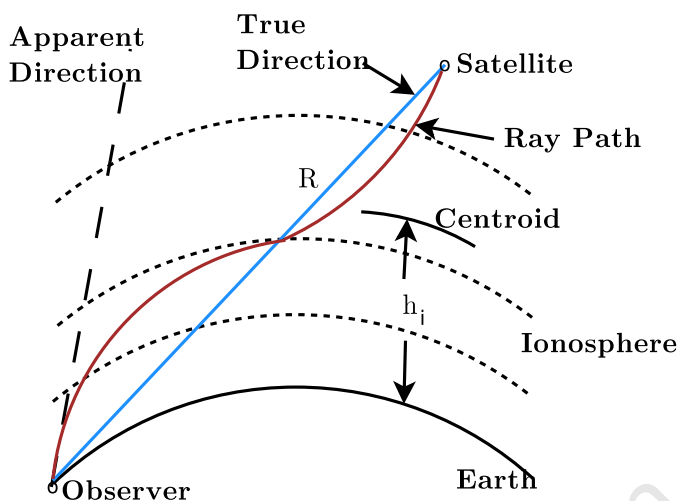
Figure 2.2: Ray Path from a satellite to ground showing refractive bending and angular deviation

and f is the frequency in Hz, N_T is the TEC in electrons/m^2. Angular error ξ for small values of true elevation angle is given by;

$$\xi = \frac{\rho \cos \Delta}{2 h_i}. \tag{2.10}$$

For large values of true elevation angle and R$<<$R$_e \sin \Delta$, the angular error is given by;

$$\xi = \frac{\rho \cot \Delta}{R}, \tag{2.11}$$

where Δ is the true elevation angle, R is the range from the observer to the satellite, R$_e$ is the Earth's radius and h$_i$ is the height of centroid of electron density profile (usually between 300 and 450 km) (Davies, 1990).

2.2.2   Reflection

Reflection is the change in direction of a wavefront at an interface between two different media so that the wavefront returns into the medium, from which it originated. Assuming a spherically symmetric ionosphere, continued refraction can be modeled as reflection by postulating a virtual reflection height and applying the laws of reflection, which are:

1. The incident ray, the reflected ray and the normal to the reflection surface at the point of incidence lie in the same plane.

2. The angle which the incident ray makes with the normal is equal to the angle which the reflected ray makes to the same normal.

3. The reflected ray and the incident ray are on opposite sides of the normal.

However, in the case of a real ionosphere, the ionospheric electron density is not the same along the ray paths towards and away from the reflection point and hence the second law of reflection does not apply. And due to the inhomogeneities in the ionosphere, the rays do not travel in a plane, and so the first law of reflection does not apply either (Budden, 1985). Radio waves can be reflected off layers of the ionosphere or any other objects in the Earth's atmosphere.

2.2.3 Polarisation

Change in polarisation, an inherent property of an electromagnetic wave along the ray path, is due, among other things to the magnetic field which causes the O and X modes of the waves to separate and interact in such a way as to change the polarisation of the wave between the point of transmission and reception (Davies, 1990). In the E and F-layers of the ionosphere, where the wave frequency is much smaller than the electron collision frequency, the frictional force due to collisions is negligible compared to the electrostatic and Lorentz forces. The phase refractive index is defined by the Appleton-Lassen equation. The Appleton-Lassen equation, given in Equation 2.12, is a form of dispersion relation used to describe the phase refractive index in the ionosphere (Budden, 1985).

$$n^2 = 1 - \frac{X}{1 - \frac{\frac{1}{2}Y^2 \sin^2 \theta}{1-X} \pm [(\frac{\frac{1}{2}Y^2 \sin^2 \theta}{1-X})^2 + Y^2 \cos^2 \theta]^{\frac{1}{2}}} \tag{2.12}$$

where n is the phase refractive index given by:

$$n = \frac{c}{V_{ph}}, \tag{2.13}$$

V_{ph} is the phase velocity and c is velocity of light in a vacuum.

$$X = \frac{\omega_0^2}{\omega^2} \tag{2.14}$$

ω_0 is the electron plasma frequency, ω is the angular frequency,

$$Y = \frac{\omega_H}{\omega}, \tag{2.15}$$

ω_H is the electron gyro frequency and θ is the angle between the ambient magnetic field vector and the wave vector.

The plus and minus sign for the refractive index, calculated by taking the square root of Equation 2.12 indicates that the complex refractive index may take on two different values.
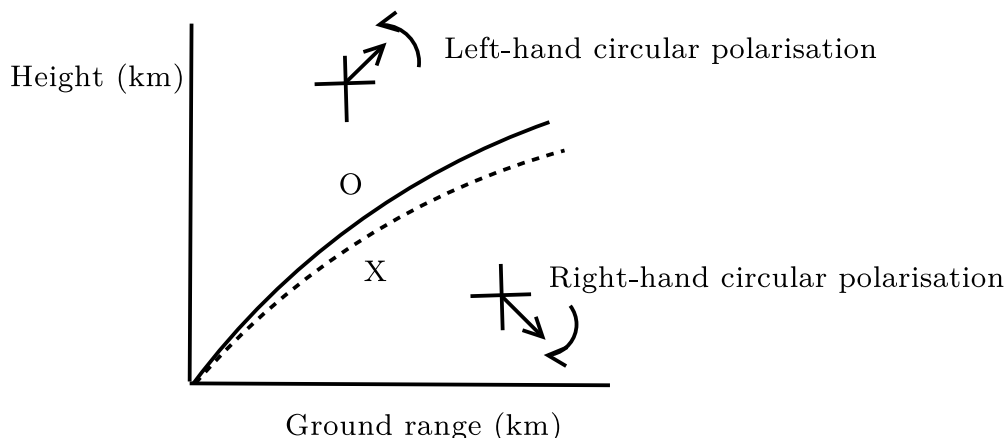
Figure 2.3: Diagram showing the O and X modes of radio waves as a result of polarisation

This means that the medium supports two characteristic modes of propagation, commonly referred to as the O and X waves. When the wave frequency is low, there is a third propagation mode which does not occur for HF propagation (Davies, 1990).

Consider a plane polarised wave propagating parallel to the magnetic field. The positive sign represents a left-hand circularly polarised mode, and the negative sign represents a right-hand circularly polarised mode. The ray paths of the O and X waves will appear as illustrated in Figure 2.3. In the absence of electron collisions, O and X waves have different wavelengths, phase speeds and opposite senses of rotation (Davies, 1990). The different characteristics of the ordinary and extra-ordinary waves result in the rotation of the electric field vector, leading to Faraday rotation.

2.2.4   Doppler shift

Doppler effect is the shift in frequency of the return signal from a target or other object as a result of the object's radial motion relative to the receiver. Doppler effect constitutes two parts, one due to motion of the satellite with respect to the receiver and another due to the rate of change of TEC along the path. For low Earth orbiting satellites, the Doppler shift of a wave is expressed by Equation 2.16;

$$\Delta f = \frac{f \mathrm{n}_s \nu_l}{c} + \frac{40.3}{\mathrm{c} f} \frac{dN_T}{dt} \tag{2.16}$$

where f is the frequency, n_s as the refractive index at the satellite, ν_l is the line of sight component of the satellite velocity, $\frac{dN_T}{dt}$ is the rate of change of TEC and c is the the speed of light in a vacuum. Note that these shifts in frequency are generally insignificant compared to the frequency of propagation, especially with HF signals. Doppler shift is important in HF beacon transmission due to the shift in the frequency during the approaching and

receding phases of the orbit (McNamara, 1991). This requires sufficient receiver bandwidth to accommodate the range of frequencies from the frequency of transmission plus or minus the Doppler shift.

2.2.5   Multipath and Ducting

Multipath is a propagation phenomenon that occurs when radio waves reach the receiving antenna by more than one path. This effect leads to a reduction in the received signal power, interference and phase shift. Some of the causes of multipath are; ducting, ionospheric reflection, reflection from other objects (water bodies, mountains and buildings) and refraction (Haslett, 2008).

Ducting occurs when a radio wave propagates in a horizontal direction following the Earth's curvature, particularly at the E-F valley in the ionosphere. When there is a steep gradient in the refractive index over a small altitude interval, a plane of high refractive index is sandwiched between regions of lower refractive index and the radio wave is trapped in this region (Haslett, 2008). Over large distances and beyond the horizon, where the signal strength is normally low, ducting leads to enhancement of the signal strength.

Multipath creates the problem that to 'ghost' targets are seen by the radar receiver as illustrated in Figure 2.4. Thus the real target signal has to be isolated from the 'ghost' target signal. This problem can be resolved by creating a ground map of the radar's surroundings and eliminating all 'echoes' which appear to originate below the ground and above the height of the signal source (Davies, 1990). Using more than one antenna to receive the signal can also mitigate the effect, since the multipath effect may not occur in all the antennas simultaneously.

2.2.6   Fading of radio signals

Fading of radio signals is caused by the fluctuation in signal amplitude as it propagates from the transmitter to the receiver, and it can occur in the form of multi-path or single path fading. The faded signals present random temporal fluctuations in both amplitude and phase when received at an antenna. This effect is difficult to eliminate due to its unpredictable nature (Budden, 1985). The variations in the ionosphere cause reduction of the amplitude of the signal, sometimes to a level below which the signal cannot be detected. In HF transmission, signal fading can be minimised by a high power transmitter such that the signal is still detectable when it reaches the receiver. The effect of signal fading is closely related to ionospheric scintillation where irregularly structured regions in the ionosphere cause diffraction of trans-ionospheric radio signals. Reflection of radio waves can also lead
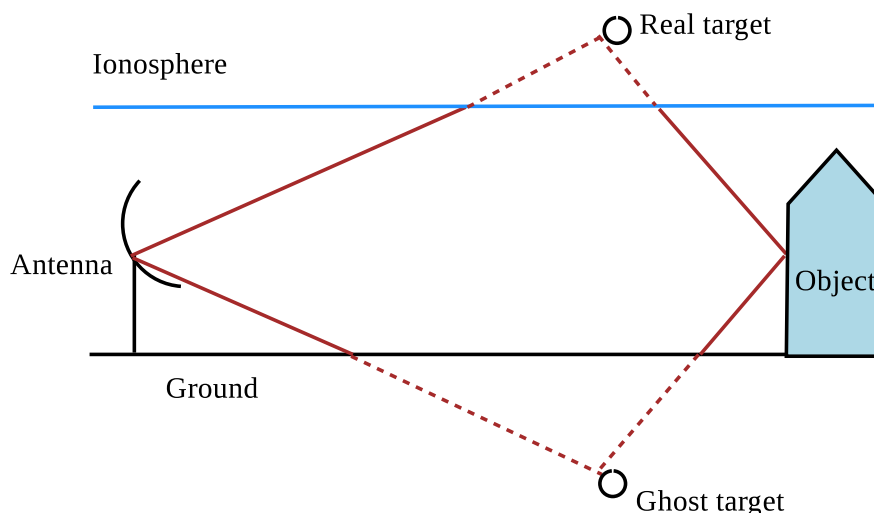
Figure 2.4: Diagram illustrating multipath of radio waves

to signal fading since the strength of the reflected wave is less than that of the incident wave (McNamara, 1991).

2.3   Modelling the ionosphere

The ionosphere can be described by four parameters: electron density, electron and ion temperatures, and ionic composition. Signal propagation depends uniquely on electron density and this parameter is of greatest interest in the present context. Electron density in the ionosphere depends on a number of parameters, which include altitude, latitude, longitude, time, season, solar activity and geomagnetic activity (McNamara, 1994). Because of the complicated nature of the ionosphere, there have been numerous approaches towards modelling the ionosphere over the years. Some of the models are discussed in the following sub-section.

2.3.1   Empirical models

These models are expressed by means of parametrised equations which do not have any direct link with the physics, but are derived from best-fit to available data, based on extensive worldwide data sets from ionosondes, rockets, satellites, and incoherent scatter radars (Chiu, 1975). These models describe not only the ionospheric parameters, but also the magnetospheric parameters underlying the effects. Currently, there are empirical models that describe ionospheric ion and electron temperatures (Rawer and Bilitza, 1989), and auroral conductivities (Hardy *et al.*, 1987). The IRI model (Bilitza, 2001), the IONCAP and the NeQuick models are some of the empirical models that have been developed.

2.3.2   Analytic models

These are physics-based models described by equations of which the parameters are derived from data in a closed form solution, known as a mathematical analytic function. Analytical models are based on orthogonal function fits to the output, obtained from numerical models, most of which have been developed separately for low, middle and high latitude regions of the ionosphere. An example is the Fully Analytical Ionospheric Model (FAIM) (Anderson *et al.*, 1989).

2.3.3   Assimilative models

Assimilative models are either empirical or analytic models driven by real-time ionospheric inputs (Schink 1988). Such models have recently been developed with a strong interest in data-driven specifications and forecast. An example is the Parameterised Real Time Ionospheric Specification Model (PRISM) based on ionosonde and satellite data.

2.3.4   The IRI model

The IRI model is an empirical standard model of the ionosphere based on available ground and space data sources and using theory to bridge data gaps to describe ionospheric density and temperature (Bilitza, 2001). The major data sources for IRI are the worldwide network of ionosondes, incoherent scatter radars and topside sounders. Several editions of the model have been released. The model is updated yearly and the latest version is IRI 2011 which has the option to use NeQuick as the topside model.

For a given location, time and date, the IRI model provides monthly averages of the electron density, electron temperature, ion temperature, and ion composition in the altitude range from 50 km to 2000 km (Chiu, 1975). This model can also generate TEC, predict the occurrence of spread F and the equatorial vertical ion drift (Bilitza, 2001). The IRI model is recommended for international use by the Committee On SPAce Research (COSPAR) and the International Union of Radio Science (URSI). For this reason and the fact that it has been widely used in ionospheric research, the IRI model was the predominant model used to define the ionosphere in this work.

2.3.5   Chapman layer model

The Chapman layer model is a theoretical model that describes the formation of the ionised layer in the atmosphere. The model describes the variation of electron density with height, provided certain assumptions are valid. These assumptions are: the ionisation radiation is

monochromatic, only one species of an atom or molecule is being ionised, and the temperature is independent of height (Davies, 1990).

By applying the above assumptions to the structure of the atmosphere and the incoming solar radiation, the Chapman layer model allows one to deduce the rate of ion production as a function of height and zenith angle of the incoming rays from the sun. Recombination or attachment are the processes that decrease the electron density distribution within the Chapman ionosphere. Important to note is that the D, E and F1 layers are very good Chapman layers, but sometimes the assumptions mentioned are not valid in the F2 layer. The Chapman layer model is used for Haselgrove ray tracing.

Chapter 3

Orbit analysis algorithm

Orbit analysis can be performed with free or commercial software or custom programmes. Available tools in use today include:

1. **MATLAB**, a numerical computing programming language developed by Mathworks. Several versions have been released since it was developed in the 1970s. To simulate the satellite's orbit, the 2009 version of MATLAB was used on a Windows-7 interface. The programme uses orbit parameters as inputs to give the ground trace of the satellite orbit in the required plane. This programming language was chosen because of its programming flexibility, ability to use a wide range of functions, its graphical interface and the fact that over the years, it has been successfully used in scientific research. Details can be found in Downey (2011). The major supplier of this software in South Africa is Opti-Num Solutions.

2. **Satellite Tool Kit (STK)** simulation tool is commercial software that has been widely used for validation of mission plans through simulation while being complemented by other tools (St-Pierre *et al.*, 2002). The development, support, sales of and training for STK is done by Analytical Graphics International (AGI).

3. **Satellite Orbital Analysis Program (SOAP)** is 'an interactive software system which employs 3-dimensional graphics animation to display the relative motion of satellites, airplanes, ships and ground stations' (Stodden, 1995).

4. **Environment for Visualising Images (ENVI)** was designed for data visualisation and analysis of images from aircraft and satellites. This software is produced by Exelis Visual Information Solutions Company. More details can be found in Exelis Visual Information Solutions (2012).

To perform orbit analysis, a number of orbital parameters need to be clearly understood. These include: the type of orbit, the inclination with respect to the equator, altitude, eccentricity, perigee and apogee position (Howard, 2010). For ZACUBE 1, the orbital parameters

act as input for the orbital analysis algorithm. In an ideal case, the CubeSat would pass over or very close to the Earth's poles in a near-polar orbit, with an ideal inclination of about 90° to the equatorial plane of the Earth, at an altitude of about 600 km and period of about 98 minutes. However, an ideal polar orbit may not be practically achievable since it requires an expensive dedicated launch opportunity. But the good news is that a LEO satellite can transmit a signal to be received on the ground and yet minimise the problem of drag that causes satellite orbits to decay over time. In the following analysis, two orbit inclinations which are at the time of writing potentially available for ZACUBE 1 are considered for the best and worst case scenarios. These orbit inclinations are 97.8° and 65° respectively, at an altitude of 600 km.

3.1   Theory of the orbit analysis algorithm

The orbit parameters for the CubeSat are listed in Table 1.1 and were used as input parameters for the MATLAB programmme. Below are the equations that describe the parameters in terms of the orbital mechanics of Kepler's motion (Serway and Jewett, 2010). The constants in this model are: Earth's radius, $R_e = 6378.134 \times 10^3$ m, Earth's rotation rate, dr$= 7.292 X 10^{-5}$ rad/s and Earth's equatorial surface speed in m/s (Michael, 2002).

$$v_e = dr \times R_e \tag{3.1}$$

Then the orbit is defined using perigee height H_1 in km (the closest orbit to Earth) and apogee height H_2 in km (the furthest orbit from Earth). Perigee radius in meters is given by Equation 3.2.

$$r_p = (R_e + H_1) \times 10^3 \tag{3.2}$$

And apogee radius in meters is given by Equation 3.3.

$$r_a = (R_e + H_2) \times 10^3 \tag{3.3}$$

The semi-major axis is given by Equation 3.4.

$$a = \frac{r_a + r_p}{2}, \tag{3.4}$$

where a $= 6971 \times 10^3$ meters. The orbital period is given by Equation 3.5.

$$P = \frac{2 \times \pi \times a^{3/2}}{\sqrt{\mu}} \tag{3.5}$$

Lastly, the orbital velocity of the satellite at any point at a distance r from the centre of Earth is given by Equation 3.6.

$$\mathrm{v} = \sqrt{\mu(2/\mathrm{r} - 1/\mathrm{a})} \tag{3.6}$$

Where $\mu \approx 3.9 \times 10^{14}$ m^3/s^2 is the gravitational constant. The assumptions made in this analysis are: spherical Earth, negligible relativistic effects and ignoring the Earth's nutation and precession due to its oblateness. With an orbital period of 98 minutes, about 14 orbits are made in one day. The satellite elevation angle relative to the receiver on the ground is calculated. Then the ground trace of the orbits are plotted in the azimuth-elevation plane, local horizontal plane and orthogonal projection. This is done for 3 receiver locations: SANAE IV in Antarctica, SANSA in Hermanus and Grintek in Pretoria. For each of these receiver locations, the orbits with inclination of 97.8° and 65° are considered. The part of the satellite orbit during which the satellite is visible from a given location is known as a satellite pass. Refraction caused by the ionosphere is not taken into account during the orbit propagation, but it is calculated for a specific location by means of ray tracing.

3.2   Orbit analysis results and discussion

3.2.1   Orbit analysis centred at SANAE IV in Antarctica.

Figure 3.1 shows that all satellite orbits traverse the radar field of view at an inclination of 97.8° in (a) but none of the satellite orbits traverse the radar at an inclination of 65° in (b). This shows that if the satellite is an orbit with inclination of 65° or less, will not be visible within the field of view of the SuperDARN radar at SANAE IV. Here the satellite coordinates were converted from the geographical coordinate system to the East-North-Up coordinate system.

In Figures 3.1 (c) and (d) the hemisphere projection was plotted with the zenith angle as the scale and the radial distance expressed in terms of the zenith angle. The zenith angle is the angle relative to the vertical line or zenith at the receiver. The centre of the plot corresponds to a satellite location directly above the receiver, and the edge of the plot corresponds to a satellite location on the horizon (elevation=0). Figure 3.1 (c) shows that there are 13 visible satellite passes out of 14 orbits at an inclination of 97.8°. Figure 3.1 (d) shows that there are 7 visible satellite passes out of 14 orbits at an inclination of 65°.

In Figure 3.2, the elevation range $(0° - 30°)$ and azimuth range $(156° - 210°)$ of the HF radar at SANAE IV has been superimposed onto the azimuth elevation plot (see red shaded area). This shows there are satellite passes which intersect the radar's field of view in terms of azimuth and elevation. It is clear from Figure 3.2 (a) that a number of satellite passes at

Plot for CubeSat orbits in orthogonal projection centred on SANAE IV

(a)

Plot for CubeSat orbits in orthogonal projection centred on SANAE IV

(b)

Hemisphere projection at inclination of 97.8° observed from SANAE IV

(c)

Hemisphere projection at inclination of 65° observed from SANAE IV

(d)
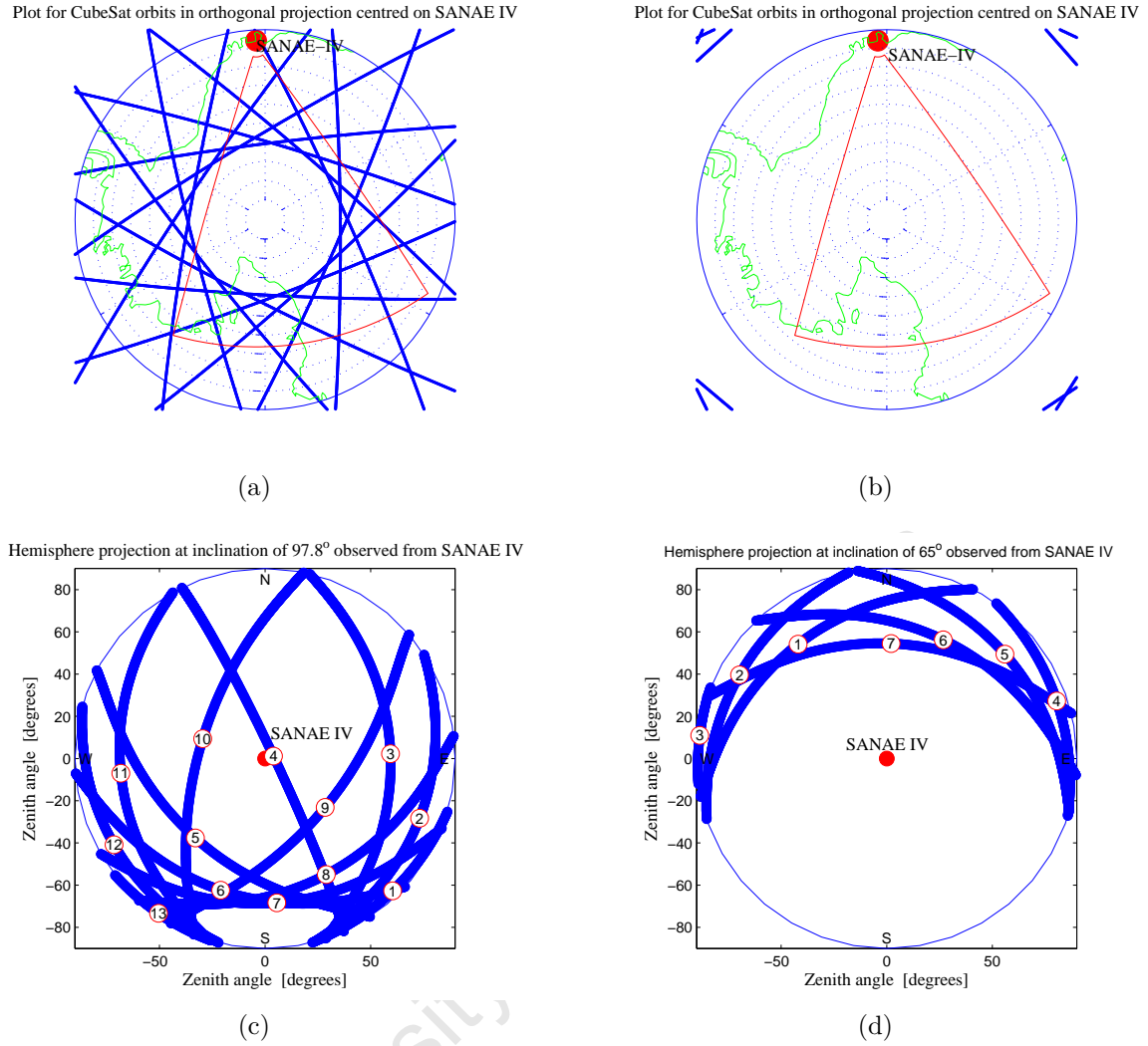
Figure 3.1: Orthogonal projection of the visible satellite passes out of 14 orbits for inclination equal to 97.8° in (a) and 65° in (b) centred at SANAE IV. Green and red borders mark the geographic map of Antarctica and ground trace of the radar coverage respectively. Figures (c) and (d) show projection of the visible satellite passes out of 14 orbits on the Earth's hemisphere for inclination angles of 97.8° and 65° respectively.

an inclination of 97.8° intersect the radar's azimuth and elevation range. However, there are no satellite passes at an inclination of 65° in 3.2 that intersect this region (Figure 3.2 (b)).

To view the physical visibility of the satellite, its orbits are traced in the local horizontal plane as shown in Figure 3.3. From Figure 3.3 (a), which shows the ground projection of the visible satellite passes out of 14 orbits in the local horizontal plane at an inclination of 97.8°, it is clear that some of the satellite passes will be seen by the radar, since its field of view is south of SANAE IV. However, in Figure 3.3 (b), which shows the ground projection of the visible passes out of 14 orbits in the local horizontal plane at an inclination of 65°, these satellite passes will not be seen by the radar. This is because, even if the satellite passes
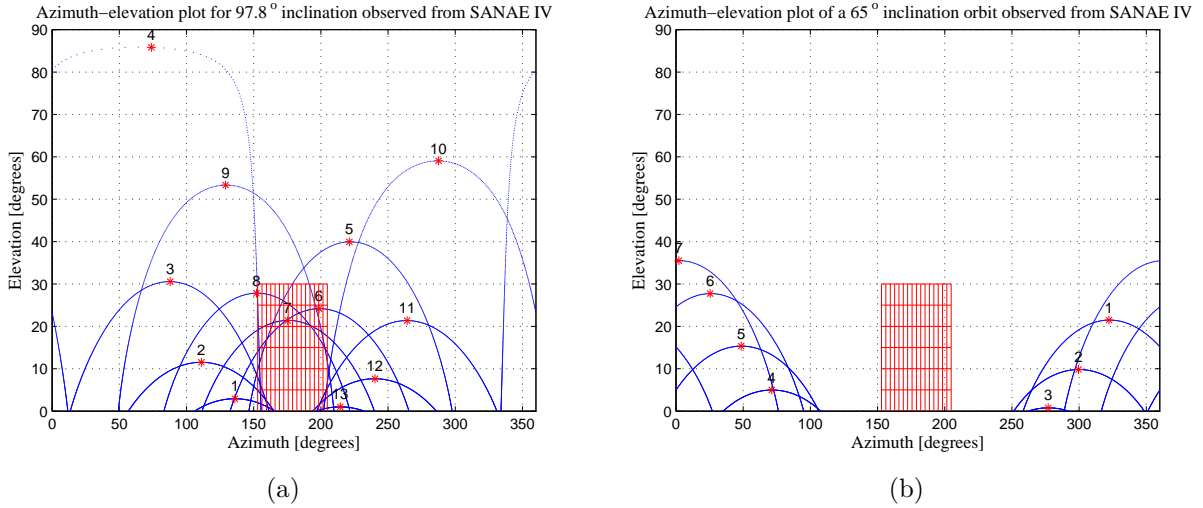
Figure 3.2: Projection of the visible passes out of 14 orbits in the azimuth-elevation plane at an inclination of 97.8° in (a) and 65° in (b), centred at SANAE IV. The area shaded red is the azimuth-elevation coverage of the radar

are as close to SANAE IV to the north in (b) as to the south in (a), the radar does not see north of SANAE IV.
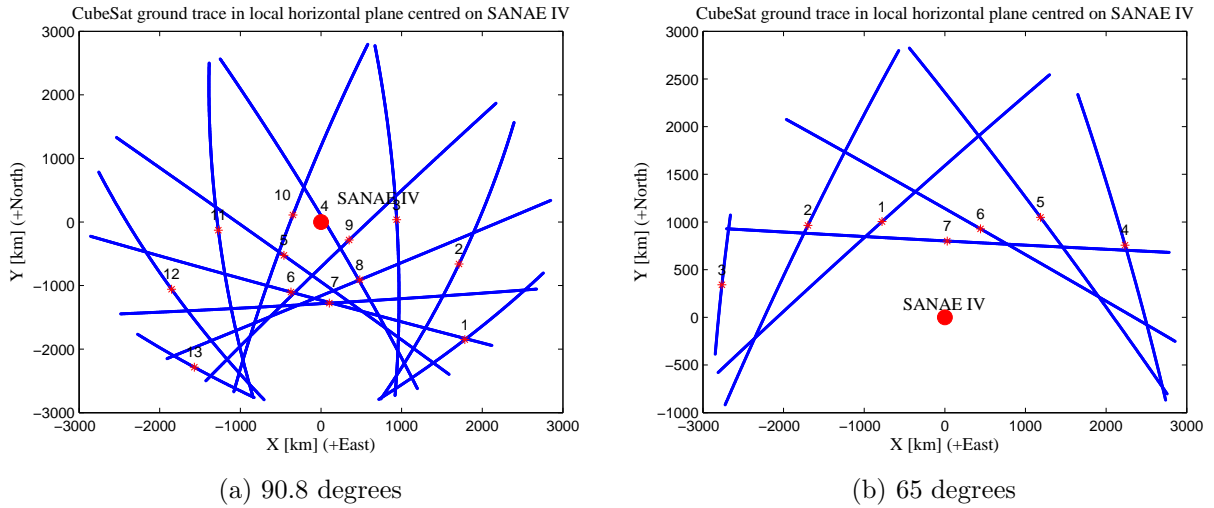
Figure 3.3: Ground projection of the satellite visible passes out of 14 orbits in the local horizontal plane at an inclination of 97.8° in (a) and 65° in (b), centred at SANAE IV.

Figure 3.4 (a) shows that, even though the satellite has a maximum elevation of about 86° in the 4th satellite pass at an inclination of 97.8°, part of each of the 13 passes falls within the radar's elevation range of 0°-30°. Figure 3.4 (b) shows that even though the satellite has a maximum elevation of about 35° in the 7th satellite pass at an inclination of 65°, part of each of the 7 visible passes falls within the radar's elevation range. In Figure 3.4 (c) there

31

are visible satellite passes with azimuth values that are within the radar's range (156°-210°), but none of the visible satellite passes in Figure 3.4 (d) are within this range.
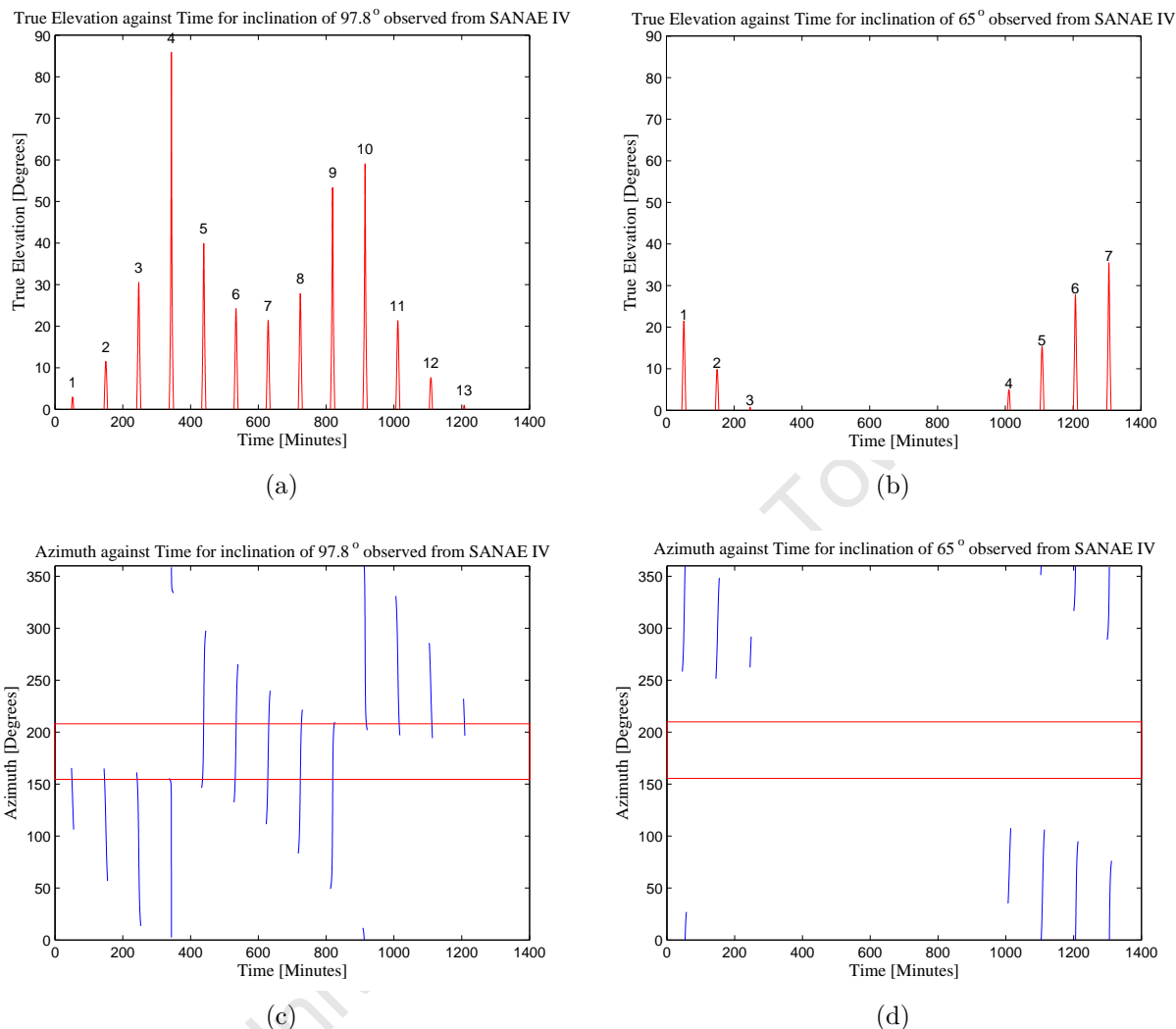
Figure 3.4: Plots of true elevation against time for the visible satellite passes out of 14 orbits at an inclination of 97.8° in (a) and 65° in (b) and azimuth against time for the visible satellite passes out of 14 orbits at an inclination of 97.8° in (c) and 65° in (d), centred at SANAE IV. The red border in (c) and (d) shows the azimuth range of the radar.

Considering the elevation angles for the 13 visible satellite passes out of 14 orbits over SANAE IV at an inclination of 97.8° (Figure 3.4 (a)), a ray trace was done to determine the expected refraction for each of these passes. Figure 3.5 shows the amount of refraction expected for the best and worst propagation conditions in midwinter on 1 June 2011 at 23:00 UT and midsummer on 1 January 2011 at 12:00 UT, respectively, as determined by means of the spherical Earth top-to-bottom multilayer model. In Figure 3.5 the satellite elevation angles from the visible passes were concatenated, thereby eliminating the time gaps.

The satellite elevation angles, which are now true elevation angles (e_T) at the inclination of 97.8°, were used to calculate the apparent elevation angles (e_A) from the spherical Earth top-to-bottom multilayer model for the worst (midsummer) and best (midwinter) propagation conditions. The true and apparent elevation angles were then plotted against the time index. The difference between e_T and e_A gives the expected refraction. In Figure 3.5 (a) the maximum refraction obtained in summer was about 16.4° compared to 16.1° obtained with the same model (Model 3b). This is illustrated in Figure 4.17 (a) in Chapter 4. According to Figure 3.5 (b) the maximum refraction obtained in winter was about 0.6° and it compares to 0.7° obtained with the same model (see Figure 4.17 (b)).
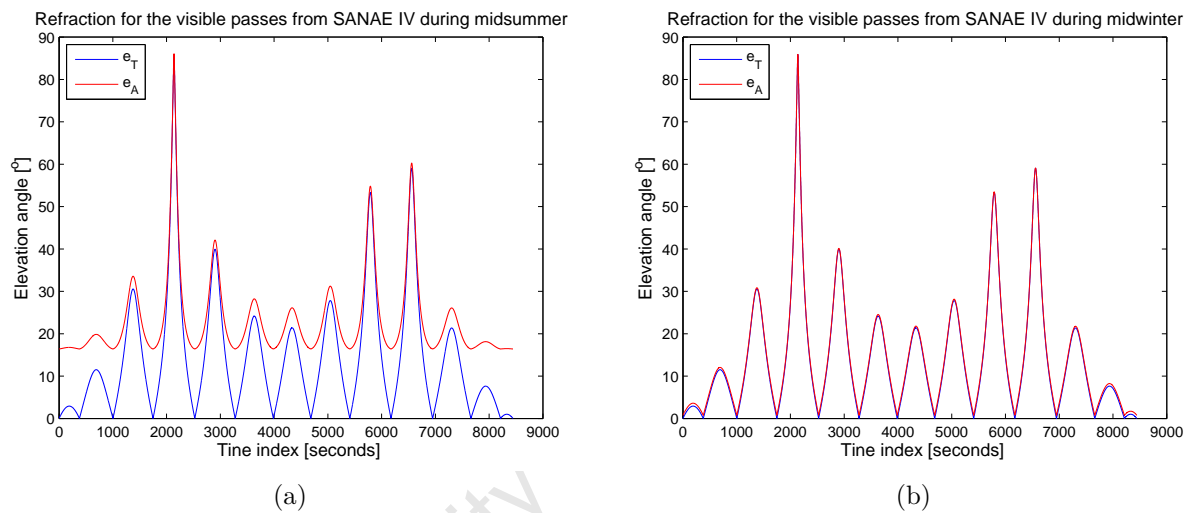

(a)   (b)

Figure 3.5: Comparison of satellite elevation angle (e_T) and apparent elevation angle (e_A) during midsummer (a) and midwinter (b) for the visible satellite passes at an inclination of 97.8° over SANAE IV

3.2.2   Orbit analysis centred at SANSA in Hermanus.

For the orbit analysis centred at SANSA in Hermanus, where the proposed DF instrument is to be built, the satellite was propagated for 14 orbits at an inclination angles of 97.8° and 65°. In Figure 3.6 (a) 4 satellite passes out of 14 orbits are visible along the Earth's hemisphere at the inclination of 97.8°, whereas in Figure 3.6 (b), 6 satellite passes out of 14 orbits are visible along the Earth's hemisphere at the inclination of 65°. This indicates that the satellite will be visible from SANSA at both the selected inclination angles.

(a)   (b)
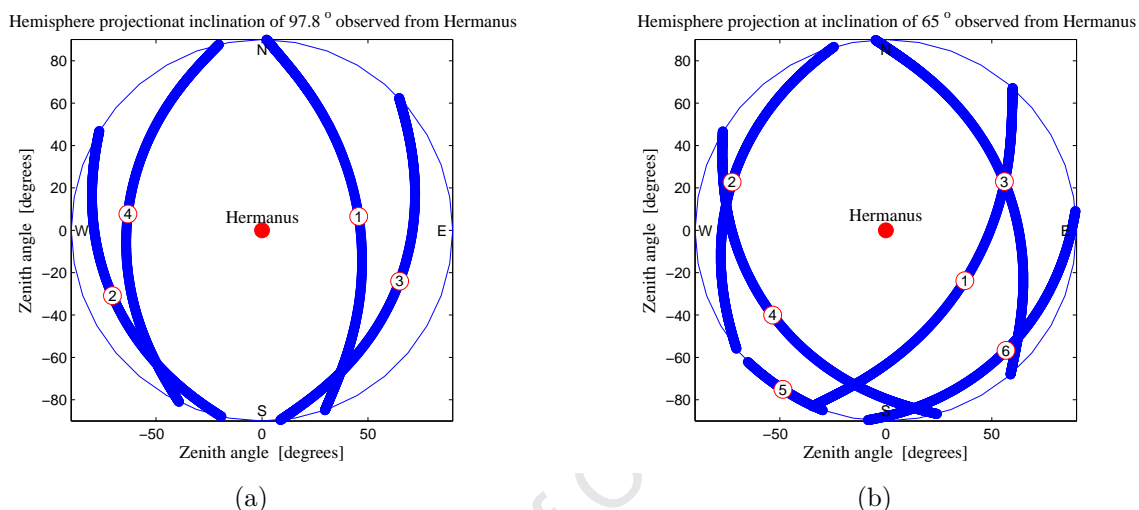
Figure 3.6: Projection of the 4 visible passes out of the 14 orbits on the Earth's hemisphere at inclination angles of 97.8° in (a) and the 6 visible passes out of 14 orbits at an inclination of 65° in (b) centred at SANSA in Hermanus.

For observation of the satellite from Hermanus, an azimuth range from horizon (0°) to horizon (360°) was considered and the corresponding satellite elevation angles were calculated and plotted. According to Figure 3.7, there are 4 visible satellite passes per day over Hermanus at an inclination angle of 97.8° in the elevation range from 0° to 44°, and 6 visible satellite passes per day at an inclination angle of 65° in the elevation range from 0° to 46°. The elevation and azimuth angles for the visible satellite passes are each plotted against time in Figure 3.8. For the visible passes in Figures 3.8 (a) and (b), the satellite elevation angles were concatenated to remove the time gaps.

Taking the satellite or true elevation angles (e_T) at an inclination of 97.8° as in Figure 3.8 (a), ray tracing was done to calculate the apparent elevation angles (e_A) and hence the expected refraction (e_A-e_T) for each pass over Hermanus. The model used for ray tracing was the spherical Earth top-to-bottom multilayer model, for both the best (midwinter) and worst (midsummer) conditions for trans-ionospheric propagation. In Figure 3.9 (a) the maximum refraction measured in summer was about 18.6° which is in the range of the 17° calculated

(a)   (b)
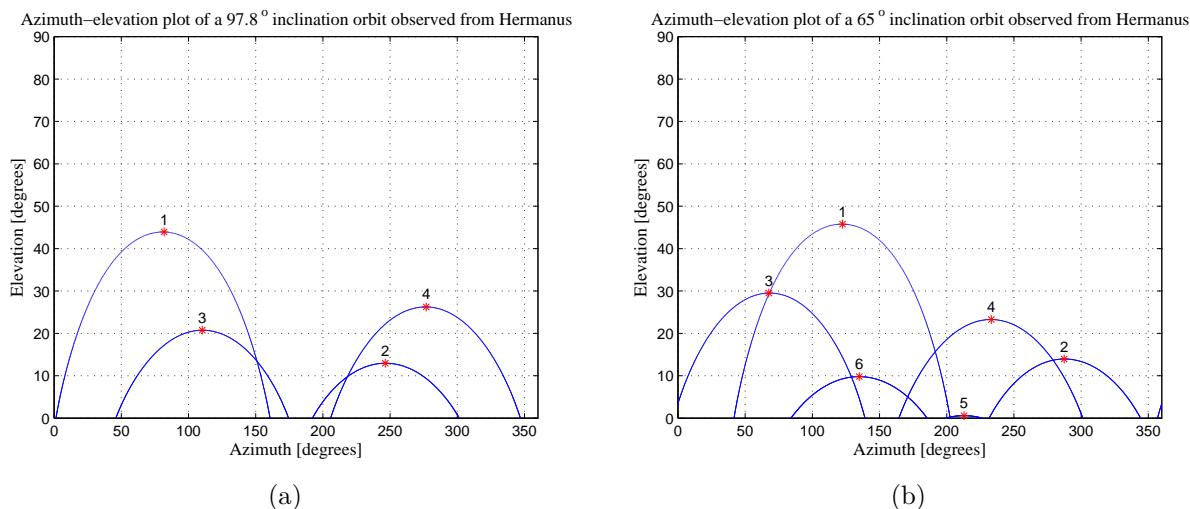
Figure 3.7: Projection of the 4 visible satellite passes out of 14 orbits in the azimuth-elevation plane at an inclination of 97.8° in (a) and the 6 visible passes per day at an inclination of 65° in (b), centred at SANSA in Hermanus.

by means of the spherical Earth top-to-down multilayer ray tracing model over Hermanus. The maximum refraction measured in winter was about 1.1° and it compares to 1° calculated by using a similar ray tracing model (Model 3b) over SANSA in Hermanus.

To see the satellite passes in the local horizontal plane over SANSA, the coordinates of the satellite's position are converted to a Cartesian coordinate system and plotted (see Figure 3.10). From this figure it is clear that there are 4 visible satellite passes per day at an inclination of 97.8° and 6 visible satellite passes per day at the inclination of 65° over SANSA.
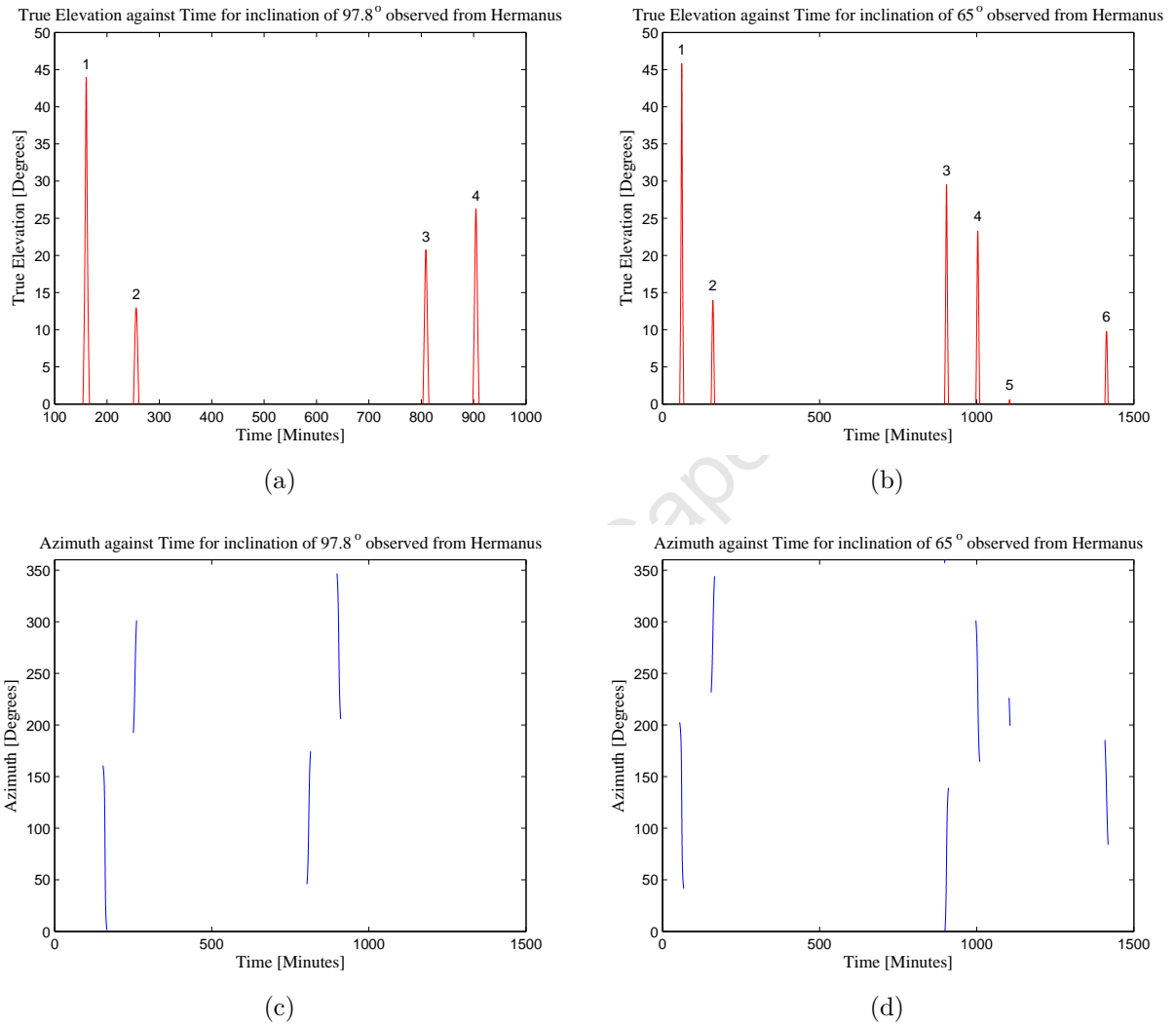
Figure 3.8: Plots of true elevation against time for the visible satellite passes out of 14 orbits at inclinations of 97.8° in (a) and 65° in (b) and azimuth against time for the visible satellite passes out of 14 orbits at an inclination of 97.8° in (c) and 65° in (d), centred at SANSA in Hermanus.
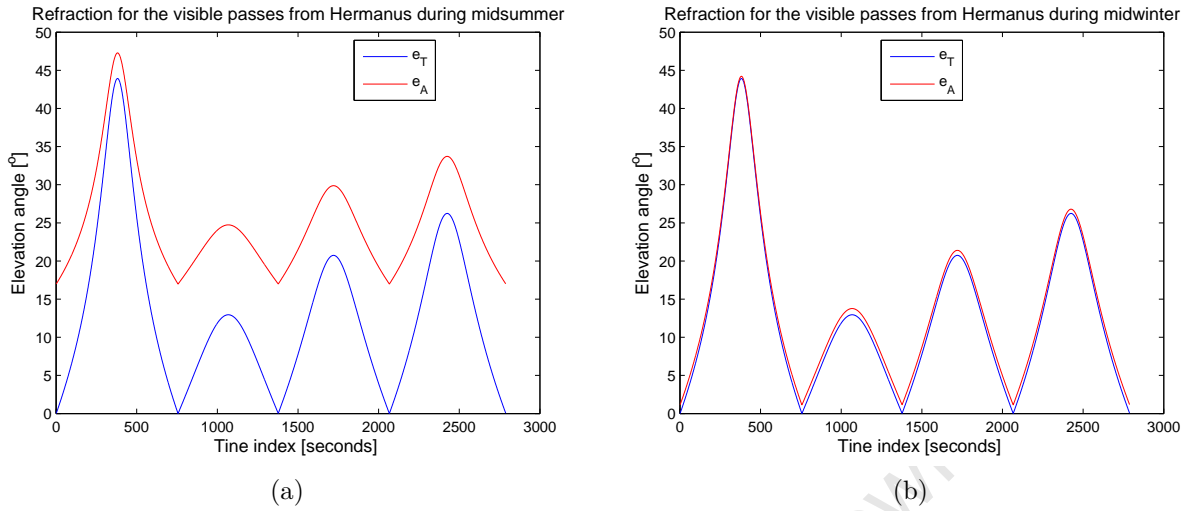
Figure 3.9: Comparison of satellite elevation angle (e_T) and apparent elevation angle (e_A) during midsummer on 1 January 2011 at 12:00 UT (a) and midwinter on 1 June 2011 at 23:00 UT (b) for the visible satellite passes at an inclination of 97.8° over SANSA in Hermanus
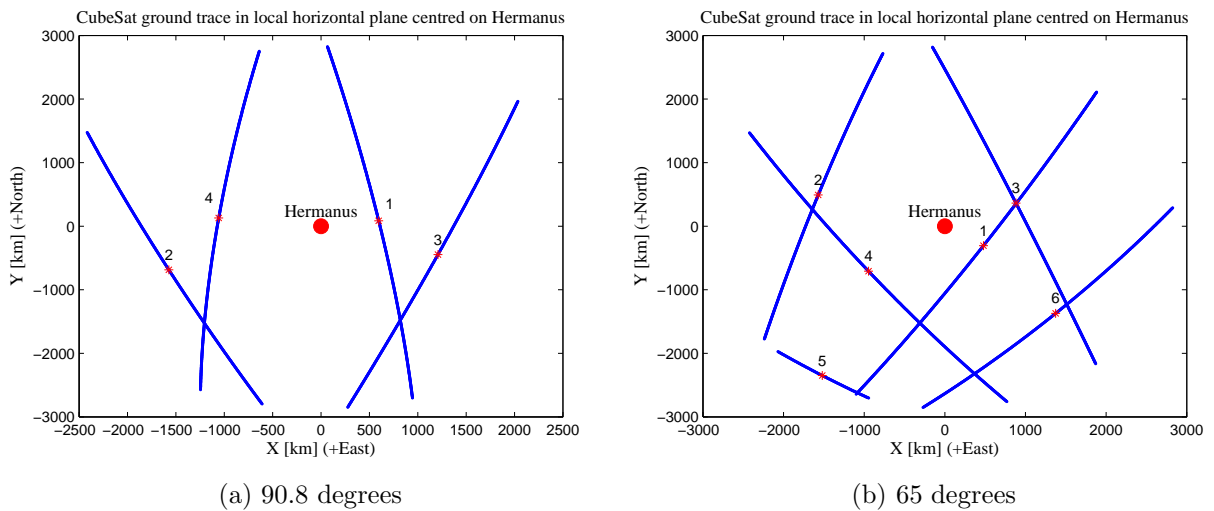
Figure 3.10: Ground projection of the 4 and 6 visible passes out of 14 orbits in the local horizontal plane at an inclination of 97.8° in (a) and 65° in (b) respectively, centred at SANSA in Hermanus.

3.2.3   Orbit analysis centred at Grintek in Pretoria.

For the orbit analysis centred at Grintek in Pretoria, the satellite's orbits were plotted along the Earth's hemisphere. In Figure 3.11 (a) and (b), 4 satellite passes out of 14 orbits for both inclination angles traverse the position of Grintek in Pretoria. This indicates that the satellite will be visible from Grintek for both the selected inclination angles.

An azimuth range from horizon (0°) to horizon (360°) was considered for the satellite passes over Grintek and the corresponding satellite elevation angles were calculated and plotted. Figure 3.12 shows 4 visible satellite passes per day over Grintek at inclination angles of both 97.8° and 65° within this range. The elevation and azimuth angles for the visible satellite passes are plotted against time in Figure 3.13. In Figures 3.13 (a) and (b), the satellite elevation angles for were concatenated to remove the time gaps. Figures 3.13 (a) and (b) show 4 satellite passes in the elevation range from 0° to 24° and 0° to 27° at an inclination of 97.8° and 65° respectively. The azimuth variation for the visible satellite passes out of the 14 orbits is shown in Figures 3.13 (c) and (d).

Using the satellite elevation angles obtained from Figure 3.13 (a) as true elevation (e_T), a ray trace was done to obtain the apparent elevation (e_A) angles and hence the amount of expected refraction during each visible pass over Grintek in Pretoria. The spherical Earth top-to-bottom multilayer ray tracing model was used for both the best (midwinter) and worst (midsummer) conditions for trans-ionospheric propagation. Figure 3.14 (a) indicates the maximum refraction in summer was about 20° which compares to the value of 20.4° obtained from ray tracing using the same model over Grintek. Figure 3.14 (b) indicates the

(a)   (b)
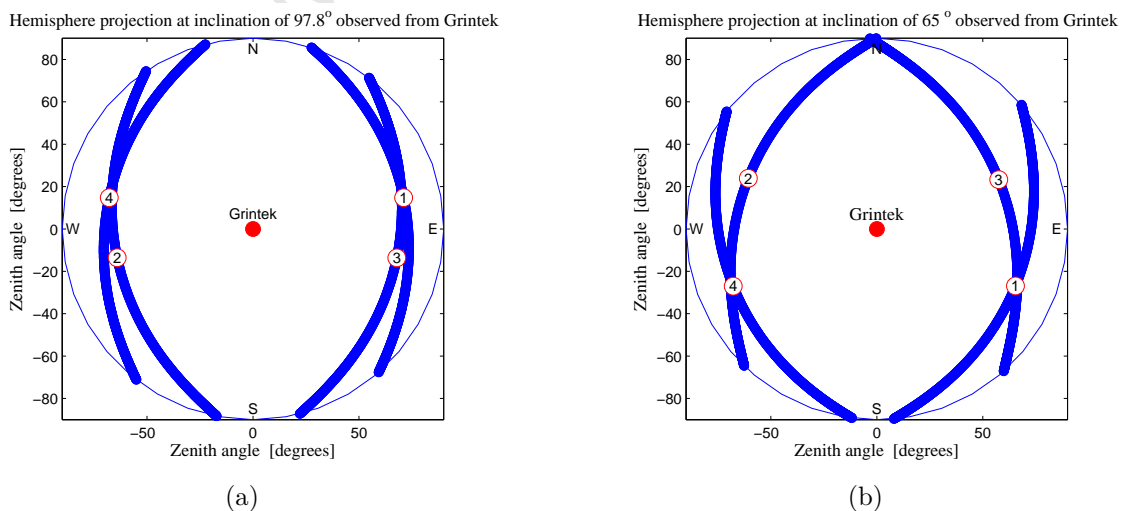
Figure 3.11: Projection of the 4 visible passes out of 14 orbits on the Earth's hemisphere at an inclination angle of 97.8° in (a) and 65° in (b) centred at Grintek in Pretoria.

(a)

(b)

Figure 3.12: Projection of the 4 visible satellite passes out of 14 orbits in the azimuth-elevation plane at an inclination of 97.8° in (a) and the 6 visible passes per day at an inclination of 65° in (b), centred at SANSA in Hermanus.

maximum refraction in winter was 1.8° and it compares to the value of 1.6° obtained from ray tracing using a similar model over Grintek.

To see the satellite passes in the local horizontal plane over Grintek, the coordinates of the satellite's position are converted to a Cartesian coordinate system and plotted as shown in Figure 3.15. This figure illustrates that there are 4 visible satellite passes over Grintek at inclination angles of both 97.8° and 65°.
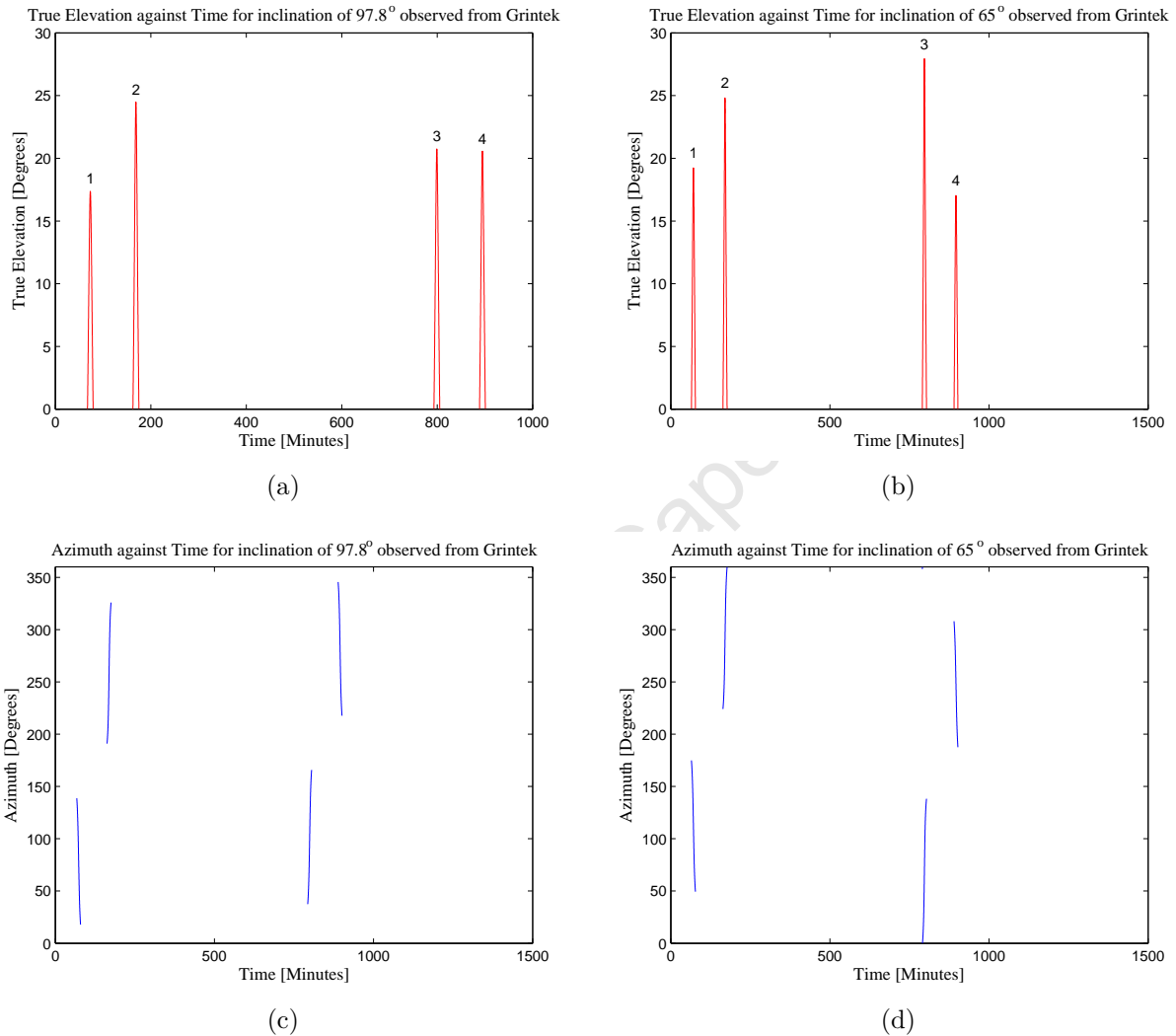
Figure 3.13: True elevation against time for the 4 visible satellite passes out of 14 orbits at an inclination angle of 97.8° in (a) and 65° in (b) and azimuth against time for the 4 visible satellite passes out of 14 orbits at an inclination of 97.8° in (c) and 65° in (d), centred at Grintek in Pretoria.

(a)

(b)
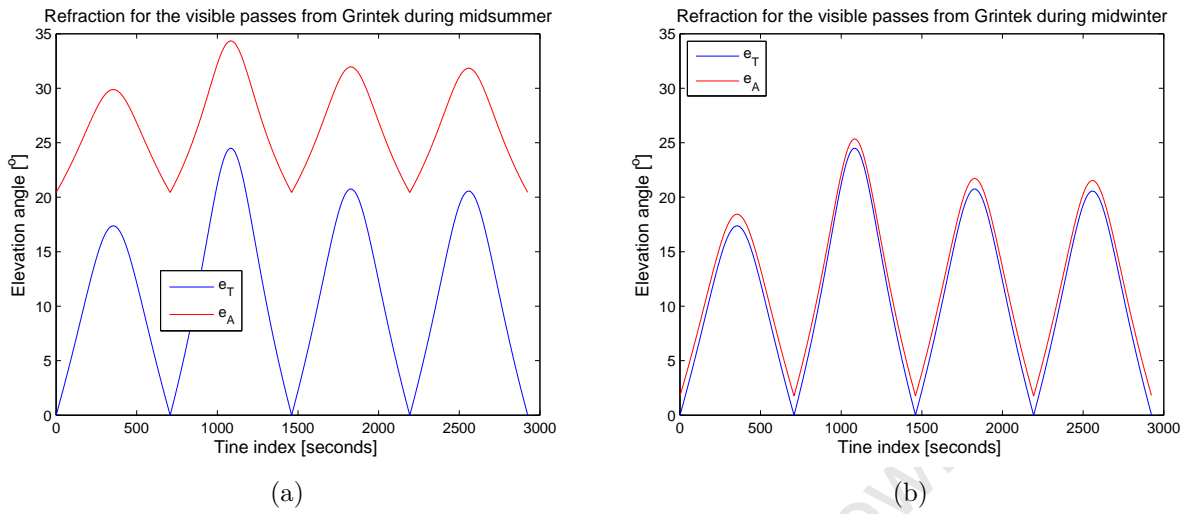
Figure 3.14: Comparison of satellite elevation angle (e_T) and apparent elevation angle (e_A) during midsummer on 1 January 2011 at 12:00 UT (a) and midwinter on 1 June 2011 at 23:00 UT (b) for the visible satellite passes at an inclination of 97.8° over Grintek in Pretoria
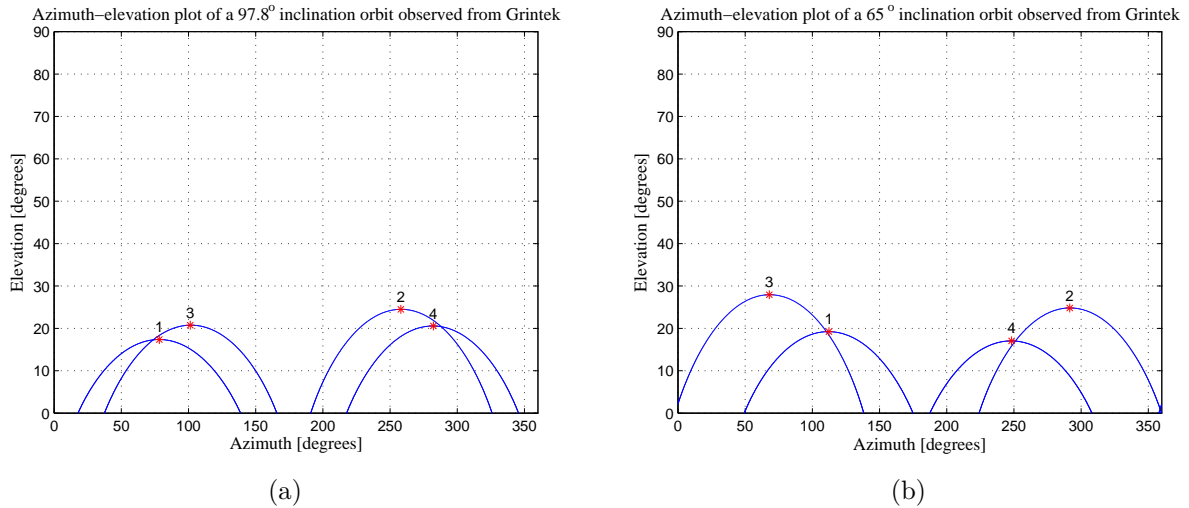

(a) 90.8 degrees

(b) 65 degrees
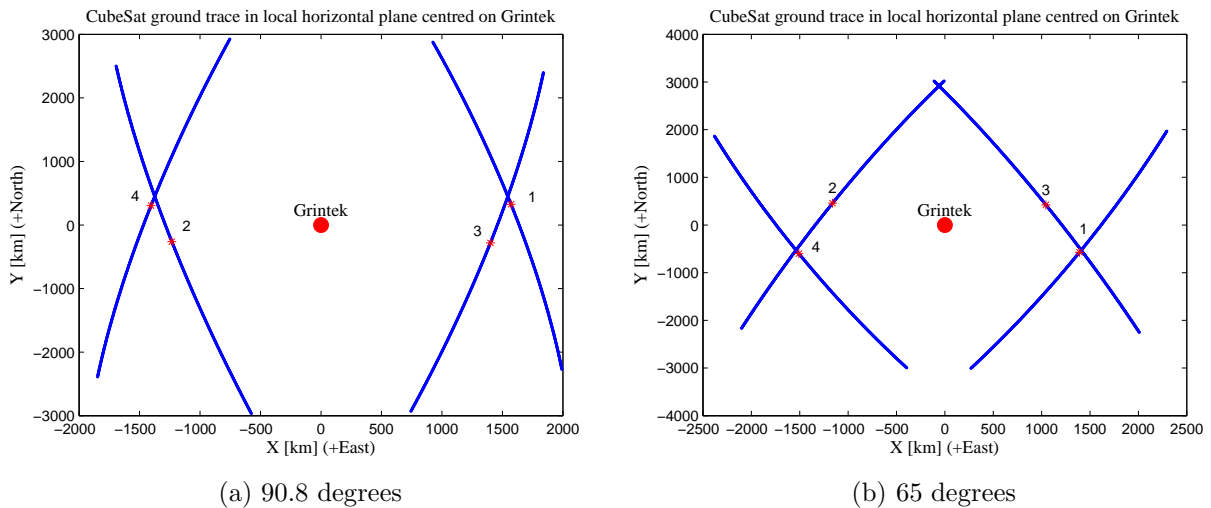
Figure 3.15: Ground projection of the 4 visible satellite passes out of 14 orbits in the local horizontal plane at an inclination of 97.8° in (a) and 65° in (b), centred at Grintek in Pretoria.

41

3.2.4 Summary of the orbit analysis results

For the CubeSat at an altitude of 600 km and inclination angles of 97.8° and 65°, a minimum of 0 passes and a maximum of 13 passes are expected to be seen from SANAE IV, SANSA in Hermanus and Grintek in Pretoria. The total time for each of these passes is added for 24 hours to give the daily satellite visibility for the two inclination angles of 97.8° and 65° at each of these locations as shown in Figure 3.16.

For the true elevation angles that correspond to the visible satellite passes within the range of the receiver, the maximum expected refraction as obtained by ray tracing ranged from 0° to 20°. Table 3.1 shows a summary of the maximum refraction obtained for the true elevation from the visible satellite passes per day at an inclination of 97.8° over SANAE IV, SANSA and Grintek, during winter and summer.

The results indicate that the best inclination at which the satellite signal would be received at these 3 locations is 97.8°. The propagation time with the least amount of refraction is midnight in winter. The similarity between the orbit analysis results for Hermanus and Pretoria can be attributed to their geographical proximity.

Table 3.1: Summary of the maximum refraction obtained for the visible satellite passes out of 14 orbits at an inclination of 97.8° over SANAE IV, SANSA and Grintek.

Maximum refraction		
	Summer	Winter
SANAE IV	16.4	0.6
SANSA	18.6	1.1
Grintek	20.0	1.8
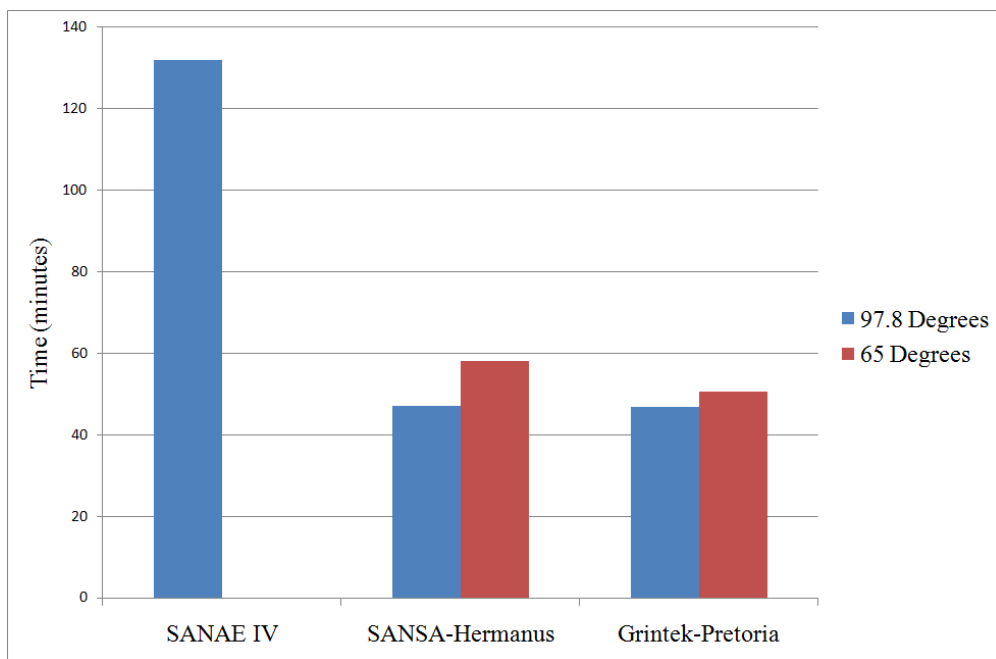
(a)

Figure 3.16: Summary of the duration of visibility of the satellite during a 24 hour period over SANAE IV, SANSA and Grintek.

Chapter 4

Ray tracing techniques

Ray tracing is a method of simulating the path taken and the effects experienced by waves or particles as they propagate from one point to another through a system with regions of varying propagation properties. HF communicators use ray tracing to precisely determine the paths of HF waves as they propagate through the ionosphere (Tomas, 2010). The process basically involves a step-by-step integration of differential equations that describe the propagation of these waves through dispersive and anisotropic media like the ionosphere (Budden, 1985). Unlike optical ray tracing, in which the refractive index is typically constant for a given medium, ray tracing through the ionosphere must account for the complexities of a spatially and temporally varying refractive index. Changes in the ionospheric electron density correspond to changes in the refractive index.

The fact that ray tracing can be performed for a variety of paths, e.g ground to ground, ground to satellite or satellite to ground, makes it an important tool in understanding near-space phenomena. Such phenomena include: observing aurorae, detecting backscatter from magnetic field-aligned plasma irregularities in the ionosphere, ionospheric dynamics such as gravity waves, mapping density irregularities in the ionosphere and global electron density distribution (Bennett *et al.*, 2004).

Two of the most common equations used for ray tracing are Fermat's principle, which calculates the ray path for minimum travel time, and Snell's law based on the law of refraction. Approximated models of trans-ionospheric ray tracing for satellite to ground and ground to satellite ray paths are described in the following section. In Models 1, 2 and 3, only the ray paths that reach the satellite altitude are plotted, the reflected rays are not of interest. However, in the Haselgrove ray tracing algorithm, the reflected rays are also plotted. For all the ray tracing results, both summer and winter conditions are evaluated. This is because during summer, the rays are subject to a significant amount of refraction which makes the conditions suitable for performing ionospheric physics while during winter, refraction is

minimal making conditions suitable for characterising the radar.

4.1   Model 1: Uniform electron density model

As a first approximation, the ionosphere is represented by a uniform planar electron density layer of density N_e, thickness B, and with altitude range h1 to h2. The values of these parameters are estimated from electron density profiles at the location of interest which can be obtained from an appropriate model such as the IRI, or from measurements from ionograms or from GPS tomography. To obtain the simplified model, the electron density is assumed to vary only with altitude and this means neglecting any azimuthal variation.

In this model, the thickness of the ionosphere is assumed to be twice the bottomside thickness parameter (B_0). The $B_0 = h_mF_2$ - $h_{0.24}$ parameter is by definition the height difference between the height at which the peak electron density occurs (hmF2) and the height where the electron density profile has dropped to 0.24 of the maximum electron density of the F_2-layer (Bilitza, 1998). The parameters h_mF_2 and $h_{0.24}$ can be obtained from any electron density profile. Total ionospheric thickness (T) $= 2 \times B_0$. The top height of the single ionospheric layer $h_2 = h_1 + T$. The electron density now is assumed to be the TEC divided by the thickness T as shown in Equation 4.1. The particular value of the mean electron density $(\overline{N_e})$ depends on the season and time of day chosen for the simulation.

$$\text{TEC} = \int\limits_{h_1}^{h_2} N_e(z)\,\mathrm{d}z = \overline{N_e}T \tag{4.1}$$

For this study, the electron density, ionospheric height and thickness parameters were derived from the IRI 2007 model and the uniform layer parameters are derived and plotted for 1 January 2011 at 12:00 UT and 1 June 2011 at 23:00 UT representing summer and winter extremes respectively. The geographical position of SANAE IV is 2.85°W, 71.67°S. The frequency of 14.099 MHz at which the satellite beacon will transmit its signal was used for the ray tracing. The electron density profile as obtained from the IRI 2007 model for midsummer and midwinter are shown in Figures 4.1 (a) and 4.1 (b).

Assuming that TEC, that is the total area under the electron density profile, is equal to the area under the red boundary in Figure 4.1, a single-layer ionospheric model was derived. The refractive index in the single-layer is uniform and is considered to be unity below and above the uniform layer. To perform ray tracing using this model, the correlation between the maximum electron density and refractive index was used, as shown in Equation 2.7. From the specified true elevation angles, the apparent elevation angles were calculated. The
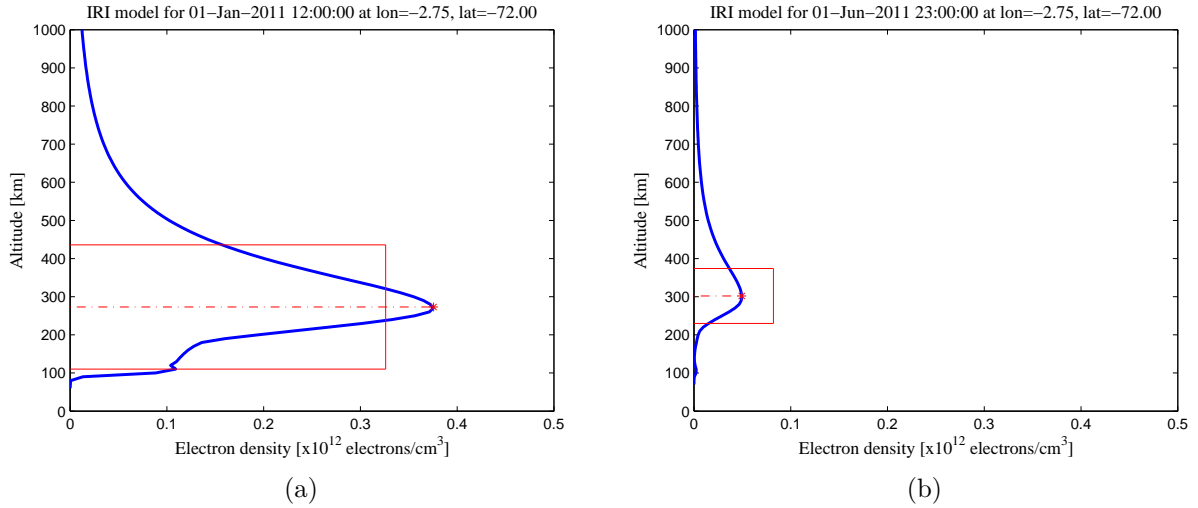
Figure 4.1: Uniform single-layer electron density profile derived from the IRI 2007 model over SANAE IV for midsummer on 1 January 2011 at 12:00 UT in (a) and midwinter on 1 June 2011 at 23:00 UT in (b)

difference between apparent and true elevation gives the approximate refraction.

4.1.1   Model 1a: Flat Earth uniform density model

In the flat Earth uniform density model, the Earth is assumed to be flat, that is the effects due to the Earth's curvature are assumed to be negligible at the altitude of a LEO. Figure 4.2 illustrates the parameters used in the flat Earth uniform density model.
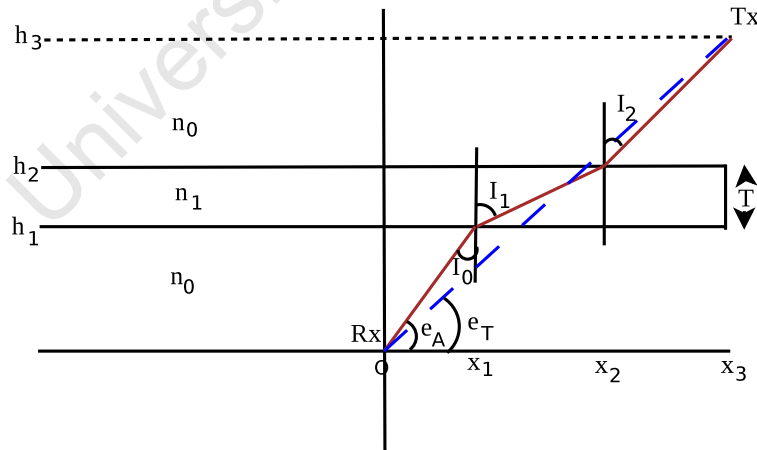
Figure 4.2: Geometry of the flat Earth single-layer, uniform electron density model.

For the flat Earth model, the equations describing the ray path starting from the receiver (Rx) and tracing upwards to the satellite (Tx), are as follows:
The horizontal distance of the ray path from the receiver to h_1, h_2, and the satellite height

h_3 are respectively given as:

$$x_1 = h_1 \tan(I_0) \qquad (4.2)$$

$$x_2 = x_1 + T \tan(I_1) \qquad (4.3)$$

$$x_3 = x_2 + (h_3 - h_2) \tan(I_0) \qquad (4.4)$$

where I_0 is the incident angle of the ground-to-satellite ray path at the point where the ray path enters the ionosphere. The incident angle is related to the apparent elevation angle E_A by:

$$I_0 = \frac{\pi}{2} - e_A \qquad (4.5)$$

The exit angle I_1 relative to the normal into the ionosphere can be derived from Snell's law.

$$n_0 \sin(I_0) = n_1 \sin(I_1) \qquad (4.6)$$

where $n_0 = 1$ is assumed in the neutral atmosphere above and below the ionosphere.
The true elevation angle e_T of the satellite as seen from the receiver can be derived from:

$$\tan(e_T) = \frac{h_3}{x_3} \qquad (4.7)$$

The minimum elevation angle for trans-ionospheric ray paths follows Snell's law at the point of entry into the ionosphere from the bottomside with $n_0 = 1$ and $I_0 = \frac{\pi}{2}$ as shown in Equation 4.7.

$$n_0 \sin(I_0) = n_0 \cos(e_A) = n_1 \sin(I_1) = n_1 \sin(\frac{\pi}{2}) \qquad (4.8)$$

Hence

$$I_0 = \sin^{-1}(n_1) \qquad (4.9)$$

and

$$e_A(\min) = \cos^{-1} n_1. \qquad (4.10)$$

The trans-ionospheric ray paths for the flat Earth, uniform electron density ionospheric model at the frequency f = 14.099 MHz were simulated and plotted for midsummer and midwinter to represent the worst and best case conditions for trans-ionospheric propagation, as shown in Figures 4.3 (a) and 4.3 (b) respectively. This ray tracing was done from the receiver back to the beacon transmitter on the satellite. According to Figure 4.3 all the ray paths shown reach the satellite altitude during both midsummer and midwinter. The ray paths below the minimum apparent elevation angle, as shown in Equation 4.9, do not reach the satellite.

The apparent and true elevation angles were calculated and the difference was plotted for

(a) Midsummer   (b) Midwinter

Figure 4.3: Trans-ionospheric ray paths for the flat Earth, single-layer uniform electron density ionosphere model at 14.099 MHz for midsummer on 1 January 2011 at 12:00 UT in (a) and midwinter on 1 June 2011 at 23:00 UT in (b)

both the summer and winter dates, as shown in Figures 4.4 (a) and 4.4 (b) respectively. Figure 4.4 (a) shows that true elevation angles below 30° are subject to refraction that increases with a decreasing true elevation angle, up to a maximum of 21° at the elevation angle of 0°. Figure 4.4 (b) shows that true elevation angles below 12° are subject to refraction that increases with a decreasing true elevation angle, up to a maximum of 10° at the elevation angle of 0°. This shows that more refraction at low true elevation angles occurs in summer than in winter.

(a) Midsummer   (b) Midwinter

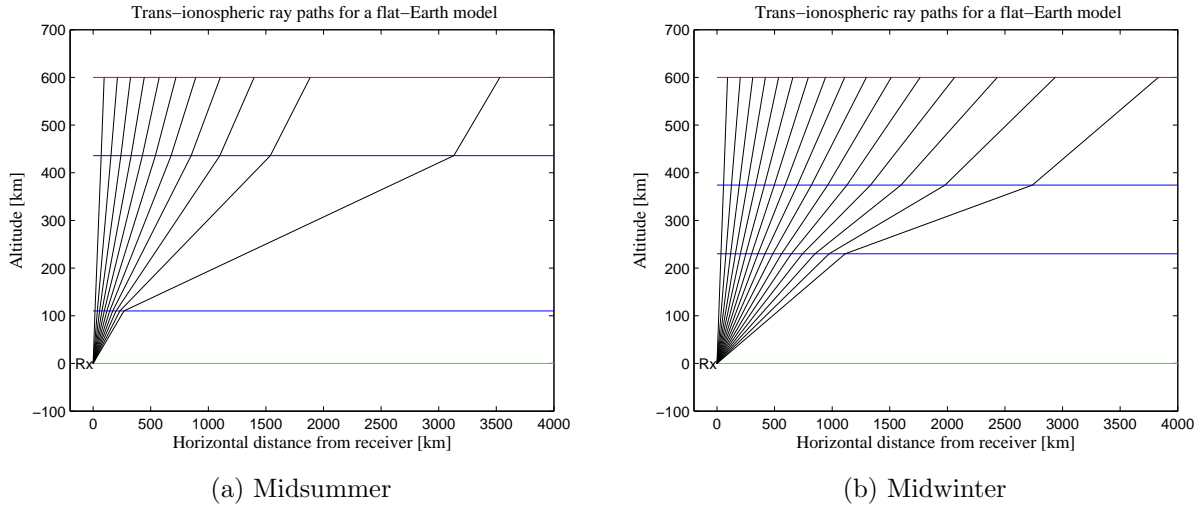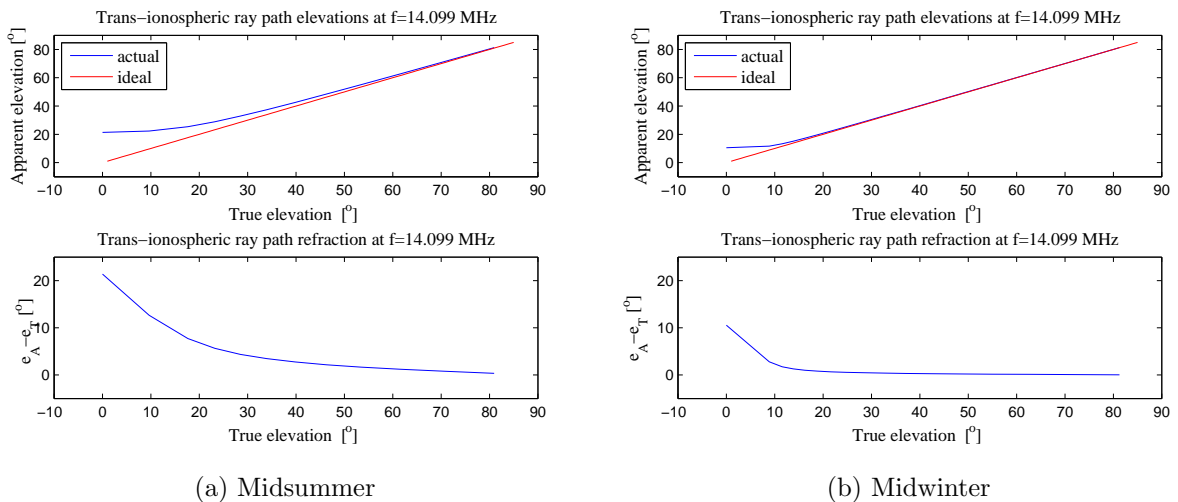Figure 4.4: True and apparent elevation angles (top panel) and their difference (bottom panel) for the flat Earth, single-layer uniform electron density ionosphere model at 14.099 MHz for midsummer on 1 January 2011 at 12:00 UT in (a) and midwinter on 1 June 2011 at 23:00 UT in (b)

4.1.2   Model 1b: Spherical Earth uniform density model

To evaluate whether the Earth's curvature actually has an effect on ray tracing through the ionosphere, the Earth is now assumed to have a spherical shape with a radius R_e approximately equal to 6371 km. Figure 4.5 illustrates a ray through a section of the spherical Earth with a uniform density single-layer model. For the spherical Earth approximation, the equations describing the ray paths are divided into 3 categories: when the satellite is above the horizon, on the horizon and below the horizon.
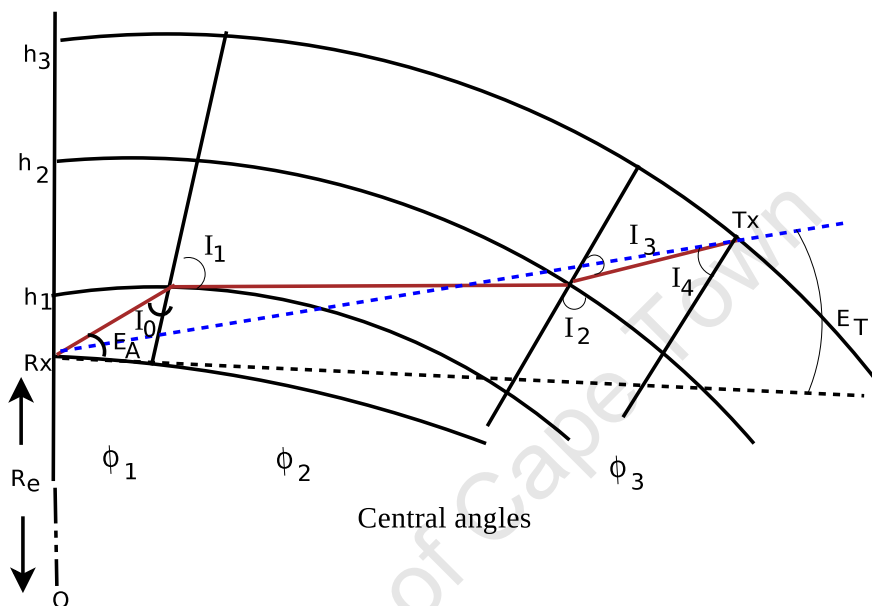
Figure 4.5: Geometry of the spherical Earth single-layer, uniform electron density model.

Satellite above the horizon

For the spherical Earth model, the equations describing the ray path to a satellite above the horizon, that is with true elevation angle greater than 0°, starting from the receiver and tracing upwards to the satellite, are as follows: The surface distances d_1, d_2 and d_3 traversed by the ray path corresponding to the vertical distances from the receiver to h_1, h_1 to h_2, and from h_2 to the satellite height h_3 are respectively related to the central angles ϕ_1, ϕ_2 and ϕ_3 by

$$d_1 = R_e \phi_1 \tag{4.11}$$

$$d_2 = R_e \phi_2 \tag{4.12}$$

$$d_3 = R_e \phi_3 \tag{4.13}$$

The total surface distance and the total central angle at the height of the satellite is given by:

$$S = d_1 + d_2 + d_3 \tag{4.14}$$

$$\phi_T = \phi_1 + \phi_2 + \phi_3 \tag{4.15}$$

The incident angle I_0 at the point where the ray path enters the ionosphere is related to the apparent elevation angle e_A by the sine rule:

$$\frac{\sin I_0}{R_e} = \frac{\sin(\frac{\pi}{2} + e_A)}{R_e + h_1} \tag{4.16}$$

As in the case of the flat Earth ionosphere model, the exit angle I_0 defined relative to the normal at the point where the ray path enters the ionosphere can be derived from Snell's law, Equation 2.6. The incident angle I_2 at the point where the ray path leaves the ionosphere can be derived from the sine rule applied to the triangle with central angle ϕ_2

$$\frac{\sin(I_2)}{R_e + h_1} = \frac{\sin(\frac{\pi}{2} + \frac{\pi}{2} - I_1)}{R_e + h_2} = \frac{\sin(I_1)}{R_e + h_2}. \tag{4.17}$$

The exit angle I_3 defined relative to the normal at the point where the ray path leaves the ionosphere can be derived from Snell's law

$$n_1 \sin(I_2) = n_0 \sin(I_3). \tag{4.18}$$

The angle I_4 between the ray path and the line from the satellite to the centre of the Earth can be derived from the sine rule applied to the triangle with central angle ϕ_3

$$\frac{\sin(I_4)}{R_e + h_2} = \frac{\sin(\frac{\pi}{2} + \frac{\pi}{2} - I_3)}{R_e + h_3} = \frac{\sin(I_3)}{R_e + h_3}. \tag{4.19}$$

The relationship between the central angles and the incident angles are

$$\phi_1 + \frac{\pi}{2} + e_A + I_0 = \pi, \tag{4.20}$$

$$\phi_2 + \frac{\pi}{2} + (\frac{\pi}{2} - I_1) + I_2 = \pi, \tag{4.21}$$

$$\phi_3 + \frac{\pi}{2} + (\frac{\pi}{2} - I_3) + I_4 = \pi. \tag{4.22}$$

In order to find the true elevation angle e_T from the receiver to the satellite, consider the triangle O-Rx-Tx where O is the centre of the Earth, Rx is the receiver and Tx is the transmitter. The direct distance D between Rx and Tx is related to the combined central

angle through the cosine rule:

$$D^2 = R_e^2 + (R_e + h_3)^2 - 2R_e(R_e + h_3)\cos(\phi_1 + \phi_2 + \phi_3). \tag{4.23}$$

The angle e_T can then be found from the application of the sine rule

$$\frac{\sin(\phi_1 + \phi_2 + \phi_3)}{D} = \frac{\sin\left(\frac{\pi}{2} + e_T\right)}{R_e + h_3}. \tag{4.24}$$

Thus

$$e_T = \cos^{-1}\left(\frac{R_e + h_3}{D}\sin(\phi_T)\right). \tag{4.25}$$

The theoretical the maximum value of the angle I_4 as shown in Equation 4.19, which corresponds to reflection from the topside of the ionosphere, can be obtained by considering a ray path from the satellite to the ionosphere. The maximum value of I_3 is then associated with the exit angle into the ionosphere I_2=90°. From Snell's law, this implies;

$$n_1 \sin I_2 = n_0 \sin I_3. \tag{4.26}$$

For $I_2 = \frac{\pi}{2}$, this implies $n_1 = \sin I_3$ and

$$I_4 = \sin^{-1}\left(\frac{R_e + h_2}{R_e + h_3}\right)n_1. \tag{4.27}$$

For conditions where I_4 is larger than the angle between the horizon and the line from the satellite to the centre of the Earth, which can be obtained from

$$\theta = \tan^{-1}\left(\frac{R_e}{R_e + h_3}\right), \tag{4.28}$$

it implies that the true elevation angle can be less that 0°. The angle I_2 is always less than I_1 since

$$\sin I_2 = \left(\frac{R_e + h_1}{R_e + h_2}\right)\sin I_1. \tag{4.29}$$

The implication for this condition is that reflection from the topside ($I_2 = \frac{\pi}{2}, n_1 = \sin I_3$) would occur at a true elevation angle lower than the angle where reflection from the bottomside occurs ($I_1 = \frac{\pi}{2}, n_1 = \sin I_0$). Thus the minimum value of the true elevation angle corresponds to the condition where reflection from the bottomside occurs for a ray path from the receiver to the satellite, that is; n_0=1 and $I_1 = \pi/2$. Thus $n_0 \sin I_0 = n_0 \cos e_A = n_1 \sin I_1 = n_1 \sin \pi/2$, hence $I_0 = \sin^{-1} n_1$.
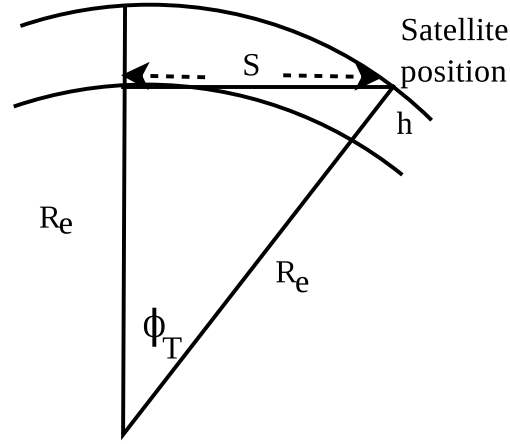
Figure 4.6: Illustration of the geometry of the satellite on the horizon ($e_T = 0$)

Satellite on the horizon

The corresponding equations are:

$$\cos(\phi_{Tc}) = \frac{R_e}{R_e + h_3} \tag{4.30}$$

$$D^2 = (R_e + h_3)^2 - R_e^2, \tag{4.31}$$

$$\phi_{Tc} = \frac{d_3}{R_e}. \tag{4.32}$$

where ϕ_{Tc} is the critical value of the central angle and d_3 is the distance along the surface, equal to 2664 km for $h_3 = 600$ km.

Satellite below the horizon

When the satellite is below the horizon ($e_T < 0°$), the distance D between the transmitter and the receiver is related to the combined central angle ϕ_T by the cosine rule.

$$D^2 = R_e^2 + (R_e + h_3)^2 - 2R_e(R_e + h_3)\cos(\phi_T) \tag{4.33}$$

The angle e_T can be obtained from the application of the sine rule.

$$\frac{\sin(\phi_T)}{D} = \frac{\sin\left(\frac{\pi}{2} - e_T\right)}{R_e + h_3} = \frac{\cos(e_T)}{R_e + h_3} \tag{4.34}$$

The true elevation angle (e_T) is then given by;

$$e_T = -\cos^{-1}\left(\frac{R_e + h_3}{D}\sin(\phi_T)\right) \tag{4.35}$$

This is similar to the case where the elevation angle $e_T > 0°$.

The trans-ionospheric ray paths for the spherical Earth, uniform electron density ionospheric model at the frequency f = 14.099 MHz were simulated and plotted. This was done for midsummer on 1 January 2011 at 12:00 UT and midwinter on 1 June 2011 at 23:00 UT, to represent the worst and best case conditions for trans-ionospheric propagation (Figures 4.7 (a) and 4.7 (b) respectively). Here the ray tracing was done from the receiver back to the beacon transmitter on the satellite.

(a) Midsummer   (b) Midwinter
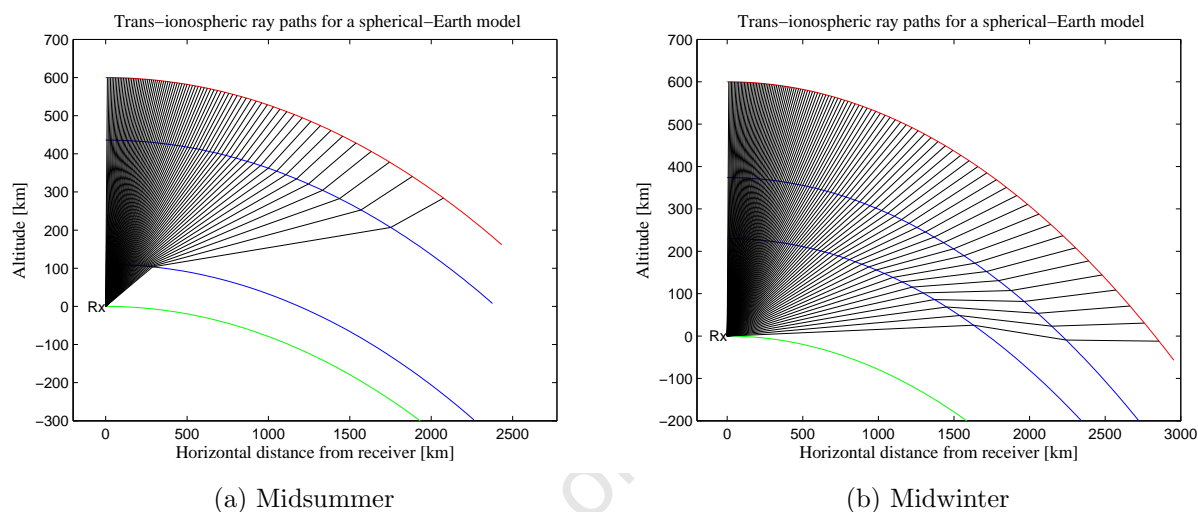
Figure 4.7: Trans-ionospheric ray paths at 14.099 MHz obtained by means of the spherical Earth model with uniform electron density single-layer ionosphere derived from the IRI profile for midsummer on 1 January 2011 at 12:00 UT in (a) and midwinter on 1 June 2011 at 23:00 UT in (b)

Figures 4.8 (a) and 4.8 (b) show the difference in true and apparent elevations for the spherical Earth, uniform electron density ionospheric model for both worst and best case conditions. At 14.099 MHz, the minimum apparent elevation angle for trans-ionospheric ray paths in the case of the spherical Earth model is 18.77° compared to true elevation of 0.89° in summer and 0° compared to a true elevation of 1.1° in winter. All the ray paths shown reach the satellite altitude with some rays reaching below the horizon in winter as illustrated by the negative elevation angle in Figure 4.8 (b). For spherical Earth approximation, it is possible for the true elevation to be greater than the apparent elevation ($e_T > e_A$) as illustrated in Figure 4.9.

(a) Midsummer   (b) Midwinter

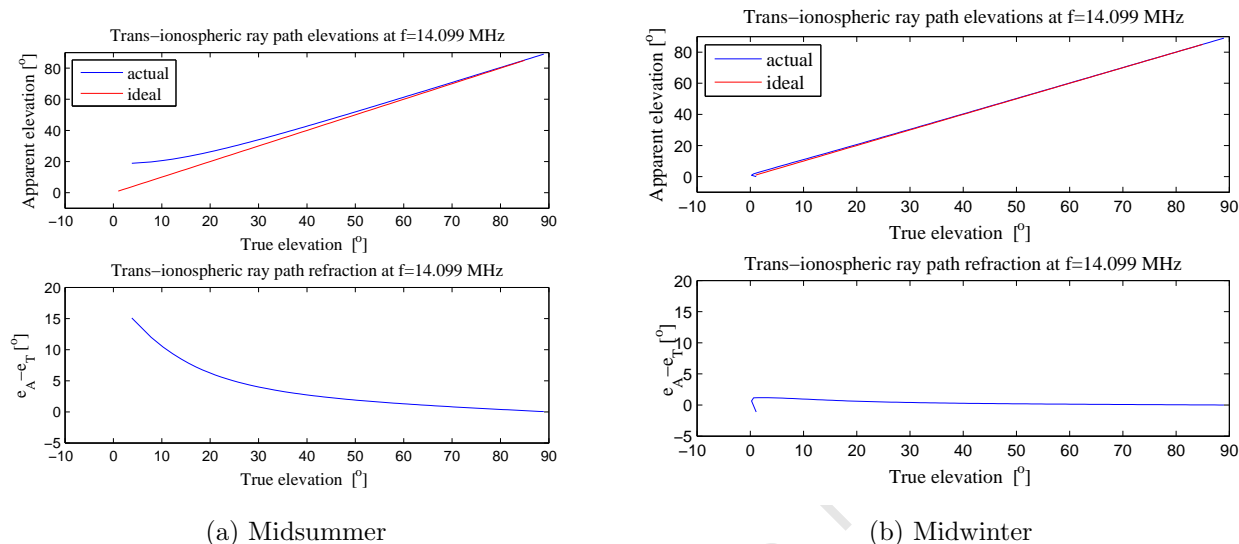Figure 4.8: True and apparent elevation angles (top panel) and their difference (bottom panel) for the spherical Earth, single-layer uniform electron density ionosphere model at 14.099 MHz for midsummer on 1 January 2011 at 12:00 UT in (a) and midwinter on 1 June 2011 at 23:00 UT in (b)
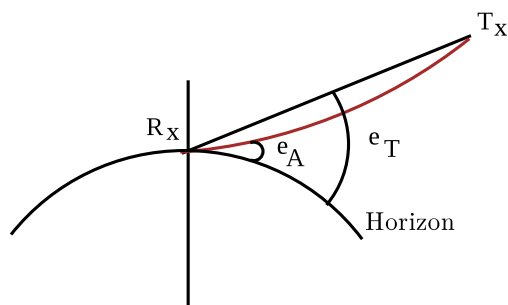
Figure 4.9: Illustration of the true elevation greater than apparent elevation ($e_T > e_T$)

4.2   Model 2: Multilayer model

In order to improve accuracy of the results obtained from Model 1, the number of layers in the ionosphere was increased to take into account the varying electron density and in turn the refractive index at every point where this value changes. Therefore, a new value for the refractive index was calculated at every layer as opposed to the average value used in the single-layer model. This is known as the multilayer model, as illustrated in Figure 4.10.
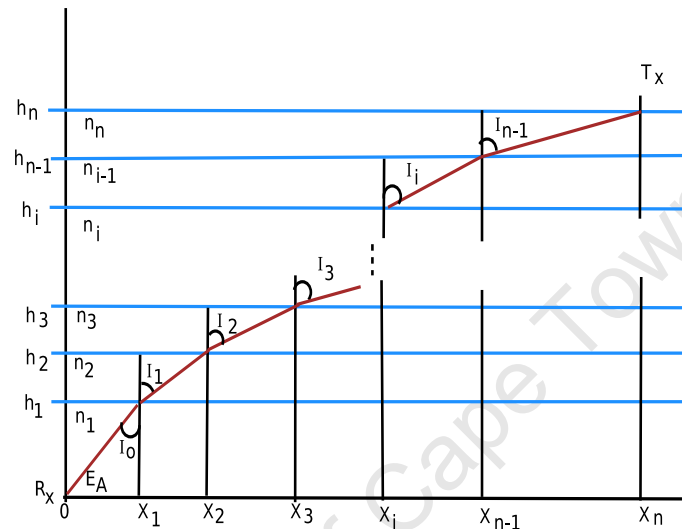
Figure 4.10: Diagram illustrating ray tracing for a flat Earth multilayer model

Figure 4.11 shows how the ionosphere is divided into several uniform density layers up to the satellite altitude (600 km) as derived from the IRI 2007 model over SANAE IV.
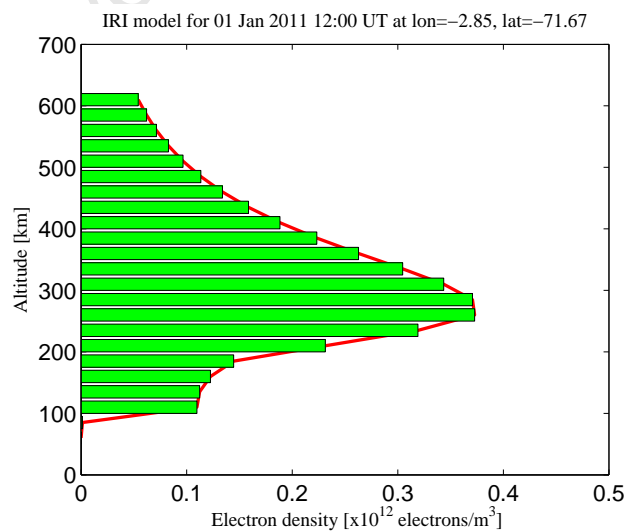
Figure 4.11: Illustration of the multilayer model where the electron density profile derived from the IRI model is divided into a number of layers of uniform electron density.

4.2.1   Model 2a: Flat Earth multilayer model

Figures 4.12 (a) and 4.12 (b) show the ray tracing results for the Flat Earth multilayer model, traced from the ground to the satellite at a frequency of 14.099 MHz. All the ray paths shown reach the satellite altitude and all propagate above the horizon.
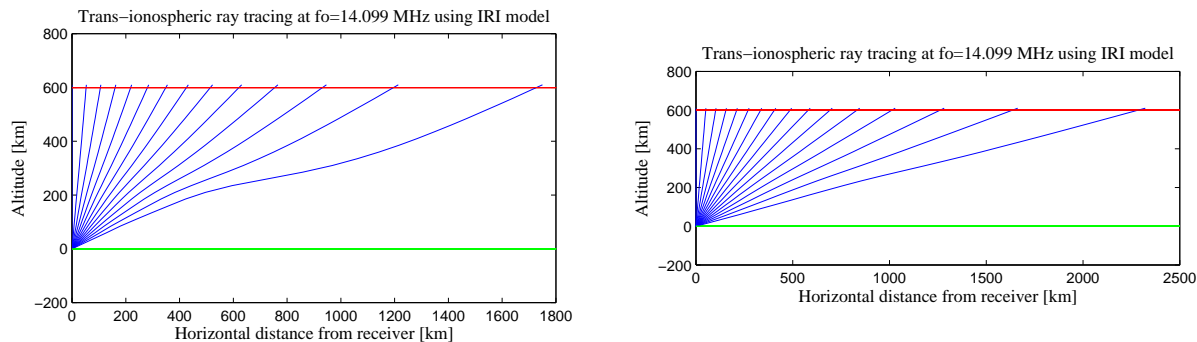
(a) Midsummer   (b) Midwinter

Figure 4.12: Trans-ionospheric ray paths for the flat Earth, multilayer model at 14.099 MHz for midsummer on 1 January 2011 at 12:00 UT in (a) and midwinter on 1 June 2011 at 23:00 UT in (b)

Figures 4.13 (a) and 4.13 (b) show the relationship between true and apparent elevation angles, the later derived from the flat Earth multilayer model for the midsummer and mid-winter dates. All the ray paths at elevation angles below 20° in summer and 6° in winter were completely reflected and were not plotted in Figure 4.12. The minimum apparent elevation angle in summer was 8° and it corresponds to the minimum satellite elevation angle of 8.76° as shown in Figure 4.13 (a). In winter, the minimum apparent elevation angle was 22.00° and it corresponds to the minimum satellite elevation angle of 16.82° as shown in Figure 4.13 (b).

(a) Midsummer   (b) Midwinter

Figure 4.13: Comparison of true and apparent elevation (top panel) and their difference (bottom panel) for the flat Earth, multilayer model at 14.099 MHz for midsummer on 1 January 2011 at 12:00 UT in (a) and midwinter on 1 June 2011 at 23:00 UT in (b).

4.2.2   Model 2b: Spherical Earth multilayer model

Figures 4.14 (a) and 4.14 (b) show the ray paths obtained by means of the spherical Earth multilayer model where the ray paths were traced from the ground to the satellite at a frequency of 14.099 MHz for both midsummer and midwinter, respectively. For both seasons, the ray paths shown reach the satellite altitude (600 km).

(a) Midsummer   (b) Midwinter

Figure 4.14: Trans-ionospheric ray paths for the spherical Earth multilayer model at 14.099 MHz for midsummer on 1 January 2011 at 12:00 UT in (a) and midwinter on 1 June 2011 at 23:00 UT in (b).

Figures 4.15 (a) and 4.15 (b) show the relationship between true and apparent elevation angles, the later obtained from the spherical Earth multilayer model, for both midsummer and midwinter. Figures 4.15 (a) and (b) show that all the rays below the true elevation angle of 8° in summer and 0° in winter are reflected. Below 40° in summer, the rays are refracted, and this increases with decreasing true elevation angle. The maximum refraction in summer is 10.00° and it compares to the minimum apparent elevation angle of 16.00°. Maximum refraction in winter is 0.36° and it compares to the minimum apparent elevation angle of 0.00°. There is minimal refraction of the rays during winter.

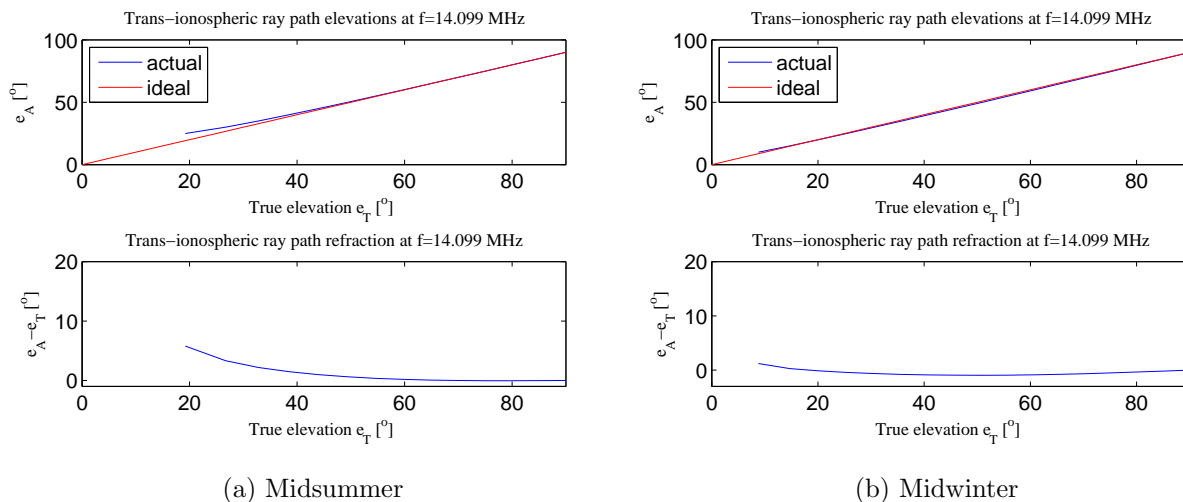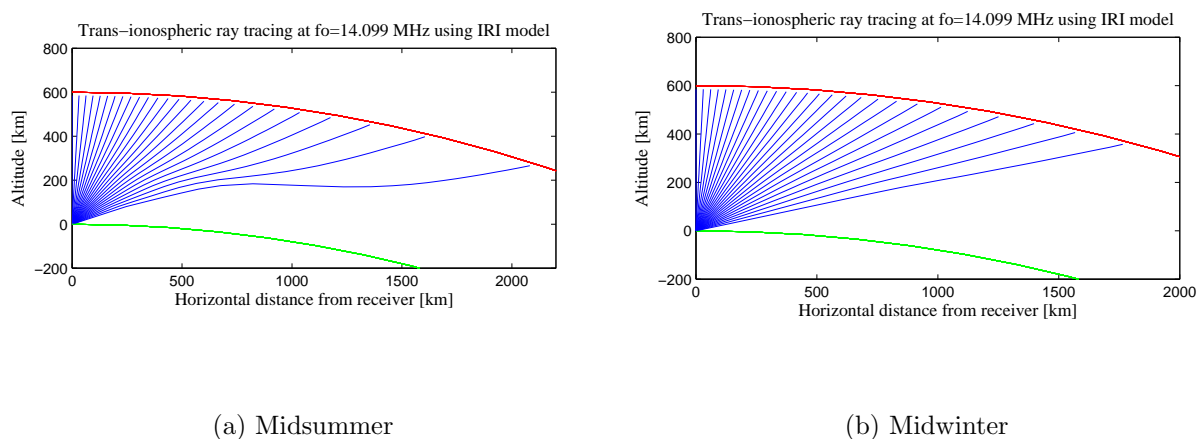(a) Midsummer   (b) Midwinter

Figure 4.15: Comparison of true and apparent elevation (top panel) and their difference (bottom panel) for the spherical Earth multilayer model at 14.099 MHz for midsummer on 1 January 2011 at 12:00 UT in (a) and midwinter on 1 June 2011 at 23:00 UT in (b)

4.3   Model 3: Top-to-bottom

To determine whether ray tracing from receiver to transmitter gives relatively accurate results, another path was traced from the beacon transmitter on the satellite to the ground receiver. This method is called 'top-to-bottom' ray tracing.

4.3.1   Model 3a: Flat Earth top-to-bottom ray tracing

The results of the top-to-bottom ray tracing for the flat Earth multilayer model for the worst and the best propagation conditions, are shown in Figures 4.16 (a) to 4.16 (b). All the ray paths shown reach the ground from the satellite. A comparison of the true and apparent elevation angles for the flat Earth multilayer top-to-bottom model at 14.099 MHz is shown in Figures 4.17 (a) and 4.17 (b). There is minimal refraction for propagation in winter as

(a) Midsummer   (b) Midwinter

Figure 4.16: Trans-ionospheric ray paths for the flat Earth multilayer top-to-bottom model at 14.099 MHz for midsummer on 1 January 2011 at 12:00 UT in (a) and midwinter on 1 June 2011 at 23:00 UT in (b)

shown by Figure 4.17 (b). There is refraction up to a maximum of 8° for elevation angles less that 40°. Below 18° there is complete reflection from the topside ionosphere.
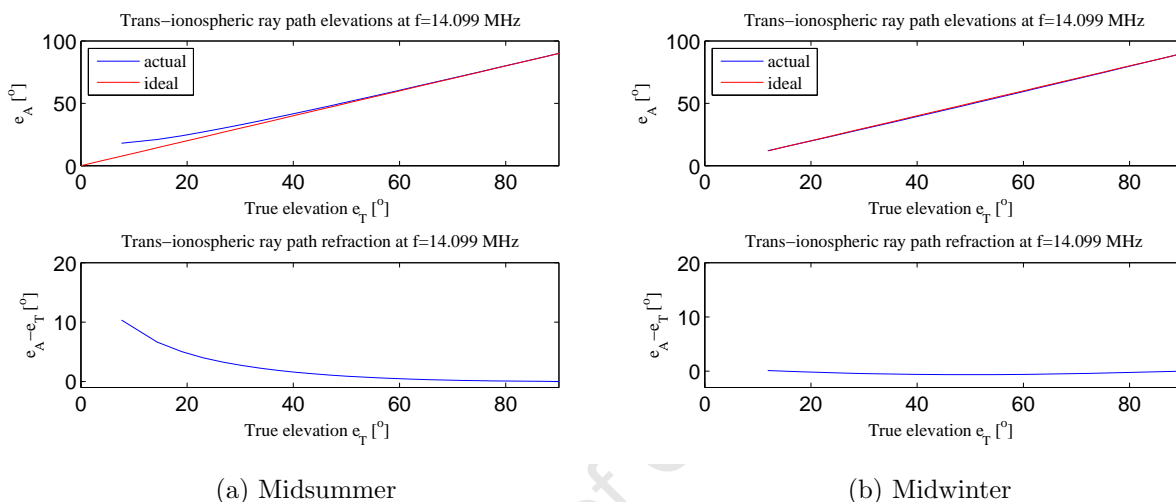

(a) Midsummer   (b) Midwinter

Figure 4.17: Comparison of true and apparent elevation(top panel) and their difference (bottom panel) for the flat Earth multilayer top-to-bottom model at 14.099 MHz for midsummer on 1 January 2011 at 12:00 UT in (a) and midwinter on 1 June 2011 at 23:00 UT in (b)

4.3.2 Model 3b: Spherical Earth top-to-bottom ray tracing

The results of the top-to-bottom ray tracing method for the spherical Earth multilayer model for the worst and best propagation conditions are shown in Figures 4.18 (a) to 4.18 (b). All the ray paths shown reach the ground from the satellite.

(a) Midsummer   (b) Midwinter
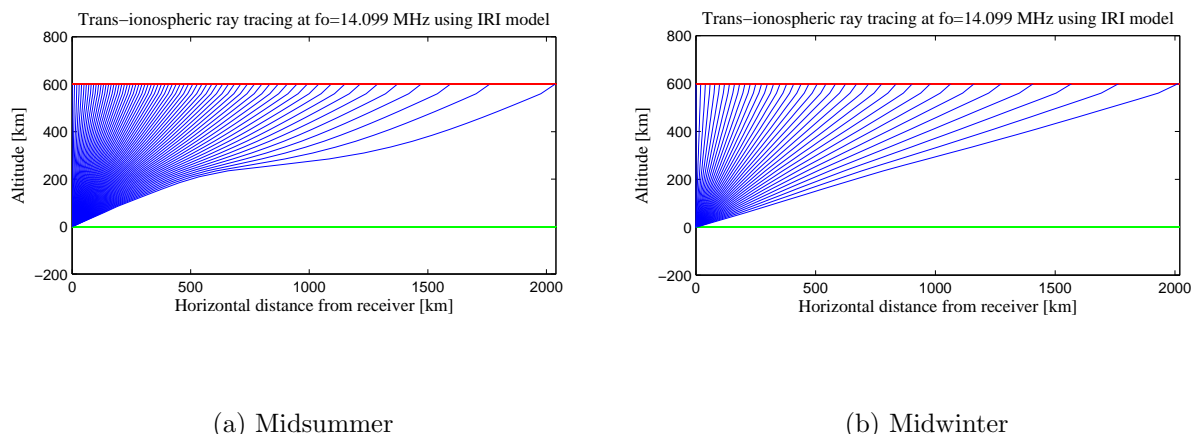
Figure 4.18: Trans-ionospheric ray paths for spherical Earth multilayer top-to-bottom model at 14.099 MHz for midsummer on 1 January 2011 at 12:00 UT in (a) and midwinter on 1 June 2011 at 23:00 UT in (b)

The comparison of the true and apparent elevation angles for "top-to-bottom" ray tracing at a frequency of 14.099 MHz for both midsummer and midwinter dates is shown in Figures 4.19 (a) and 4.19 (b). There is minimal refraction for propagation in winter, as shown in Figure 4.19 (b). In midsummer, there is significant refraction up to a maximum of 12° for elevation angles less that 40° as shown in Figure 4.19 (a).

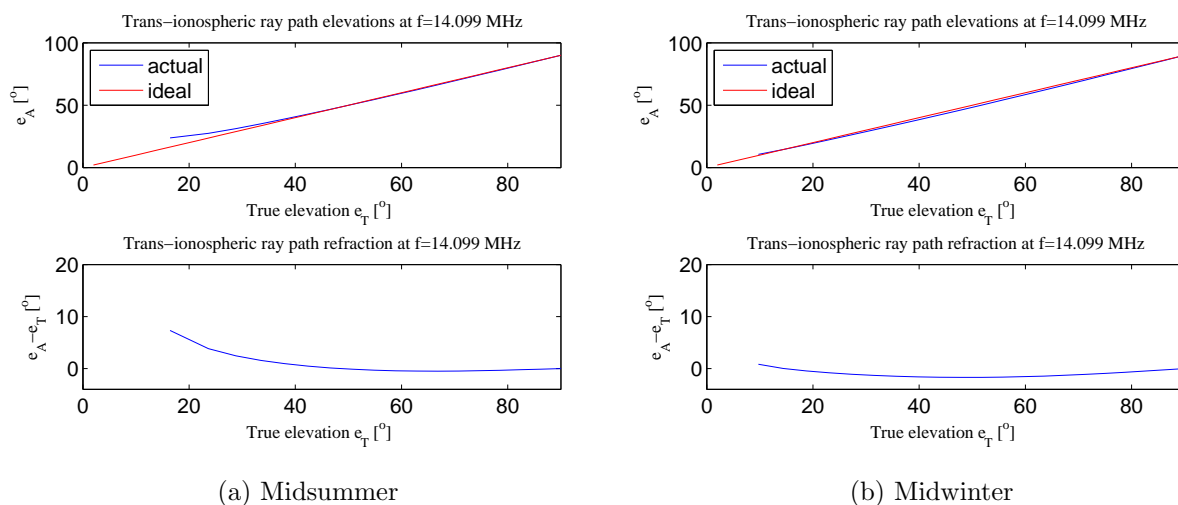(a) Midsummer   (b) Midwinter

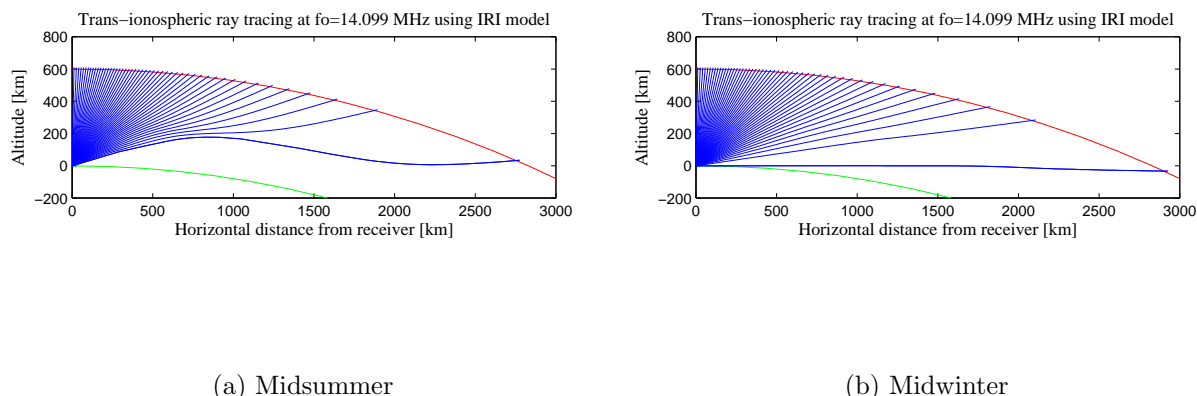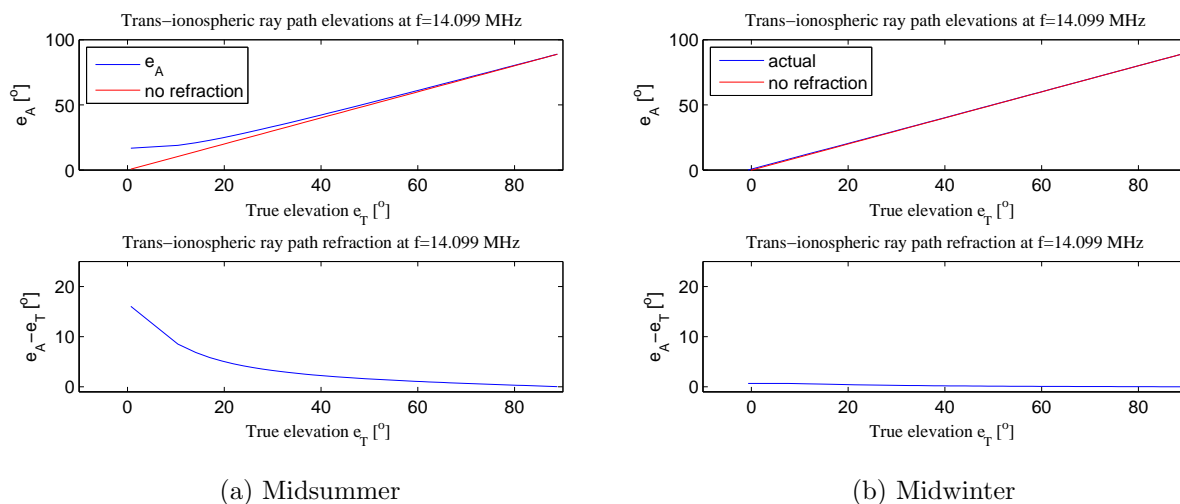Figure 4.19: Comparison of true and apparent elevation (top panel) and their difference (bottom panel) for the spherical Earth multilayer top-to-bottom model at 14.099 MHz for midsummer on 1 January 2011 at 12:00 UT in (a) and midwinter on 1 June 2011 at 22:00 UT in (b)

For each of the ray tracing models, there is a minimum apparent elevation angle, for which

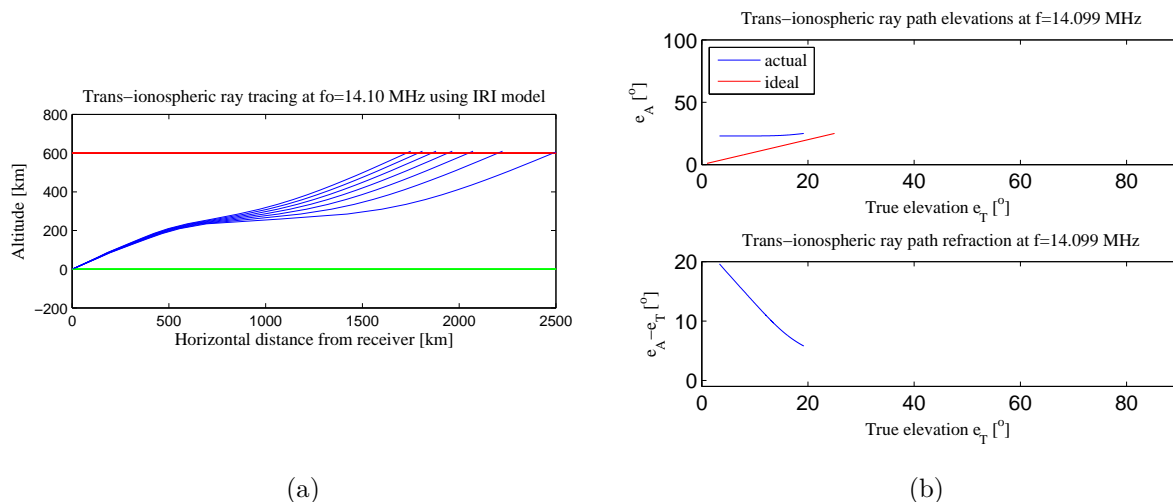(a)   (b)

Figure 4.20: Rays near the minimum apparent elevation angle as obtained with top-down ray tracing using a spherical Earth model at 14.099 MHz for midsummer on 1 January 2011 at 12:00 UT in (a) and midwinter on 1 June 2011 at 23:00 UT in (b)

any ray with an apparent elevation that exceeds it is reflected from the topside of the ionosphere (Table 4.1). For this minimum apparent elevation, there is a range of ray paths with different true elevation values that still traverse the ionosphere and reach the receiver with approximately the same apparent elevation angle. This effect becomes very evident when the step size of the zenith range is made small.

The rays near the minimum apparent elevation angle as obtained with top-down ray tracing using a spherical Earth model at 14.099 MHz were plotted. The apparent and true elevation angles are compared in Figures 4.20 (a) and 4.20 (b). The minimum satellite elevation angle is 6.36°. The apparent elevation angle remains in the range 26.35° to 27.68° while the true elevation ranges from 6.36° to 15.35°.

4.3.3   Comparison of flat Earth and spherical Earth models

In order to assess the error introduced by the assumption of a flat Earth and planar ionosphere, the results of the spherical Earth and flat Earth models were compared for ground to satellite ray tracing during midsummer (1 January 2011 at 12:00 UT) over SANAE IV. Figure 4.21 shows this comparison. Notice that the spherical Earth model predicts a smaller minimum elevation angle than the flat Earth model. This is due to the difference in geometry near the horizon. For the flat Earth model, all rays at zero elevation do not traverse the ionosphere, by definition. However, for the spherical Earth model, even rays from below the horizon can reach the receiver due to refraction.
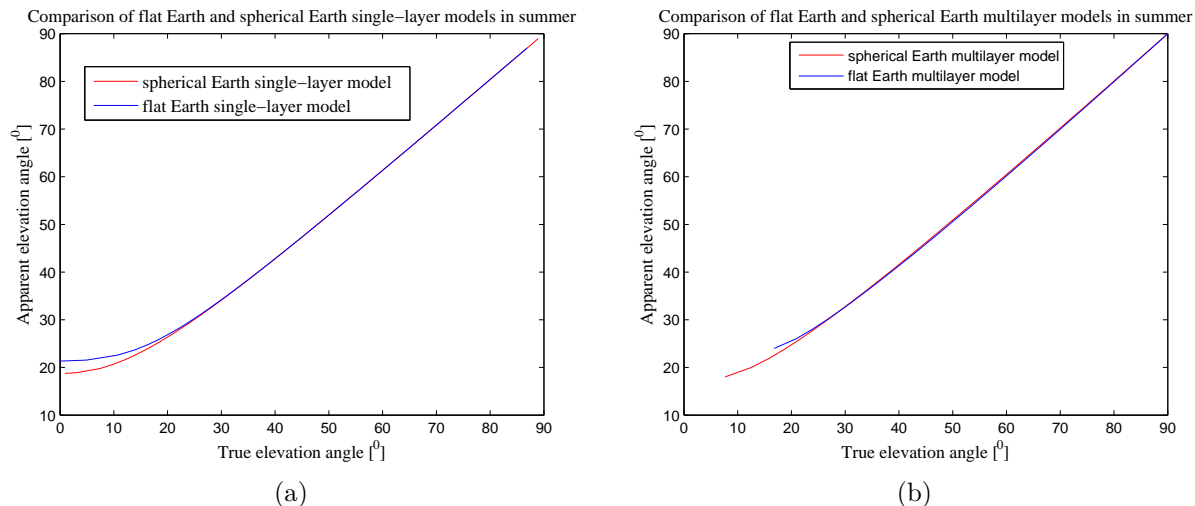
Figure 4.21: Comparison of the results of the flat Earth and spherical Earth models based on from single uniform density ionospheric layer (a) and multilayer (b) models done with bottom-up ray tracing at 14.099 MHz on 1 January 2011 at 12:00 UT over SANAE IV.

4.4   Haselgrove ray tracing

Haselgrove ray tracing is a procedure of tracing the trajectory of an electromagnetic wave in a smoothly varying anisotropic medium, based on a numerical solution of the Haselgrove equations. The Haselgrove equations are ordinary differential equations (ODE's), similar to Euler-Lagrange equations, derived from a mathematical relationship between Fermat's principle and Hamiltonian equations (Coleman, 2008). These Hamiltonian equations consider the ionosphere in the form of a set of tabular height profiles on latitude-longitude points, and are also generalised to include ionospheric absorption. The form of Fermat's principle from which these first order differential equations are derived, is given as:

$$\delta\Phi = \delta \int \mathrm{n}\cos\theta ds \tag{4.36}$$

where Φ is the trajectory, n is the real part of refractive index, θ is the angle between the ray direction and the wave vector, ds is the element of distance along the wave trajectory.

The Haselgrove equations were used to verify of the results of the simpler models 1, 2 and 3, in line with experimental verification. The confidence that the Haselgrove equations enjoy is evidenced by the fact that they are well published (Singh, 1976) and (Mal'Tseva and Chernov, 1989) and ray tracing done with these equations has been verified by ground-to-ground measurements (Lambert, 1978).

In the Haselgrove ray tracing algorithm, the Earth is assumed to be a sphere with a radius of

approximately 6378 km. The spherical ionosphere is converted to a two-dimensional surface which is stretched out and represented by (X,Y) coordinates, where X is the distance along the Earth's surface and Y is the vertical height to the ray path. This mapping introduces some distortion on the ray paths, so that ray paths that are straight on the true spherical model, are represented as curved lines in the X-Y-mapping. The implication of this X-Y-mapping is that at elevation of zero, ray path A looks like ray path A', ray path B looks like ray path B' and ray path C looks like ray path C', as illustrated in Figure 4.22.

The first step towards implementing the Haselgrove ray tracing algorithm was to define a "portion" of the ionosphere for a certain date, time and geographic position, using the Chapman layer ionosphere or any other model of the ionosphere. In this analysis, both the Chapman layer and IRI models were used to define the ionosphere. The next step was to specify the initial elevation, initial bearing of the ray and the frequency of propagation. A number of rays were traced from a specified starting height to the stopping height or to the point where the ray path was reflected from the bottomside ionosphere. For each ray path, the O (red) and X (white) rays were plotted at a bearing of 0° East of North. Details of the implementation of the Haselgrove equations can be found in the paper by Coleman (1993).

In principle the ionosphere is reciprocal, hence ray paths that traverse it from the bottom to the top, would also traverse it from the top to the bottom. Ray paths at elevation angles that are reflected from the bottomside, would also be reflected from the topside. This principle was demonstrated with the spherical Earth multilayer model. Top-to-bottom ray tracing was not implemented for the Haselgrove equations since the software package made available by the authors (Coleman, 1993) had not been set up to perform top-to-bottom ray tracing.

Figure 4.23 shows the extent of the ionosphere that was defined around the receiver at SANAE IV in Antarctica by the Chapman layer ionospheric model for midsummer (Figure 4.23 (a)) and midwinter (Figure 4.23 (b)) and by the IRI model for midsummer (Figure 4.23 (c)) and midwinter (Figure 4.23 (d)). The ray tracing results from the Haselgrove algorithm for both the midsummer and midwinter dates are shown in the Figures 4.24 (a) and 4.24 (b) for the Chapman model and Figures 4.24 (c) and 4.24 (d) for the IRI model respectively. These rays were traced from SANAE IV on the ground to a satellite at a frequency of 14.099 MHz.

The Haselgrove ray tracing results based on both the IRI and Chapman layer model clearly show a number of ray paths for both O and X modes propagating through the ionosphere to the satellite altitude on both the selected dates for midwinter and midsummer. However,
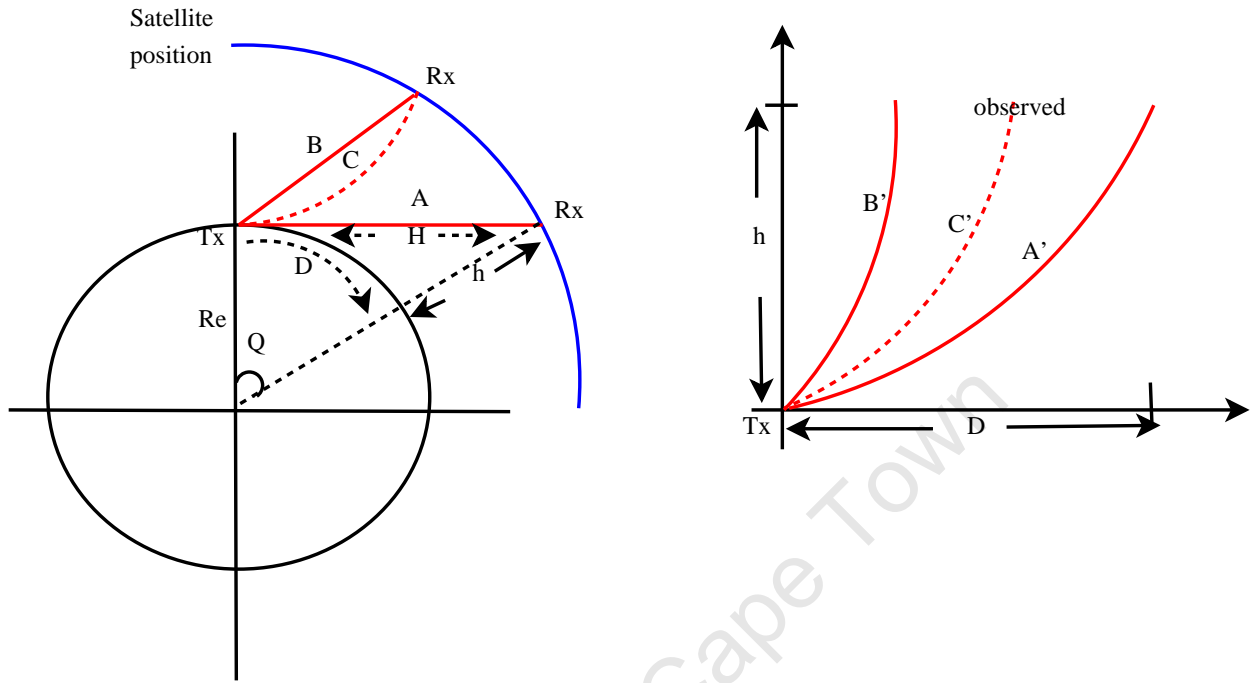
(a)
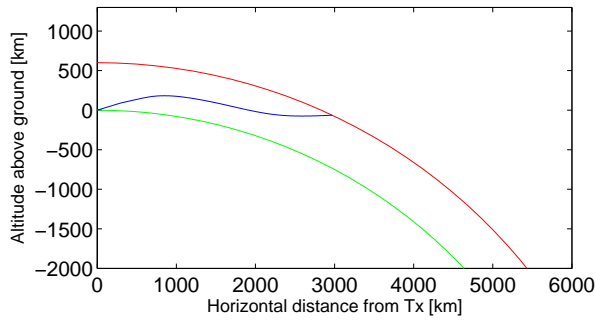
(b)
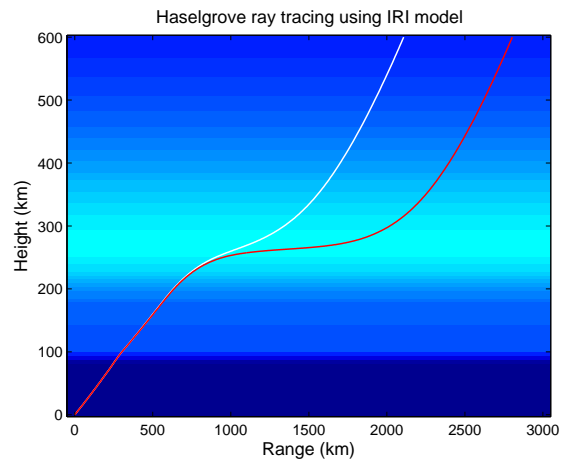
(c)

Figure 4.22: The geometry of the spherical Earth approximation from Haselgrove ray tracing algorithm in (a). The ray paths are in red. A plot of one ray path along the spherical Earth (b), the green boundary is the ground and the red boundary is the satellite altitude. And O (red) and X (white) rays at the apparent elevation angle of $17°$ in (c).

(a) Midsummer

(b) Midwinter

(c) Midsummer

(d) Midwinter
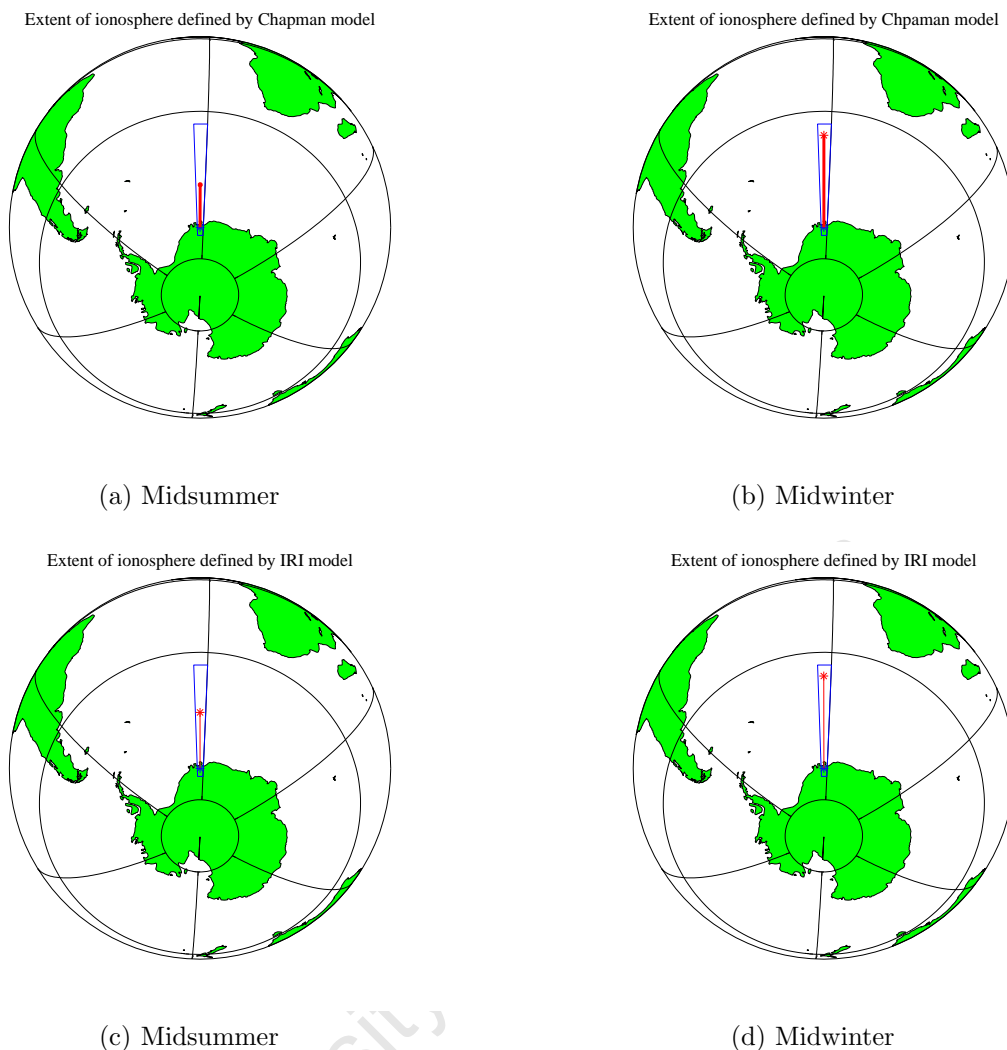
Figure 4.23: The blue boundary shows the extent of ionosphere defined by the Chapman model in (a) and (b) and the IRI model in (c) and (d), respectively around SANAE IV. The red line shows the ray path reaching the satellite altitude at the elevation angle of the first ray to reach the satellite altitude.

in summer some of the rays do not reach the height of 600 km as intended due to reflection and ducting. More rays reach the satellite altitude in winter than in summer as a result of the changes in the refractive index due to a decrease in electron density from summer to winter. The minimum satellite and apparent elevation angles are shown in Table 4.1.

In order to compare the true and apparent elevation angles of the ray paths that reach the altitude of 600 km at SANAE IV, Figure 4.25 was plotted. During summer, the minimum apparent elevation angle was 30° for the ionosphere defined by the Chapman layer and 18° for the ionosphere derived from the IRI model. However, during winter, the minimum apparent elevation angle was 0° for both ionospheric models. This is because in summer the Chapman layer model approximates a higher electron density compared to the IRI model,

(a) Midsummer

(b) Midwinter

(c) Midsummer
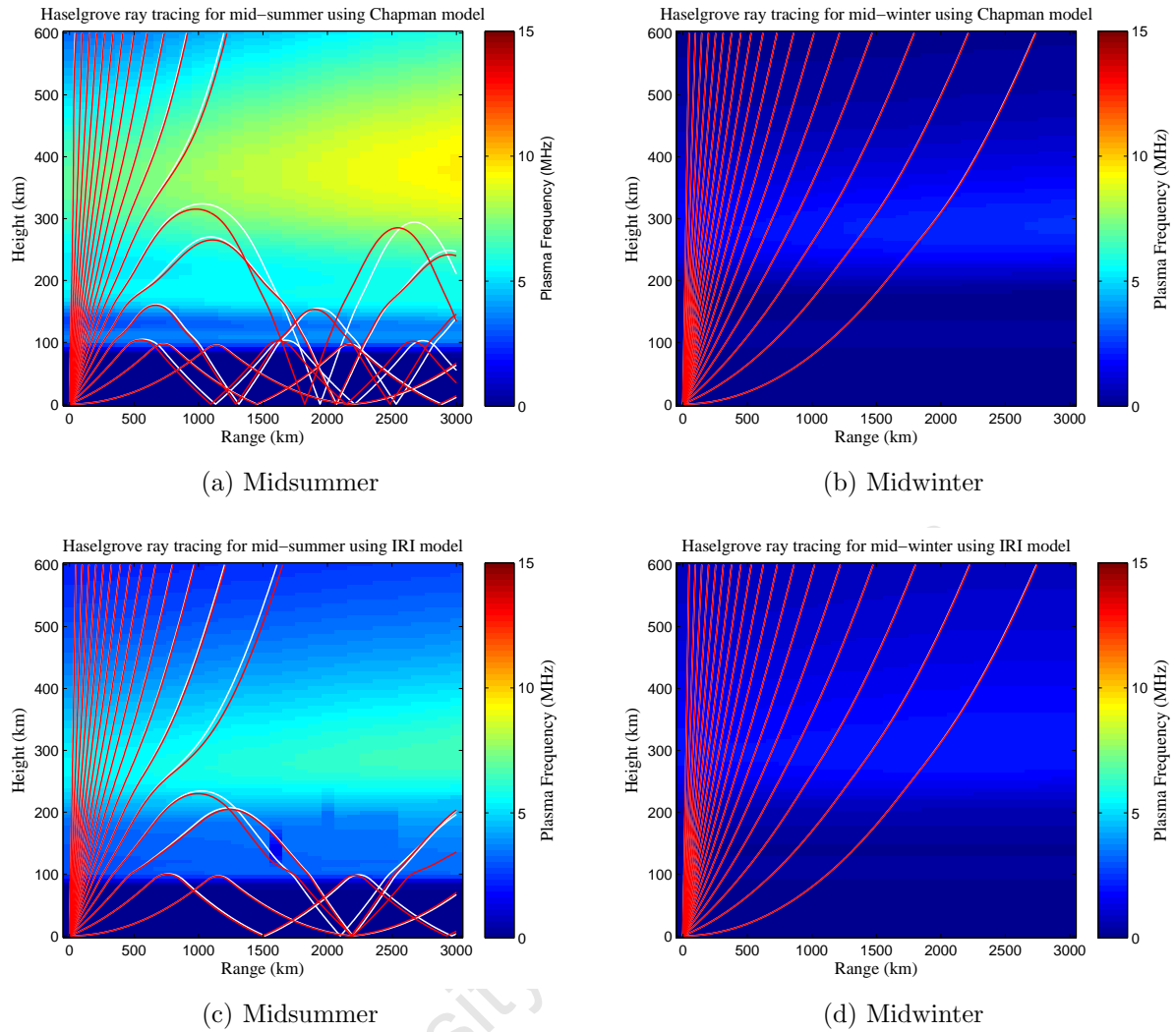
(d) Midwinter

Figure 4.24: Trans-ionospheric ray paths over SANAE IV from Haselgrove ray tracing algorithm at 14.099 MHz using the Chapman and IRI models for midsummer on 1 January 2011 at 12:00 UT in (a) and (c), and midwinter on 1 June 2011 at 23:00 UT in (b) and (d) respectively, at a bearing of 0° East of North.

as shown in Figure 4.26.

Figure 4.25: Comparison of true and apparent elevation angles derived from Haselgrove ray tracing over SANAE IV using the Chapman and IRI models at 14.099 MHz for midsummer on 1 January 2011 at 12:00 UT in (a) and (c), and midwinter on 1 June 2011 at 23:00 UT in (b) and (d) respectively, at a bearing of 0° East of North.
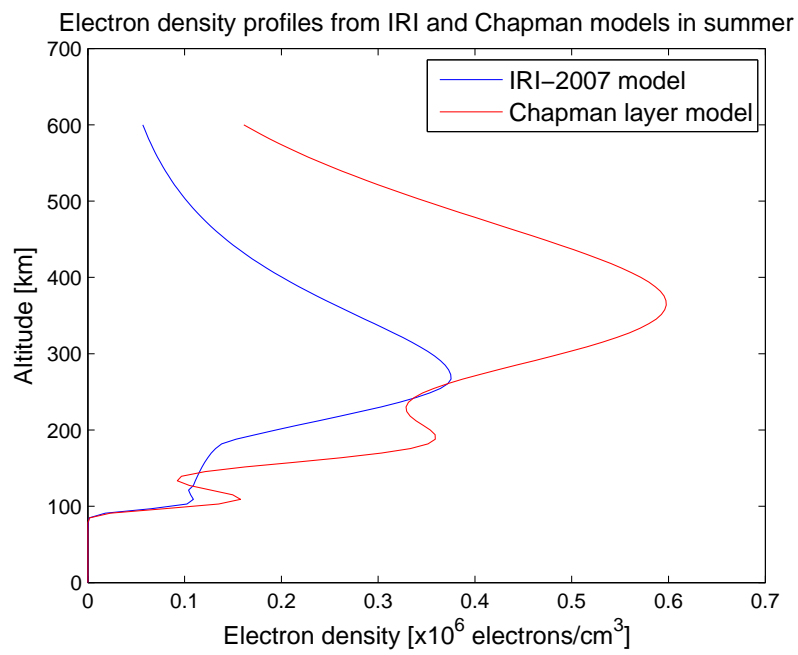
Figure 4.26: Electron density derived from the IRI and Chapman layer models for 1 January 2011 at 12:00 UT.

4.5   Summary of ray tracing results

According to the ray tracing theory, bottom-up and top-to-bottom ray tracing have the same equations that describe the ray path going in different directions. To check whether the results of the bottom-up and top-to-bottom ray tracing match the theory, Figure 4.27 was plotted. This comparison was done for midday in summer when the maximum refraction is expected. It is clear from this figure that the results are very similar. Therefore, it is safe to say that the results match the theory.
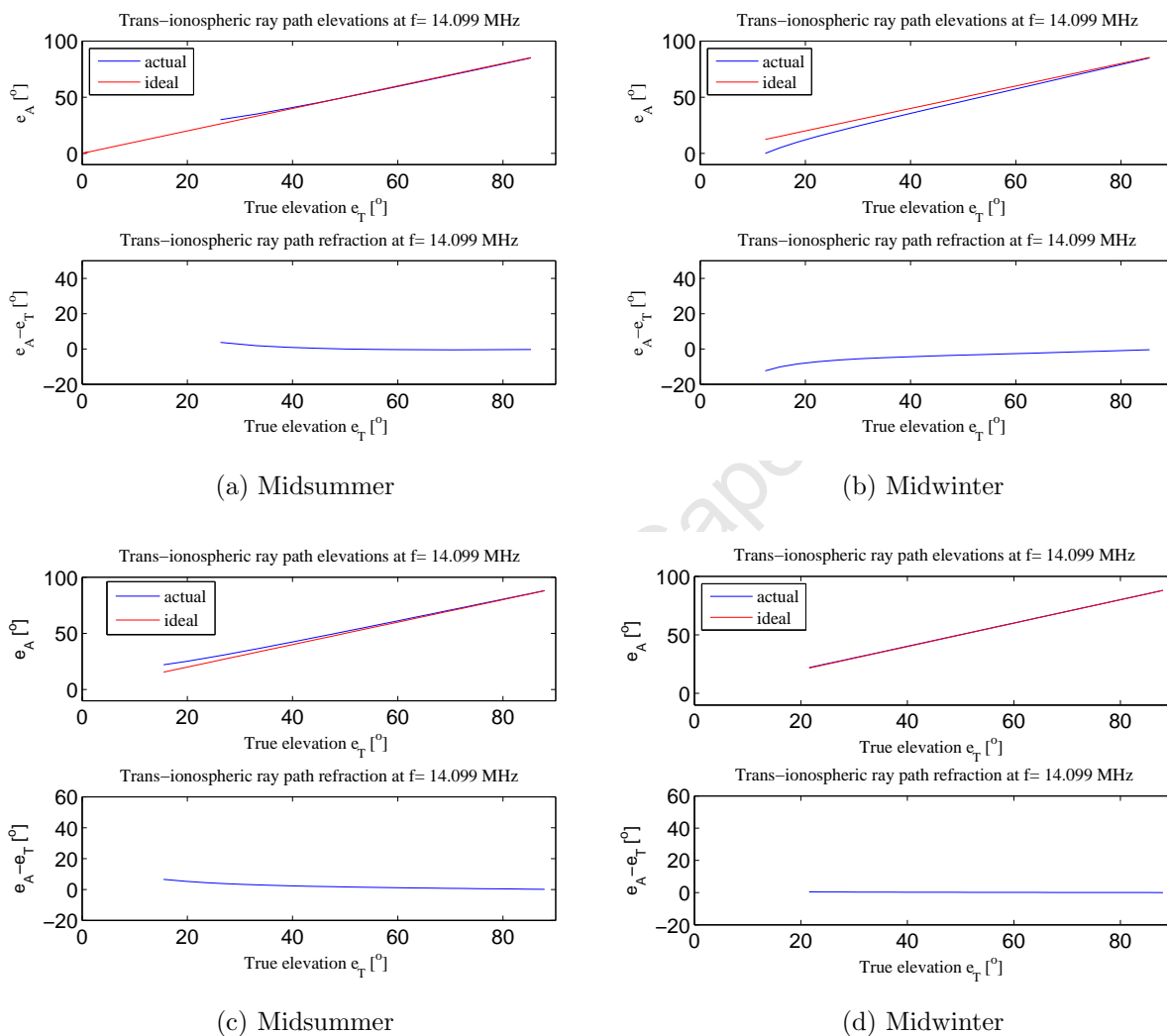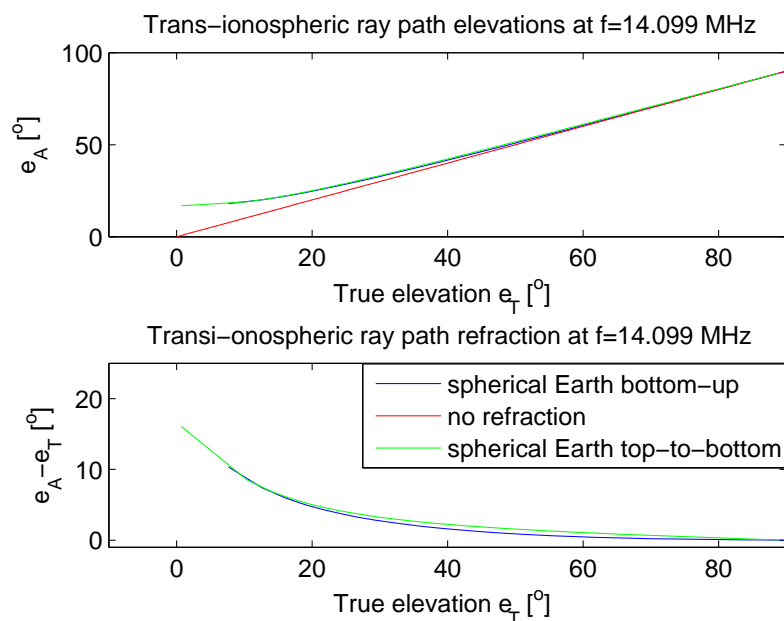

(a)

Figure 4.27: Comparison of true and apparent elevation angles from the bottom-up and top-to-bottom spherical Earth multilayer models for midsummer on 1 January 2011 at 12:00 UT using electron density derived from the IRI model.

Figures 4.28 (a) and (b) show the comparison of true and apparent elevation angles obtained by means of the spherical Earth multilayer model (bottom-up) and the ordinary ray paths from the Haselgrove ray tracing using the IRI model for midsummer on 1 January 2011 at 12:00 UT. This result shows a very close correlation between Model 2b and the Haselgrove equations. In both cases the electron density was derived from the IRI-2007 model.

Table 4.1 summarises the minimum true (E_T) and apparent (E_A) elevation angles of the single-layer, uniform electron density model (Model 1), multilayer model (Model 2) and the Haselgrove ray tracing model. The zero minimum value obtained in both summer and winter for the flat Earth single-layer model (Model 1a) is unrealistic, because it would mean that either the satellite is on the ground or it is infinitely far away, both of which are not the case

Haselgrove and spherical Earth multilayer model in summer

(a)
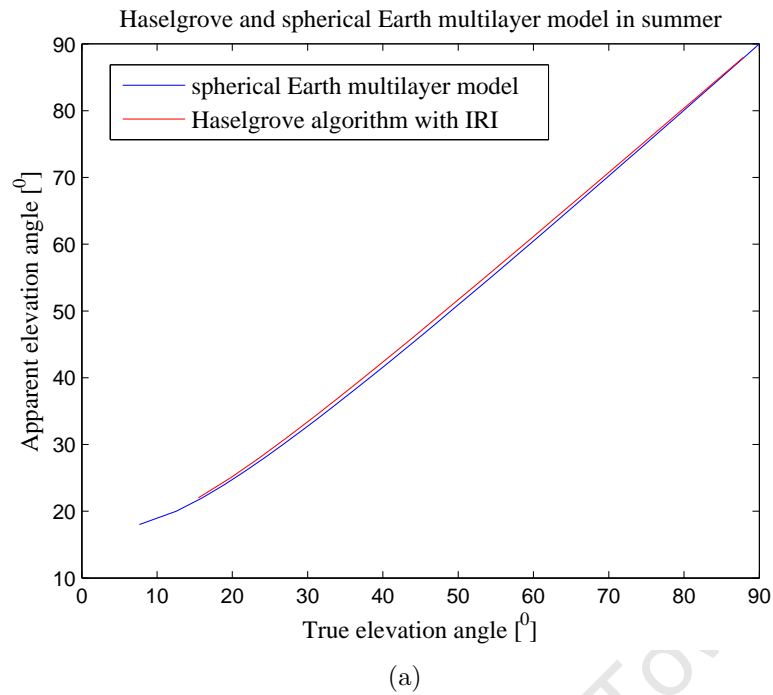
Figure 4.28: Comparison of true and apparent elevation angles from Model 2(b) and the Haselgrove ray tracing algorithm for midsummer on 1 January 2011 at 12:00 UT using electron density derived from the IRI model.

here. During winter, the spherical Earth single-layer and multilayer models give values of the true elevation angle that are higher than the apparent elevation angle. This is possible when the ray paths go beyond the horizon.

Table 4.1: Summary of the uniform electron density model with rays propagating from ground to satellite. Electron density is in electrons/cm^3, min E$_T$ and min E$_A$ are minimum satellite and apparent elevation angles in degrees

Model and Time	min E$_T$	min E$_A$
Model 1a (summer)	0.00	21.33
Model 1b (summer)	0.89	18.77
Model 2a (summer)	16.82	22.00
Model 2b (summer)	7.66	16.00
Haselgrove-IRI (summer)	7.38	18.00
Haselgrove-Chapman (summer)	26.29	30.00
Model 1a (winter)	0.00	10.19
Model 1b (winter)	1.10	0.00
Model 2a (winter)	8.76	8.00
Model 2b (winter)	0.36	0.00
Haselgrove-IRI (winter)	0.68	0.00
Haselgrove-Chapman (winter)	12.38	0.00

Chapter 5

Conclusion and future work

5.1 Discussion of results and conclusions

According to the link budget, for the signal to be detectable by the receiver, it should have sufficient power. Typically for HF transmission, the signal is detectable if the signal strength at the receiver is -120 dBm for 12 dB signal in noise at distortion (SINAD). The maximum Doppler shift at 14.099 MHz is ± 300 Hz and this is within the bandwidth of the receiver. The link margin is the difference between the above required received signal power and actual received signal power calculated at a specific elevation angle. It must be greater than 3 dB.

The orbit analysis showed that the satellite will be visible from SANAE IV for the inclination of 97.8° and SANSA and Grintek for the two inclination angles. During a 24 hour period, it was determined that for the 14 orbits, 7 to 12 satellite passes would be visible from SANAE IV and 4 to 5 passes would be visible from both SANSA and Grintek at inclination angles of 97.8° and 65°. The results for the stations at SANSA and Grintek are comparable because of their geographical proximity.

For SANAE IV, the significant satellite passes were the ones that are in the elevation and azimuth range of the radar's beam, that is 0°-30° and 156°-210° respectively. Ray tracing was done using the spherical Earth multilayer model for satellite passes at true elevation angles for each of the receiver locations to calculate the expected refraction. The refraction, which is the difference between apparent and true elevation angles, ranged from 16.4° to 20.0° during summer and from 0.6° to 1.8° during winter, as shown in Table 3.1. Generally lower true elevation angles were subject to more refraction than higher true elevation angles.

The visibility of ZACUBE 1, at an inclination angle of 97.8° and altitude of 600 km from SANAE IV under favorable conditions, was between 6 and 13 minutes per pass, for most

of the 13 and 7 anticipated passes per day over SANAE IV in Antarctica at the inclination angle of 97.8° and 65° respectively. The satellite was also visible from SANSA,Hermanus and Grintek,Pretoria at elevations below 30° (which is of primary interest for the calibration of the SuperDARN radar) for 10 to 13 minutes per pass, for the 4 to 6 passes per day at both inclination angles (97.8°, 65°).

The results of the ray tracing using the flat Earth and spherical Earth models are comparable, with the spherical Earth model predicting smaller minimum elevation angles than the flat Earth model, as shown in Figure 4.21. The apparent and true elevation angles for Models 1 and 2 were very similar, an indication that both single uniform density layer and multilayer approximations are viable. The difference between bottom-up and top-to-bottom ray tracing results was minimal (Figure 4.27).

There was a very good correlation between the spherical Earth multilayer model and the Haselgrove ray tracing algorithm with electron density derived from the IRI model during summer (Figure 4.28). The Haselgrove equations were used to evaluate the simplified ray tracing equations used in models 1, 2 and 3. The fact that the spherical Earth multilayer model gives a result close to the Haselgrove algorithm during the worst propagation time, shows that it is the best ray tracing model of the 3 models discussed. In addition, the spherical Earth multilayer model showed the least refraction in summer compared to the single layer model and minimal refraction in winter for true elevation angles of all the satellite passes over SANAE IV. A significant number of rays obtained by means of the spherical Earth multilayer model reached the satellite altitude over a large horizontal range.

In conclusion, these results show that the orbit analysis software is able to predict the position of the satellite and that the ray tracing models are able to calculate the amount of refraction the signal is expected to experience. This implies that the signal will be observed at SANAE IV in Antarctica, SANSA in Hermanus and Grintek in Pretoria for an inclination greater than 70°. The period of visibility per day was longer as SANAE IV at the inclination of 97.8° than at the other receiver locations considered. The best propagation time to characterise the radar is midnight in winter because there is minimal or no refraction of the signal, and the best propagation time to perform ionospheric physics is midday in summer since there is significant refraction for measuring TEC using either phase delay or Faraday rotation. Therefore, the sampling rate of 2 minutes of the SuperDARN radars allows the signal to be recorded and stored for a sufficient length of time.

5.2 Proposed future work

The orbit analysis can take into account the effects of the Earth's nutation and precession caused by the Earth's oblateness. In the ray tracing models only the vertical gradients in electron density were considered. Thus the ray tracing models can be modified to include horizontal and azimuthal gradients. In the ray tracing algorithm, absorption can also be taken into account so as to find out how much of the signal is absorbed by the ionosphere. Furthermore, the error in the received satellite signal due to multipath and reflection should be investigated.

Once the satellite has been launched, actual data from the satellite's two line elements can be used for tracing in real time. The results can then be used to calibrate the radar at SANAE IV. This data can be compared to data from future satellite missions with an HF beacon transmitter or receiver. When an appropriate receiver is available to resolve the wave polarisation, the real data from the CubeSat can be used to calculate TEC using phase shift and Faraday rotation. This will aid characterisation of the ionosphere over the Earth's polar regions.

Chapter 6

Appendix

All the software used for this work are available on a disc, submitted along with the written content. Each of the programmes are labeled as shown below.

The satellite orbit analysis programme:

Satellite_orbit_propagator.html

The ray tracing programme for the single-layer ionospheric model:

Ray_tracing_single_layer_model.html

The ray tracing programme for the multilayer model:

Ray_tracing_multilayer_model.html

The Haselgrove ray tracing algorithm:

Haselgrove_ray_tracing.html

Bibliography

Anderson D.N., Forbes J.M. and Codrescu M., "A fully Analytic, Low-and Middle-Latitude Ionospheric Model", *Geophysics Research*, **94**, pp. 1520–1524, 1989.

Appleyard S.F., Linford R.S. and Yarwood P.J., *Marine Electronic Navigation (2nd ed.)*, London: Routledge and Kegan Paul, 1988.

Bennett J.A., Dyson P.L. and Norman R.J., "Progress in Radio Ray Tracing in the Ionosphere", *Radio Science*, **104**, pp. 81–91, 2004.

Bilitza D., "The E and D region in IRI", *Advances in Space Research*, **21**, pp. 871–874, 1998.

Bilitza D., "International Reference Ionosphere 2000", *Radio Science*, **vol.36**(2), pp. 261–275, 2001.

Budden K.G., *The Propagation of Radio Waves: The Theory of Radio Waves of Low Power in the Ionosphere and Magnetosphere*, New York: Cambridge University Press, 1985.

Chisham G., Lester M., Milan S.E. and et al, "A decade of the Super Dual Auroral Radar Network (SuperDARN): Scientific Achievements, New Techniques and Future Directions", *Surveys in Geophysics*, **28**(1), pp. 33–109, 2007.

Chiu Y.T., "An Improved Phenomenological Model of Ionospheric Density", *Journal of Atmospheric and Terrestrial Physics*, **37**, pp. 1563–1570, 1975.

Cilliers P., *SANAE HF Radar Calibration*, Technical report, Hermanus Magnetic Observatory, Hermanus, South Africa, 2007.

Coleman C.J., *A General Purpose Ionospheric Ray Tracing Procedure*, Technical report, Defence Science and Technology Organisation, Australia, Salisbury, 1993.

Coleman C.J., "Ionospheric Ray Tracing Equations and their Solution", *Radio Science Bulletin*, **325**, p. 1723, 2008.

Das S.K., *Mobile Handset Design*, Singapore: John Wiley and Sons, 2010.

Davies K., *Ionospheric Radio,IEE Electromagnetic waves series 31*, London: Peter Peregrinus, 1990.

Downey A.B., *Physical Modeling in MATLAB Version 1.1.6*, Washburn: Green Tea Press, 2011.

Evans B.G., *Satellite Communication Systems (3rd ed.)*, London: The Institution of Electrical Engineers, 2008.

Exelis Visual Information Solutions, "Environment for Visualising Images (ENVI)", Intrnet:http://www.ittvis.com/ProductServices/ENVI.aspx., Accessed in May 2012.

Giraud A. and Petit M., *Ionospheric Techniques and Phenomena*, Dordrecht: Reidel Publishing Company, 1978.

Hardy D., Gussenhoven M.S., Raistrick R. and McNeil W.J., "Statistical and Functional Representations of the Pattern of Auroral Energy Flux and Conductivity", *Geophys Research*, **92**, pp. 812275–12294, 1987.

Haslett C., *Essentials of Radio Wave Propagation*, New York: Cambridge University Press, 2008.

Howard C.D., *Orbital Mechanics for Engineering Students (2nd ed.)*, Burlington: Elsevier, 2010.

Kimura I., "Effects of Ions on Whistler-Mode Ray Tracing", *Radio Science*, **1**, pp. 269–283, 1966.

Kohl H., Ruster R. and Schlegel K., *Modern Ionospheric Science*, Kattenburg-Linda: European Geophysical Society, 1996.

Lambert S., "Studies in Ionospheric Ray Tracing", *M.A. Thesis - Rhodes University Magnetic Observatory, Grahamstown, South Africa*, 1978.

Mal'Tseva O. and Chernov G., "Whistler Ray Tracing Calculations in the Solar Corona", *Kinematika i Fizika Nebesnykh Tel*, **5**, pp. 32–43, 1989.

McNamara L.F., *The Ionosphere: Communications, Surveillance, and Direction Finding*, Malabar, FL: Krieger, 1991.

McNamara L.F., *Radio Amateurs Guide to the Ionosphere*, Malabar, FL: Krieger, 1994.

Michael O.K., *Satellite Communication Engineering*, New York: Marcel Dekker, 2002.

Ratcliffe J.A., *An Introduction to the Ionosphere and Magnetosphere*, New York: University of Cambridge Press, 1997.

Rawer R. and Bilitza D., "Electron Density Profile Description in the International Reference Ionosphere", *Journal of Atmospheric and Terrestrial Physics*, **51**, pp. 781–790, 1989.

SANAP and SANAE, "South African National Antarctic Expedition (SANAE)", Internet:http://www.sanap.org.za/sanap_sanae/sanap_sanae.html., Accessed in March 2012.

Serway R.A. and Jewett J.W., *Physics for Scientists and Engineers (8th ed.)*, Belmont: Brooks Cole, 2010.

Singh B., "On the Ground Observation of Whistlers at Low Latitudes", *Geophysical Research*, **81**, pp. 2429–2432, 1976.

St-Pierre J., Melanson P., Brunet C. and Crabtree D., "Validation of Mission Plans Through Simulation", *In the 34th COSPAR Sceintific Assembly, The Second World Space Congress, held 10-19 October in Houston, TX.*, pp. U–5–05IAF abstracts, 2002.

Sterne K.T., "Testing the Re-designed SuperDARN HF Radar and Modeling of a Twin Terminated Folded Dipole Array", *M.A thesis, Virginia Polytechnic Institute and State University, Blacksburg, VA*, pp. 97–101, 2010.

Stodden D.Y., "Space System Visualization and Analysis using the Satellite Orbit Analysis Program (SOAP)", *Aerospace Applications Conference held on 4-11 February in Los Angeles, CA , Proceedings, IEEE.*, **1**, pp. 369 – 387, 1995.

Stroyan K.D., *Projects for Calculus: The Language of Change (2nd ed.)*, San Diego: Academic Press, 1999.

Tomas N., "Ray Tracing Algorithm for Interactive Applications", *M.A thesis, Czech Technical University, Prague, Czech Republic*, 2010.

Visser D., *ZACUBE 1, 1U CubeSat: Mission Requirements and Technical Specifications*, Technical report, Satellite Engineering Programme, French South African Institute of Technology, South Africa, 2009.